ORGANIC SEMICONDUCTOR LASERS: COMPACT HYBRID LIGHT SOURCES AND DEVELOPMENT OF APPLICATIONS

Ying Yang

A Thesis Submitted for the Degree of PhD
at the
University of St Andrews

2010

Full metadata for this item is available in
Research@StAndrews:FullText
at:
http://research-repository.st-andrews.ac.uk/

Please use this identifier to cite or link to this item:
http://hdl.handle.net/10023/2569

This item is protected by original copyright

Organic Semiconductor Lasers: Compact Hybrid Light Sources and Development of Applications

Ying Yang

April 2010

A thesis submitted to the School of Physics and Astronomy, at the University of St Andrews, for the degree of Doctor of Philosophy

Declaration

I, Ying Yang, hereby certify that this thesis, which is approximately 41000 words in length, has been written by me, that it is the record of work carried out by me and that it has not been submitted in any previous application for a higher degree.

I was admitted as a research student in September 2006 and as a candidate for the degree of Doctor of Philosophy in September 2006; the higher study for which this is a record was carried out in the University of St Andrews between 2006 and 2010.

April 2010 Ying Yang

I hereby certify that the candidate has fulfilled the conditions of the Resolution and Regulations appropriate for the degree of Doctor of Philosophy in the University of St Andrews and that the candidate is qualified to submit this thesis in application for that degree.

April 2010 Ifor D. W. Samuel

April 2010 Graham A. Turnbull

Copyright Declaration

In submitting this thesis to the University of St Andrews we understand that we are giving permission for it to be made available for use in accordance with the regulations of the University Library for the time being in force, subject to any copyright vested in the work not being affected thereby. We also understand that the title and the abstract will be published, and that a copy of the work may be made and supplied to any bona fide library or research worker, that my thesis will be electronically accessible for personal or research use unless exempt by award of an embargo as requested below, and that the library has the right to migrate my thesis into new electronic forms as required to ensure continued access to the thesis. We have obtained any third-party copyright permissions that may be required in order to allow such access and migration, or have requested the appropriate embargo below.

April 2010 Ying Yang

April 2010 Ifor D. W. Samuel

April 2010 Graham A. Turnbull

The following is an agreed request by candidate and supervisor regarding the electronic publication of this thesis:

Access to all of printed copy but embargo of all of electronic publication of thesis for a period of 2 years on the following ground: publication would preclude future publication.

April 2010 Ying Yang

April 2010 Ifor D. W. Samuel

April 2010 Graham A. Turnbull

Acknowledgement

I would like to thank my supervisors, Prof. Ifor Samuel and Dr. Graham Turnbull who gave me this opportunity to study a PhD. In the past three and a half years, they kept giving me useful suggestions, interesting motivations and persistent encouragements. They are definitely the best supervisors I can imagine.

Also, thanks to all the people in the organic semiconductor centre. It is my great pleasure to work with them. Particularly, thanks to Dr. Georgios Tsiminis for guiding me patiently step by step into the research field and the continuing supports with intriguing ideas; Dr. Andreas Vasdekis for showing me the high standard of a good PhD with all the valuable publications that help me a lot in the past three years; Dr. Paul Shaw for his help in both scientific work in ellipsometry and the difficult and funny trip to Brazil; Dr. Dimali Amarasinghe for her lovely encouraging smiles; Dr. Arvydas Ruseckas for his useful discussions and the effort of taking the most dangerous laser beam out for me; Gorden Hedley for his precious suggestions and the informal competition in thesis writing; Yue Wang for being a good friend and carrying on some of my projects; Shu Chen for his continuing faith in me and the delicious food. Additionally, thanks will go to everyone in the physics department, especially the secretaries and technician staffs Mr. G. Robb and Mr. S. Balfour. Lastly, I'd like to thank my parents for their loves and supports which helped me through the tough moments in the past years.

Abstract

This thesis describes a number of studies on organic semiconductors as laser gain media with the aim of simplifying the excitation scheme and exploring potential applications.

A hybrid device taking the advantage of high power inorganic light emitting diodes (LEDs) and low threshold organic distributed feedback lasers is demonstrated to realize an LED pumped organic laser. When the drive current is higher than 152 A, a sharp peak is clearly observed in the laser output spectrum, implying the LED successfully pumps the polymer laser above threshold. This is the first time an incoherent LED has been used as the excitation source for an organic semiconductor laser. A strategy for further improving the performance of the hybrid device is explored with the use of a luminescent concentrator made of a dye doped SU8 film, to intensify the power density from the inorganic LED. The luminescent concentrator is capable of increasing the incident power density by a factor of 9 and reducing the lasing threshold density by 4.5 times.

As a preliminary investigation towards mode-locked polymer lasers, the impact of a solid state saturable absorber on a solution based organic semiconductor laser is explored. The dye doped polystyrene thin film saturable absorber exhibits a saturation intensity of a few MW/cm^2. When it is placed into the laser cavity, a train of short pulses is generated and the underlying mechanism is discussed.

Finally, the potential of using organic semiconductor lasers in the detection of nitro-aromatic explosive vapours is studied in distributed feedback polyfluorene lasers. A high sensing efficiency and fast response from the laser prove polyfluorene lasers can be used as disposable and low cost devices in explosive chemosensing.

Table of Contents

Chapter 1: Introduction **1**

Chapter 2: Theory of Organic Semiconductor Lasers **11**

2.1. Introduction 11

2.2. Organic semiconductor 12

2.2.1. Molecular structure 12

2.2.2. Optical properties 15

2.2.3. Types of organic semiconductors 19

2.2.4. Stimulated emission 21

2.3. Organic semiconductor lasers 25

2.3.1. Introduction 25

2.3.2. Organic semiconductor laser resonators 26

2.3.3. Pumping sources for organic semiconductor lasers 33

2.4. Reference 36

Chapter 3: Experimental Methods **43**

3.1. Introduction 43

3.2. Fabrication and characterization of organic thin films 44

3.2.1. Sample preparation 44

3.2.2. Photophysical characterization 45

3.2.3. Gain and loss measurement 48

3.2.3.1. Excitation source:
Optical Parametric Oscillator 48
3.2.3.2. ASE measurement 51
3.3. Laser cavity fabrication 52
3.4. Organic semiconductor laser characterization 57
3.5. Angle resolved photoluminescence 59
3.6. Reference 61

Chapter 4: Hybrid Optoelectronics: A Polymer Laser Pumped by an InGaN LED 63
4.1. Introduction 63
4.2. Characterization of GaN LEDs 64
4.2.1. Focusing ability 65
4.2.2. LEDs under pulsed operation 67
4.3. Pumping geometries 76
4.4. Laser gain medium and resonator 80
4.4.1. MEH-PPV and its blends 81
4.4.2. Fluorene- based Copolymer 87
4.4.3. LED pumped polymer laser 94
4.5. Conclusion 99
4.6. Reference 101

Chapter 5: The Development of Luminescent Concentrator for Pumping Organic Lasers 105
5.1. Introduction 105
5.2. Principles of Luminescent concentrator (LC) 107
5.3. Experimental 109
5.4. Selection of materials 110

5.4.1. Active organic dye 110
5.4.2. Passive matrix material 111
5.4.3. Optimization of the LC 116
5.5. Theoretical simulation 122
5.6. Further improvement of LCR 129
5.7. Organic laser gain medium 132
5.8. Impact of pump geometries on lasing threshold 134
5.9. Effective Light Concentration Ratio (ELCR) 138
5.10. Concentrator pumped polymer laser 139
5.11. Conclusion 141
5.12. Reference 142

Chapter 6: Towards Mode-Locked Organic Lasers 145
6.1. Introduction 145
6.2. Principles of saturable absorbers & passive mode locking 147
6.3. Saturable absorber characterization 152
6.3.1. Material for saturable absorber 152
6.3.2. Experimental 153
6.3.3. HIDCI saturable absorption 155
6.3.4.1. Experimental results 155
6.3.4.2. Numerical simulation of saturation intensity 160
6.3.4. HIDCI SESAM 163
6.4. Organic semiconductor laser cavity 166
6.5. Laser characterization 170
6.5.1. Cavity without saturable absorber 170
6.5.2. Cavity with saturable absorber 172
6.6. Simulation of output pulse with saturable absorber 177
6.7. Conclusion 180

6.8. Reference 182

Chapter 7: Explosive Vapour Sensing with Organic Lasers 185

7.1. Introduction 185

7.2. Background theory 187

7.3. Experimental setup 188

7.4. Lasing threshold and slope efficiency change 191

7.5. Exposure Dynamics 197

7.6. The diffusion of DNB molecules in the PFO layer 203

7.7. Confinement factor 206

7.8. Conclusion 209

7.9. References 210

Chapter8: Conclusion 215

Chapter 1

Introduction

The discovery of electrical conductivity in polymer polypyrrole in 1963 [1] and the later well known report of polyacetylene in 1977 [2] announced a new category of material. These are similar to normal plastic, but distinguish themselves as conductors rather than insulators. In 2000, the Nobel Prize in Chemistry was awarded to Heeger, McDimarmid and Shirakawa for their achievements in conducting polymers to acknowledge the importance of this new kind of material. Since then, organic semiconductors have been the object of study across various research fields including chemistry, physics and biology [3-5]. In 1987, electroluminescence was observed experimentally in small molecule organic materials and later, in 1990, in conjugated polymers [6-7], leading to the development of highly efficient organic light emitting diodes (OLEDs). OLEDs are competitive alternatives to the current widely-used liquid crystal in display industry due to their simple fabrication, low cost and scope of wavelength tuning from different molecular designs. The rapid developments in OLEDs have driven the research on material synthesis towards organic semiconductors with high light emitting efficiency and carrier mobilities. Apart from the display industry, organic semiconductors find their importance in other research fields, such as transistors [8] and solar cells [9].

With strong absorption, broad emission spectra and high light emission efficiencies, organic semiconductors are attractive gain media for compact and low cost visible lasers. The first organic semiconductor laser was demonstrated in 1992 in the solution state [10], similar to organic dye lasers. The first solid state organic semiconductor laser based on a microcavity resonator was reported in 1996, proving them much more attractive than solution dye lasers. In the microcavity, along the feedback direction, a very thin organic layer of 100 nm was used for light amplification [11]. These early demonstrations of solid state organic semiconductor lasers triggered a large and growing research effort to optimize the laser performance. New organic semiconductor materials have been developed to enhance the gain and wavelength tunability [12-13]. Besides, improvements have been carried out on resonator designs. Apart from the initial relatively expensive microcavities, waveguide Fabry-Perot cavities [14], microlasers[15-17], and diffractive cavities [18-20] have been used over the past twenty years towards constructing a compact and low-cost laser system. Organic semiconductor lasers have exhibited wide tunability across the visible spectral range [12], modest output energy [14, 21] and short pulse width [22-23], and have already shown huge potential for applications, such as biomarker [24], data communication [25] and chemosensing [26].

While significant progress has been made in developing broadly tunable visible lasers in these materials, there is still much work to do to drive the technology towards practical applications. Firstly, to take organic semiconductor lasers out of the laboratory, there is a need to simplify the pumping system. Secondly, for applications such as spectroscopy, it would be desirable to have better control of lasing properties including the pulse duration. The work in this thesis aims to address these important areas, and to develop one application of these devices for chemical sensing.

At present, organic semiconductors are all optically pumped. They require other lasers as pump sources, which increases the cost and complexity of organic semiconductor laser systems. Electrically excited organic laser diodes would transform the situation, but to date this has remained impossible due to low carrier mobilities and significant additional losses from injected carriers [27]. To achieve this ultimate goal of organic semiconductor lasers, continuous effort has been made to address the challenges [28-31]. In the past twenty years, the threshold of organic semiconductor lasers has gradually reduced with new material development and resonator optimization. Less and less power/energy is required from the excitation source. Hence, lasers with smaller and smaller size (reducing from a regenerative amplifier [11] to InGaN laser diode [32]) can now be used as excitation sources for organic semiconductor lasers. Further simplification of the excitation source would be very attractive for practical lasers.

The major part of the thesis is to explore the feasibility of using an inorganic LED as the pump source for organic semiconductor lasers. LED pumping preserves the advantage of the optical pumping. It can separate the charge injection region from the light amplification region to prevent charge injection related losses. Meanwhile, it posesses the benefits of a direct electrically pumped laser. For instance, the small size of an LED dramatically reduces the size of the whole laser system. Moreover, the LED pumped organic laser will be current/voltage controlled with a price much lower than a diode laser pumped system. Low threshold operation and a need for high power LEDs are two critical challenges for achieving LED pumped organic lasers, both of which are investigated in thesis.

Additionally, the thesis discusses the possibility of short pulse and thereby high peak power operation from organic semiconductor lasers, since the broad emission spectra of organic semiconductors make them potential good gain media for

mode-locked lasers. Moreover, the short output pulse itself is attractive in applications such as fluorescence spectroscopy. One attractive route to short-pulse lasing is to include a saturable absorber in the laser resonator, which can either act to mode-lock the laser field or q-switch the resonator. Organic dyes have historically been used as saturable absorbers in liquid dye lasers and have potential for use with organic semiconductor lasers.

The thesis ends with an application-orientated study of chemosensing using organic semiconductor lasers. This study exploits the photophysics of semiconducting polymers to use the gain medium as the sensing element. Adsorbed nitroaromatic analyte molecules lead to a reversible quenching of the laser emission, allowing detection of the analyte at low vapour pressures.

The layout of the thesis is arranged as follows. A background introduction to organic semiconductors is given in **Chapter 2**. This explains how the conjugated molecular structure of organic semiconductors determines the electron delocalization and the photophyscial properties. Stimulated emission and energy levels for lasing are also discussed to justify the suitability of organic semiconductors as laser gain media. Different categories of organic semiconductors are presented to give an overview of the whole organic semiconductor family and potential for molecular design. In terms of resonators, emphasis is placed on diffractive resonators with detailed illustrations in the feedback mechanism.

Chapter 3 outlines the experimental methods and equipments used for characterizing organic semiconductor lasers, including basic photophysical properties such as absorption and emission measurements, and characterisation of stimulated emission through gain and loss measurements. The chapter also discusses cavity fabrication and laser characterisation.

Chapter 4 presents the first demonstration of an LED pumped organic semiconductor laser. Two big challenges are presented at the beginning: low output powers from LEDs and high lasing thresholds of organic lasers. To bridge the gap between these two issues, an attempt of focusing and pulsing the LED with two different commercial available diode laser drivers are discussed in this chapter. A range of polymers, polymer blends and copolymers are characterized and included in DFB resonators to lower laser thresholds. The first LED pumped polymer laser is presented in the final section of the chapter, serving as a new alternative pumping scheme for direct electrically pumped organic laser diodes [33].

A remaining problem in the performance of LED pumped polymer lasers is the limited power of the inorganic LED. In **Chapter 5**, a non-imaging concentrator is developed to improve the output power density of the LED. The luminescent concentrator is capable of varying the beam profile between the excitation and emission spots, through which a power density improvement can be achieved. With careful selection of materials and geometry for the luminescent concentrator, the output power density of the LED is increased significantly. This higher excitation level reduces the power requirements of the pump source, leading to a threshold reduction in organic semiconductor lasers [34].

Chapter 6 shows some initial attempts for building a passively mode-locked polymer laser. To distinguish from mode-locked solution organic dye lasers, solid state saturable absorbers are tested both experimentally and theoretically. As a preliminary study in controlling the laser dynamics, a saturable absorber is incorporated in an organic semiconductor laser cavity. The combination of the saturable absorber with an organic semiconductor gain medium results in a change in the output pulse profile, which is simulated theoretically to get an insight into the underlying physics.

The eventual goal of research on organic semiconductor lasers is to make them alternative new light sources in practical applications. Therefore, to complete the thesis, an investigation of organic semiconductor lasers for chemosensing nitro-aromatic compounds is presented in **Chapter 7**. Organic semiconductor DFB lasers based on polyfluorene are used to detect the explosive vapour 1,4-Dinitrobenzene (DNB) at a low vapour pressure of 10 ppb. The vapour molecules reversibly quench the light emission from the polymer laser. For the first time, the dynamics of laser emission during exposure and recovery cycles are recorded. This information is used to understand the interaction between the vapour molecules and the polymer chains.

Reference

[1] B. Bolto, R. McNeill, and D. Weiss, *Australian Journal of Chemistry*, 1963. **16**: p. 1090.

[2] C.K. Chiang, C.R. Fincher, Y.W. Park, A.J. Heeger, H. Shirakawa, E.J. Louis, S.C. Gau, and A.G. Macdiarmid, *Physical Review Letters*, 1977. **39**(17): p. 1098-1101.

[3] http://nobelprize.org/nobel_prizes/chemistry/laureates/2000/public.html.

[4] A.J. Heeger, *Reviews of Modern Physics*, 2001. **73**(3): p. 681-700.

[5] A.G. MacDiarmid, *Reviews of Modern Physics*, 2001. **73**(3): p. 701-712.

[6] C.W. Tang and S.A. Vanslyke, *Applied Physics Letters*, 1987. **51**(12): p. 913-915.

[7] J.H. Burroughes, D.D.C. Bradley, A.R. Brown, R.N. Marks, K. Mackay, R.H. Friend, P.L. Burns, and A.B. Holmes, *Nature*, 1990. **347**(6293): p. 539-541.

[8] A. Tsumura, H. Koezuka, and T. Ando, *Applied Physics Letters*, 1986. **49**(18): p. 1210-1212.

[9] G. Yu, J. Gao, J.C. Hummelen, F. Wudl, and A.J. Heeger, *Science*, 1995. **270**(5243): p. 1789-1791.

[10] D. Moses, *Applied Physics Letters*, 1992. **60**(26): p. 3215-3216.

[11] N. Tessler, G.J. Denton, and R.H. Friend, *Nature*, 1996. **382**(6593): p. 695-697.

[12] R.D. Xia, G. Heliotis, and D.D.C. Bradley, *Applied Physics Letters*, 2003. **82**(21): p. 3599-3601.

[13] G. Tsiminis, J.C. Ribierre, A. Ruseckas, H.S. Barcena, G.J. Richards, G.A. Turnbull, P.L. Burn, and I.D.W. Samuel, *Advanced Materials*, 2008. **20**(10): p. 1940-+.

[14] V.G. Kozlov, V. Bulovic, P.E. Burrows, and S.R. Forrest, *Nature*, 1997. **389**(6649): p. 362-364.

[15] S.V. Frolov, Z.V. Vardeny, and K. Yoshino, *Applied Physics Letters*, 1998. **72**(15):

p. 1802-1804.

[16] R.C. Polson, G. Levina, and Z.V. Vardeny, *Applied Physics Letters*, 2000. **76**(26): p. 3858-3860.

[17] Y. Kawabe, C. Spiegelberg, A. Schulzgen, M.F. Nabor, B. Kippelen, E.A. Mash, P.M. Allemand, M. Kuwata-Gonokami, K. Takeda, and N. Peyghambarian, *Applied Physics Letters*, 1998. **72**(2): p. 141-143.

[18] T. Riedl, T. Rabe, H.H. Johannes, W. Kowalsky, J. Wang, T. Weimann, P. Hinze, B. Nehls, T. Farrell, and U. Scherf, *Applied Physics Letters*, 2006. **88**(24): p. 241116.

[19] K. Forberich, A. Gombert, S. Pereira, J. Crewett, U. Lemmer, M. Diem, and K. Busch, *Journal of Applied Physics*, 2006. **100**(2): p. 023110.

[20] G.F. Barlow, A. Shore, G.A. Turnbull, and I.D.W. Samuel, *Journal of the Optical Society of America B-Optical Physics*, 2004. **21**(12): p. 2142-2150.

[21] G. Heliotis, R.D. Xia, G.A. Turnbull, P. Andrew, W.L. Barnes, I.D.W. Samuel, and D.D.C. Bradley, *Advanced Functional Materials*, 2004. **14**(1): p. 91-97.

[22] S. Stagira, M. Zavelani-Rossi, M. Nisoli, S. DeSilvestri, G. Lanzani, C. Zenz, P. Mataloni, and G. Leising, *Applied Physics Letters*, 1998. **73**(20): p. 2860-2862.

[23] M. Goossens, A. Ruseckas, G.A. Turnbull, and I.D.W. Samuel, *Applied Physics Letters*, 2004. **85**(1): p. 31-33.

[24] D. Schneider, T. Rabe, T. Riedl, T. Dobbertin, M. Kroger, E. Becker, H.H. Johannes, W. Kowalsky, T. Weimann, J. Wang, P. Hinze, A. Gerhard, P. Stossel, and H. Vestweber, *Advanced Materials*, 2005. **17**(1): p. 31-+.

[25] G. Heliotis, D.D.C. Bradley, M. Goossens, S. Richardson, G.A. Turnbull, and I.D.W. Samuel, *Applied Physics Letters*, 2004. **85**(25): p. 6122-6124.

[26] A. Rose, Z.G. Zhu, C.F. Madigan, T.M. Swager, and V. Bulovic, *Nature*, 2005. **434**(7035): p. 876-879.

[27] N.C. Giebink and S.R. Forrest, *Physical Review B*, 2009. **79**(7): p. -.

[28] J. Stehr, J. Crewett, F. Schindler, R. Sperling, G. von Plessen, U. Lemmer, J.M.

Lupton, T.A. Klar, J. Feldmann, A.W. Holleitner, M. Forster, and U. Scherf, *Advanced Materials*, 2003. **15**(20): p. 1726.

[29] H. Yamamoto, H. Kasajima, W. Yokoyama, H. Sasabe, and C. Adachi, *Applied Physics Letters*, 2005. **86**(8): p. 083502.

[30] B.K. Yap, R.D. Xia, M. Campoy-Quiles, P.N. Stavrinou, and D.D.C. Bradley, *Nature Materials*, 2008. **7**(5): p. 376-380.

[31] P. Gorrn, T. Rabe, T. Riedl, W. Kowalsky, F. Galbrecht, and U. Scherf, *Applied Physics Letters*, 2006. **89**(16): p. 161113.

[32] G.A. Turnbull, P. Andrew, W.L. Barnes, and I.D.W. Samuel, *Applied Physics Letters*, 2003. **82**(3): p. 313-315.

[33] Y. Yang, G.A. Turnbull, and I.D.W. Samuel, *Applied Physics Letters*, 2008. **92**(16): p. 163306-3.

[34] Y. Yang, I.D.W. Samuel, and G.A. Turnbull, *Advanced Materials*, 2009. **21**(31): p. 3205.

Chapter 2

Theory of Organic Semiconductor Lasers

2.1. Introduction

Laser is the acronym for 'Light amplification by Stimulated Emission of Radiation'. In 1917, Einstein established the theoretical foundation for the LASER. Nearly a half century later, the first laser based on Ruby was experimentally demonstrated [1]. Since then, lasers have found applications in various fields from pure science research, such as molecular spectroscopy to daily life in telecommunications, DVD players, displays, photocopiers and so on. The fundamental structure of a laser comprises two elements: a gain material and a feedback resonator. The resonator guides light into the gain medium which amplifies it by stimulated emission. There are many types of gain materials including solids, liquids and gases, which form the basis of gas-ion lasers, dye lasers, semiconductor lasers and solid-state lasers. Organic semiconductors with their unique properties of simple fabrication, wide absorption and emission spectra, and high luminescence efficiency make them promising gain media for a new class solid state laser.

In this chapter, the fundamental theory of organic semiconductor lasers is introduced. **Section 2.2** focuses on the gain medium, including the molecular structures of organic semiconductors (**Section 2.2.1**) and how this relates to their

electronic and optical properties (**Section 2.2.2**). A brief overview of different categories of organic semiconductors is given in **Section 2.2.3**. Based on a detailed discussion in stimulated emission, **Section 2.2.4** establishes the four-level energy diagram for organic semiconductor lasers. **Section 2.3** changes the subject from gain media to laser resonators. Different types of resonators are compatible with organic semiconductor lasers. Emphasis will be given in the most frequently used resonator, distributed feedback resonator (DFB), in **Section 2.3.2**, which forms the basis for the rest of the thesis. The chapter ends with a discussion on the simplification of the pumping schemes towards a compact solid state organic semiconductor laser system in **Section 2.3.3**.

2.2. Organic semiconductor

2.2.1. Molecular structure

The most common type of organic semiconductor used in lasers are semiconducting polymers. They are long chain conjugated molecules, made up of alternating single and double bonds between carbon atoms. Each carbon atom contains six electrons rotating in different orbitals surrounding the central nucleus. The inner most 1s orbital is occupied by two core electrons. The remaining four valence electrons sit with equal probability in the 2s and 2p orbitals, resulting in the final distribution of $1s^2\ 2s^2\ 2p^2$. The shapes of the s and p orbital are shown in Figure 2.1.

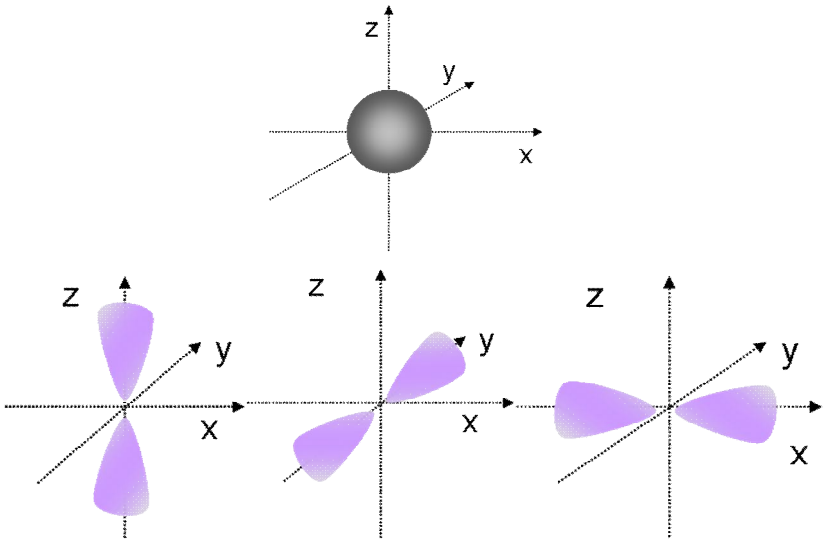

Figure 2.1. (Top) S orbital; (Bottom) P orbitals: p_z, p_y, p_x from left to right

The double bond in the conjugated chain is formed by orbital hybridization, when the wavefunctions of more than one carbon atom overlap spatially. A typical example of the double bond is ethylene (C_2H_4) (Figure 2.2). It is based on a hybridized sp^2 orbital, realized by mixing the 2s orbital and two of the three 2p orbitals. The three sp^2 orbitals lie in a plane, separated by 120 degrees from each other, represented by the two yellow and one blue lobes in the right graph of Figure 2.2. In ethylene, two of the sp^2 orbitals overlap with the hydrogen 1s orbitals to form σ C-H bonds. The other sp^2 orbital from each carbon atom forms the σ C-C bond. The remaining p orbital from each carbon atom overlaps to form a π bond. In this way, a C=C double bond is completed by one σ bond and one π bond. The long chain backbone of semiconducting polymers, such as polyacetylene (in Figure 2.3), similarly consist of σ and π bonds between adjacent carbon atoms. The π bonds are very important, since the electrons are weakly bonded to the nuclei and delocalized between the neighbouring carbon atoms. When forming a conjugated long chain, the overlapping of π bonds from all the double bonds extends the electron delocalization along the backbone [2].

Figure 2.2. Ethylene molecular structure: (left) formation of the double bonds; (right) three sp^2 orbitals and one p orbital from two carbon atoms

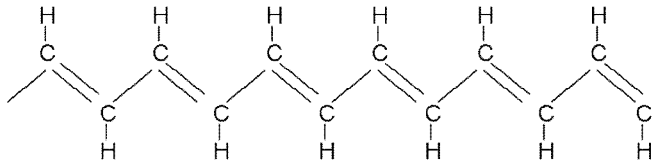

Figure 2.3. Polyacetylene

From the previous discussion, the p orbital is a critical element for electron delocalization. In each p orbital, a central node separates the upper and lower lobes which are in anti-phase with respect to each other: represented by the different colours in Figure 2.4. Due to the phase difference in the upper and lower lobes, the interaction between two p orbitals can be either constructive or destructive, depending on whether they are combined in phase or out of phase. If combined in phase, in other words a constructive interaction, π orbitals will be formed. Otherwise, for a destructive interaction, anti-bonding π^* orbitals will be generated. The π orbital is lower in energy than the π^* orbital, creating two energy states separated by an energy gap. The energy levels of these states can be estimated from the Hückel approximation. In the conjugated long chains of a semiconducting polymer, a large number of pairs of π orbital and π^* orbital with different energy gaps exist. A much more complicated energy structure is formed. It consists of two ladders of discrete π and π^* orbitals with a wide energy gap in between. The total number of energy states is proportional to the number of p electrons, as the case for ethylene.

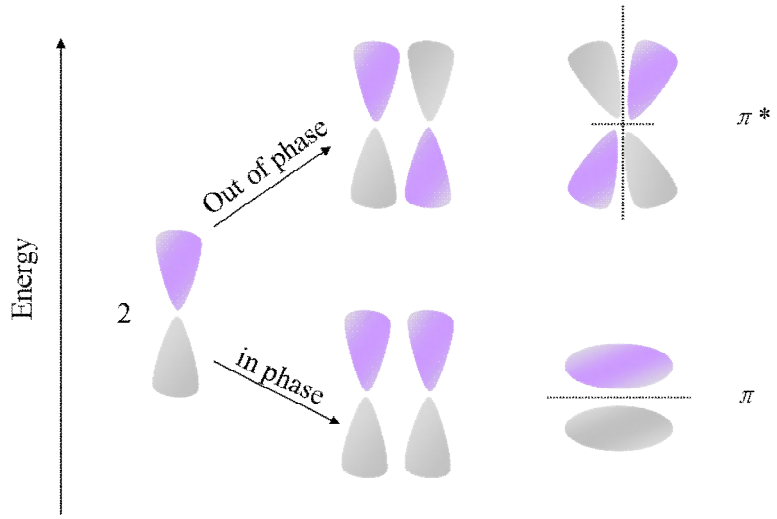

Figure 2.4. π orbital and π^* orbital

Each π orbital or π^* orbital can be occupied by two electrons with different spins. The highest occupied π orbital is called the HOMO (Highest Occupied Molecular Orbital) and lowest empty π^* orbital is called the LUMO (Lowest Unoccupied Molecular Orbital). Therefore, the energy gap is the energy difference between the HOMO level and the LUMO level:

$$E_g = E_{LUMO} - E_{HOMO} \qquad \textbf{2.1.}$$

2.2.2. Optical properties

The electronic π-π^* transition is responsible for the absorption and emission in organic semiconductors. To a first approximation, the electron wavefunction in the conjugated chain can be viewed as a free electron confined in a one dimensional quantum well, where the width of the well is equal to the length of the conjugated chain. From this assumption, according to quantum mechanics, the energy gap between π orbital and π^* orbital is determined by the length of the conjugated chains. The longer the conjugated chain, the narrower the energy gap between the two orbitals. Figure 2.5 gives an example of the impact of chain length,

represented by the number of the double bonds (monomer unit), on the HOMO-LUMO gap in poly(2,5 dioctyloxy p-phenylenevinylene) (DOO-PPV).

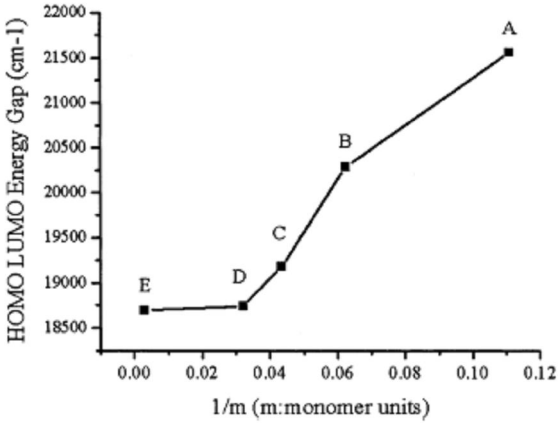

Figure 2.5. The impact of monomer units on the energy gap in DOO-PPV [3]

When an electron in the HOMO level is excited to the LUMO level by absorbing an incident photon, a positively charged hole is left in the HOMO level. The positively charged hole and negatively charged electron forms an excited state called an exciton, bound together by the Coulomb force. The binding energy of excitons in organic semiconductors is large (~0.5 eV), compared to their inorganic counterparts. Hence, these excitons are strongly bound at room temperature and show little temperature dependence[4].

Depending on the spin states, the interaction between the electron and hole can form singlet or triplet excitons, as shown in equation 2.2. A singlet exciton is created by electrons with anti-symmetric spin wavefunctions, hence the overall angular momentum is zero. On the other hand, the triplet exciton includes electrons possessing symmetric spin wavefunctions, resulting in the overall angular momentum to be one. The spin-conservation principle requires that spin must be conserved in electronic transitions. Therefore, under normal circumstance, only singlet to singlet or triplet to triplet transitions are allowed [5].

$$\text{Singlet} = \frac{1}{\sqrt{2}}(|\uparrow\downarrow\rangle - |\downarrow\uparrow\rangle) \qquad \text{Triplet} = \begin{matrix} |\uparrow\uparrow\rangle \\ \frac{1}{\sqrt{2}}(|\uparrow\downarrow\rangle + |\downarrow\uparrow\rangle) \\ |\downarrow\downarrow\rangle \end{matrix} \qquad \textbf{2.2.}$$

The absorption and emission in organic semiconductors can be explained by electrical transitions, as illustrated in Figure 2.6.

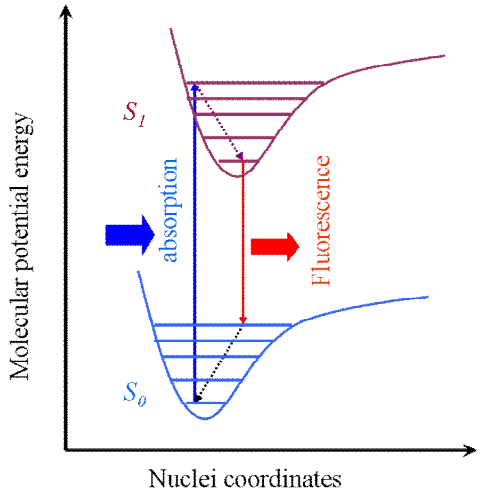

Figure 2.6. Excitonic energy diagram for optical transitions

For simplicity, only two electronic states, the ground singlet state S_0 and the first excited singlet state S_1, are shown in the diagram. The vibrations between the nuclei divide each singlet state into many sub-level vibrational states. According to the Franck-Condon principle, the electronic transition happens much faster than the nuclei can respond, since the nuclei are heavier than the electrons. As a result, the nuclear framework remains constant during the electronic transition. Only vertical transitions (the solid lines) occur between the two electronic states. The vertical transition excites the molecule from the ground state to a higher vibrational state in the first excited singlet state. The excited molecule then rapidly relaxes non-radiatively from the higher vibrational state to the lowest vibrational state of S_1 (the dotted lines). When it arrives at the lowest vibrational state in the first excited singlet state, the energy required to be dissipated for the electron

returning to the ground singlet state is larger than the energies that can be accepted by the surrounding molecules through collision. Consequently, the excited molecule remains in the lowest vibrational level in S_1 for a relatively long time until it decays to the vibrational level in the ground state via fluorescence by the Franck-Condon principle [6]. The emission spectrum is red shifted, in comparison to the absorption, due to the different energy gaps between the two transitions. The red shift, or Stokes shift, arises from the change of the nuclei positions and thus the potential between the electronic transitions. Other factors can also contribute to the red shift, such as the molecular environments. This is particularly the case for long chain conjugated polymers. The environment of disorder in polymers leads to conjugated chains with different lengths in different locations to form various localized energy states. When the sample is excited by a broadband light source, all the energy sites can be excited to their excited states. However, excitons in the higher energy localized states transfer their energies quickly to the lowest energy states through non-radiative dipole-dipole interactions. The excitons in the lowest localized exited state will finally decay back to the ground state by emitting a photon. In this manner, the red shift of the emission spectrum can be enhanced, in comparison to the case of a uniform molecular environment [7-10].

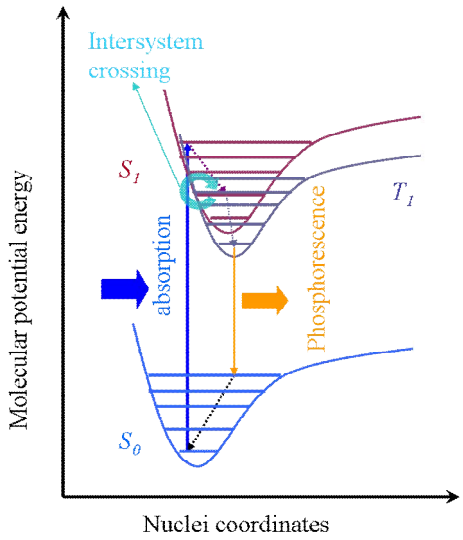

Figure 2.7. Phosphorescence energy diagram

In some materials, phosphorescence from the triplet state can also contribute to the output emission, as indicated in Figure 2.7. When a molecule is excited to the first excited singlet state, if the triplet excited state shares a common geometry with the excited singlet state at the place where their potential curves intersect, intersystem crossing can occur via a spin flipping mechanism between the single and triplet state. Hence, the exciton can transfer from the excited singlet state to the excited triplet state. The transition from the triplet state to the ground singlet state is formally spin forbidden so that the molecule is trapped in the triplet state. However, with the help of the spin flipping mechanism, the transition from the triplet state to the ground single state can be eventually completed by weak phosphorescence emissions. In most organic semiconductors, phosphorescence is very inefficient process because the non-radiative decay is much faster. Efficient phosphorescence is only observed in organic semiconductors containing heavy metal atoms [11-12].

2.2.3. Types of organic semiconductors

Besides the semiconducting polymers, organic semiconductors can be categorized into several types according to the molecular structures and processing methods, as shown in Figure 2.8. Early research was focused on crystallized organic semiconductors, like anthracene (Figure 2.8 (a)) [13]. The high voltage needed for producing fluorescence and the difficulty in fabrication make these materials less attractive. Only after the discovery of small molecule organic semiconductors, which can be fabricated by thin film evaporation, did organic semiconductors become an attractive subject for study. Figure 2.8 (b) gives an example of a typical small molecule material called aluminum tris(quinolate) (Alq_3) [14]. Compared to small molecule materials, the previous discussed semiconducting polymers have the benefit of being solution processible. They are compatible with

spin coating and inkjet printing techniques, dramatically simplifying device fabrication. Two families of polymers, namely poly(phenylenevinylene)s (PPVs)[15-17] (Figure 2.8 (c)) and polyfluorenes [18-20] (Figure 2.8 (d)), have been widely studied during the past twenty years due to their great potential as light emitting materials for lasers and LEDs. Another two more recently studied types of organic semiconductors are conjugated dendrimers and spiro-compounds. The distinctive feature of conjugated dendrimers, such as the 1st generation dendron with bis-fluorene core [21]shown in Figure 2.8 (e), is the separated control of light emission and solubility. The central chromophore core defines the emission wavelength, while the surrounding dendrons with surface groups confer solubility. The branched structure effectively prevents aggregation quenching at high concentration by keeping the chromophores apart [22-23]. Oligomers have a molecular structure between the long chain polymers and small molecules and contain limited number of the repeating units. Figure 2.8 (f) shows a molecule formed by two oligomers coupling to each other with a spiro linkage [24-25].

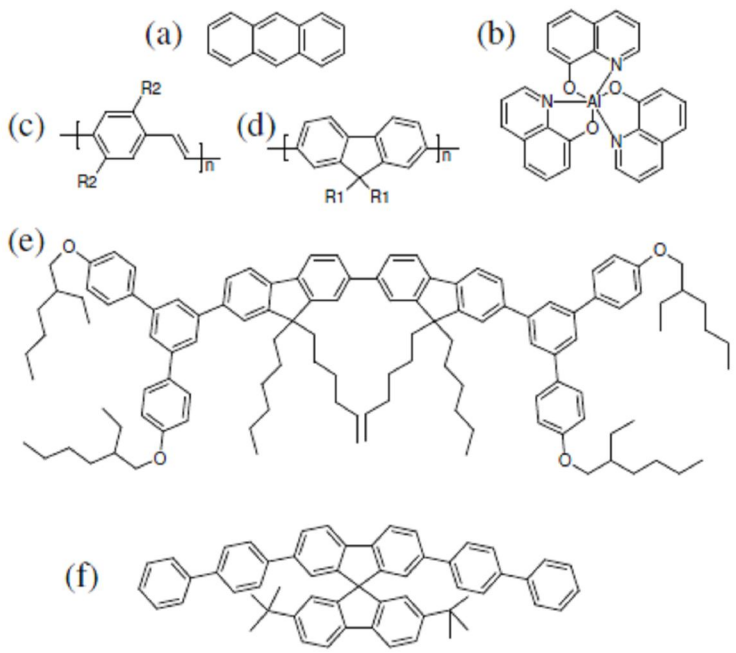

Figure 2.8. Different types of organic semiconductors ([26])

2.2.4. Stimulated emission

A two level energy system is sufficient to illustrate the fundamental phenomena when an incident electromagnetic wave interacts with a material. Figure 2.9 describes the three kinds of optical transitions involved in the interaction, namely spontaneous emission, stimulated emission and absorption[27].

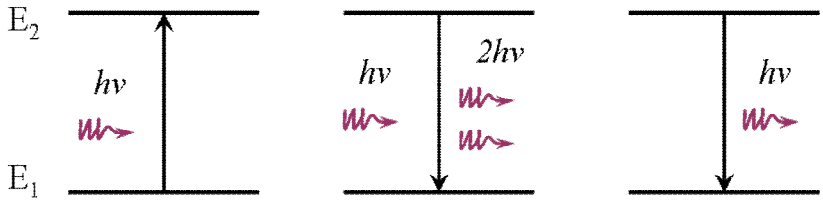

Figure 2.9. (left) Absorption; (middle) Stimulated emission; (right) Spontaneous emission

When a photon with energy equal to the energy difference between the excited state (E_2) and ground state (E_1) propagates through a material, it can be absorbed by raising an electron in the ground state to the excited state. The frequency of the photon must satisfy the following equation:

$$h\nu = E_2 - E_1 \qquad \textbf{2.3.}$$

where h is Planck's constant.

The change of the excited state (N_2) population because of absorption is determined by:

$$\frac{dN_2}{dt} = B_{12}\rho N_1 \qquad \textbf{2.4.}$$

In equation 2.4, B_{12} is the Einstein 'B' coefficient related to the absorption cross section and ρ is the photon density.

The excited electron will relax back to the ground state, accompanied by the emission of a photon with energy determined by equation 2.3 (right graph in Figure 2.9). The exact time at which the electron will return to the ground state is random and thereby the light emitted in this way is incoherent. The change of population density in the excited state due to such spontaneous emission is given by:

$$\frac{dN_2}{dt} = -AN_2 \qquad \textbf{2.5.}$$

A is Einstein 'A' coefficient, representing the spontaneous emission probability. *1/A* is referred to as the characteristic spontaneous emission lifetime of the material.

Alternatively, the electron in the excited state can be triggered by an incoming photon to relax back to the ground state (middle graph in Figure 2.9). The emitted photon will have the same energy, phase, and propagation direction as the incident photon. Consequently, the incoming photon is amplified coherently. Similar to equation 2.5, this stimulated emission can be described by:

$$\frac{dN_2}{dt} = -B_{21}\rho N_2 \qquad \textbf{2.6.}$$

Where B_{21} is Einstein 'B' coefficient, describing the stimulated emission cross section.

If both the absorption and stimulated emission are taken into account, for the incoming light, as it passes through the material in the *z* direction, the change in photon density is given by

$$\frac{d\rho}{dz} = B_{21}\rho N_2 - B_{12}\rho N_1 \qquad \textbf{2.7.}$$

In equation 2.7, spontaneous emission is neglected, since it is incoherent with the incident photon. If the degeneracies are equal for the two energy states, $B_{21} = B_{12}$. Equation 2.7 can be rearranged into:

$$\frac{d\rho}{dz} = B_{21}\rho(N_2 - N_1) \qquad \textbf{2.8.}$$

If the population in the excited state is larger than that in the ground state ($N_2 > N_1$), the incident photon experiences amplification as it passes through the material. Otherwise, it is absorbed. In thermal equilibrium, the populations in the energy states approximately follow Boltzmann statistics:

$$\frac{N_2}{N_1} = \exp[-\frac{(E_2 - E_1)}{kT}] \qquad \textbf{2.9.}$$

where k is Boltzmann's constant and T the absolute temperature.

It is obvious that under equilibrium, N_1 is always larger than N_2 and thus equation 2.8 leads to a net absorption. To create a situation with the upper state population larger than the lower state (called population inversion), three or four energy levels should be involved. The electronic states of organic semiconductors shown in Figure 2.6 can be treated as four level energy system, since the higher vibrational energy states in both the ground and excited electronic states have much shorter lifetime than lowest vibrational states. Figure 2.10 gives a simplified energy diagram.

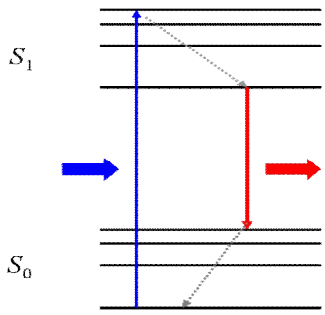

Figure 2.10. Simplified energy diagram of an organic semiconductor

In Figure 2.10, the blue arrow represents the incident photon. It is absorbed by exciting the electron from the ground singlet state to a higher vibrational level in the first singlet state. The dotted arrows indicate the fast relaxation of the electrons among the vibrational levels. Radiative decay from the first single state to a higher vibrational level in the ground state is indicated by the red arrow. A population inversion can be achieved between the lowest level of the first excited state and the higher vibrational levels in the ground state due to the fast vibrational relaxation in the ground state. Such relaxation quickly depletes the population in the higher vibrational levels in the ground singlet state.

However, population inversion can not be achieved easily. The existence of other competing mechanisms can deplete the electrons in the first excited singlet state and therefore weaken the population inversion. For instance, photo-induced absorption can pump the electrons from the first excited state to a higher singlet state. Also, exciton-exciton annihilation can occur at high pump rates, depleting the excited state population. In exciton-exciton annihilation, one exciton is scattered into a higher energy state, while the other is scattered to a lower energy state. Moreover, chemical defects or impurities can act as localized quenchers, setting up fast non-radiative paths to transfer the electrons from the singlet states to the quencher states. A commonly observed quencher is the carbonyl group formed during photoxidation [10, 15, 28-32].

When the gain medium is placed into a laser cavity, apart from the need for a population inversion, laser action can be achieved only when the round trip loss inside the resonator is lower than the round trip gain. Ground state absorption from the gain medium contributes to one of the cavity loss mechanisms in organic semiconductor lasers. This loss results from the spectral overlap between the absorption and photoluminescence spectra. One effective approach of reducing

this reabsorption loss is to increase the Stokes shift between the absorption and emission spectra, by blending two materials with different energy gaps. In the blend, light absorbed by the wider gap material can be emitted from the other material via a non-radiative Forster energy transfer between them [33-36]. Similar to blends, copolymers, consisting of wider and narrower band gap segments, can also be useful for separating absorption and emission spectra [37-38].

2.3. Organic semiconductor lasers

2.3.1. Introduction

The first organic semiconductor laser was reported in 1992 [39], based on an MEH-PPV solution. The laser had a quantum efficiency comparable to the rhodamine 6G dye lasers. Four years later, solid state organic semiconductor lasers were demonstrated [40-42]. There are several similarities between organic semiconductor lasers and organic dye lasers. For instance, both of them are solution processible materials and lase in the visible spectrum range with wide wavelength tunability. The main difference is that organic semiconductors can exhibit high quantum yield in neat films of high concentration. In contrast, organic dyes require dilution in a passive matrix material such as polystyrene to give reasonable photoluminescence quantum yield at high concentration. Therefore, organic semiconductors offer a scope for stronger pump-absorption and higher gain in solid thin films than organic dyes. Additionally, the electron delocalization in organic semiconductors supports charge transport, making compact and low cost electrically pumped organic laser diodes a future possibility.

Organic semiconductor lasers also share some similarities with inorganic semiconductor lasers. Both lasers can achieve high quantum yield in solid state and are capable of charge transport. However, compared to inorganic

semiconductors, the highly disordered molecules in organic semiconductors lead to much lower carrier mobilities, increasing the difficulty for electrically pumped laser. The exciton binding energy in organic semiconductors is much larger than that typical in inorganic semiconductors. Consequently, organic semiconductor lasers show very little temperature dependence in lasing thresholds and slope efficiencies, unlike their inorganic counterpart which are strongly temperature dependent [4]. The most important advantage of organic semiconductor lasers is the simple fabrication which usually involves spin coating or dip coating. For inorganic semiconductor lasers, the fabrication processes are much more complicated, including the growth of gain layers with epitaxy techniques like molecular beam epitaxy (MBE) that are expensive and time consuming.

2.3.2. Organic semiconductor laser resonators

A laser is comprised of two fundamental elements: a gain medium and a feedback resonator. The resonator circulates the internal beam through the gain medium for amplification by stimulated emission to establish an intense and coherent optical field. A simple example of a laser resonator includes two mirrors with a gain medium in the middle. This behaves as a Fabry-Perot interferometer with a standing-wave optical field formed between the two mirrors. A more complicated case is a ring resonator within which circulates a travelling wave. Figure 2.11 shows the geometries of these two basic types of resonators. Each of these resonators selects the resonant wavelengths of the internal optical field, according to the principle that the amplitude and phase of the laser field must not change following each complete round trip of the cavity. Additionally, the cavity requires the transverse mode pattern of the optical field to be self-replicated for each round trip and hence determines the output laser beam pattern [43].

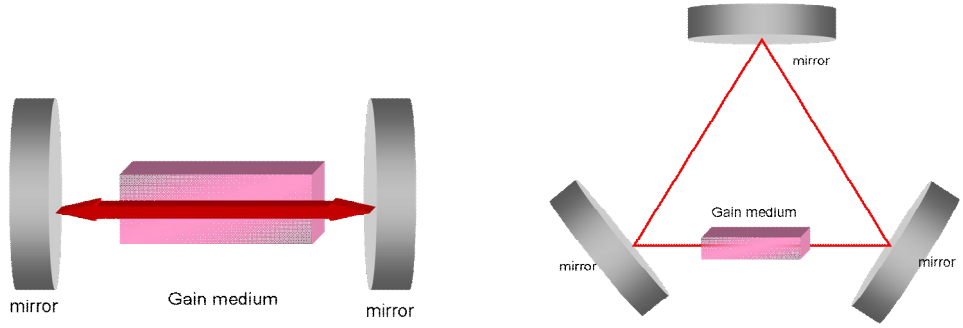

Figure 2.11. (left) Linear Fabry-Perot resonator and (right) ring resonator

Taking the simple Fabry-Perot cavity as an example (left diagram in Figure 2.11), the wavelengths of the standing-waves formed between the two mirrors should be equal to an integral number of the fundamental wavelength determined by the round trip optical length of the cavity:

$$m\lambda = 2nL \qquad \textbf{2.10.}$$

where m is an integer; n is the refractive index of the material filled inside the cavity; and L is the cavity length. These frequencies are known as the longitudinal or axial modes of the resonator. Accordingly, the spectral separation (Free Spectral Range) between each longitudinal mode should be

$$FSR = \Delta\nu = \frac{c}{2nL} \qquad \textbf{2.11.}$$

$$\delta\lambda = \frac{\lambda^2}{2nL} \qquad \textbf{2.12.}$$

Organic semiconductors can be processed into various kinds of resonators due to their ease of fabrication. Early research focused on microcavities, usually comprising a thin organic layer between two Bragg reflectors or one Bragg reflector and a metal mirror [44-45]. This functions as a conventional linear Fabry-Perot resonator. However, the interaction length between the optical field and the gain medium is determined by the film thickness (~ 100s nm) of the organic semiconductor layer. Therefore, single-pass gain is very limited in

microcavities. When the cavity length is small enough to support just the fundamental mode $\lambda = 2nL$, the cavity can strongly modify the spatial distribution of spontaneous emission through interference effects, resulting in an increased stimulated emission cross section and a lower lasing threshold [46]. If the microcavity were only to support one axial mode and no lateral modes in the plane, then it has the capability of giving thresholdless lasing.

An alternative to microcavity is a Fabry-Perot waveguide resonator, which is widely used in inorganic semiconductor lasers. In the waveguide resonator, the feedback is provided in-plane by the two edges of the organic thin film. In comparison to microcavities, the interaction length between the optical field and the gain medium in waveguide cavities can be improved to a few millimetres, depending on the size of the pump beam. This resonator simplifies the fabrication process, since it excludes the complex Bragg mirrors used in the microcavities. This approach is very popular in inorganic semiconductor lasers, because the high refractive indices can give high reflectivity from the well-cleaved edges. However, organic semiconductors have much lower refractive indices and the cut edges are usually too rough to provide strong optical feedback. To date, only small molecule materials, deposited by evaporation, have been proven compatible with waveguide cavities. Lasing was observed at reasonable low threshold (1 $\mu J/cm^2$) because of the long gain region (1 mm) [4, 47-48].

Nowadays, the most popular resonators for organic semiconductor lasers are diffractive periodic cavities. These are compatible with spin coating, which preserves the simple fabrication property of organic semiconductors. Unlike conventional resonators, diffractive resonators do not require cavity mirrors or high quality waveguide facets. Instead, the feedback is provided by a periodic microstructure that diffracts the propagating light into different angles. The

scattered light can add coherently from the periodic modulation and propagates in a new direction. The diffraction angle, or Bragg scattering angle, is highly wavelength dependent. Many diffractive microstructures have been studied for organic semiconductor lasers, such as distributed feedback (DFB) structure in one dimension (1D) [38, 49], two dimension (2D) [50-51], 3D photonic crystal structures [52-53] and concentric circular gratings [54-56]. In the following, the discussion will focus on the 1D and 2D DFB resonators, since they are the basic resonators used in the rest of the thesis.

Figure 2.12 gives two examples of 1D and 2D DFB lasers, formed by a thin organic layer spin coated on corrugated periodic substrates. The 1D DFB cavity is formed by a periodic surface grating in one dimension so that feedback, in other words light diffraction, occurs in the direction perpendicular to the grating grooves. In the 2D DFB cavity shown, periodic corrugations are along two perpendicular directions, providing feedbacks in both directions. More generally, the shapes of the 2D DFB periodic microstructure can be square [57], hexagonal[58] and honeycomb lattices [59].

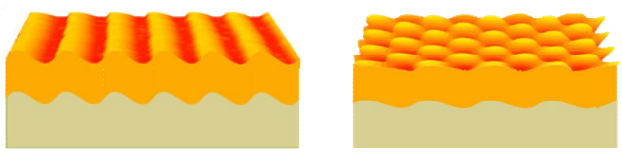

Figure 2.12. Examples of 1D (left) and 2D (right) DFB resonators

The feedback mechanism in DFB resonators can be well explained by the perturbation equations from coupled-wave theory [60]. In principle, this describes the coupling between the counter-propagating modes as they travel through the waveguide layer. The periodic structure acts as a spectral selection mechanism to achieve lasing at only discrete wavelengths. One important conclusion from the coupled-wave theory is that the lowest threshold appears at wavelengths close to

the Bragg wavelengths (shown in equation 2.13). It is at these wavelengths that the coupling between the two counter-propagating waves establishes standing waves inside the waveguide layer. Therefore, the interaction between the light and the gain medium is maximized. The Bragg condition is described as:

$$m\lambda = 2n_{eff}\Lambda \qquad \textbf{2.13.}$$

m is the diffraction order; n_{eff} is the effective refractive index of the waveguide modes supported by the thin organic layer; Λ is the period of the microstructure. When m = 1, the laser is called a "first-order" DFB laser with its output and feedback are both provided in-plane by first order Bragg scattering from the microstructure. In this case, the laser beam is emitted from the edge of the film and hence is very divergent. The most useful and convenient cavity is a surface emitting resonator, which can be achieved by using m=2. This second order lasing gives output coupling normal to the film via first order diffraction from the microstructure, while feedback is provided by second order scattering.

As mentioned above, the periodic microstructure functions as a diffraction grating. It couples the light guided by the thin organic layer into free-space light waves, propagating at different angles. During this diffraction process, the in-plane momentum between the guided mode (k_{mode}) and the sum of the reciprocal lattice of the grating and the radiated wave must be preserved [61]:

$$k_{\text{mode}}^2 = (mk_{Gx} - k_0 \sin\theta \cos\phi)^2 + (pk_{Gy} - k_0 \sin\theta \sin\phi)^2 \qquad \textbf{2.14.}$$

where k_{Gy} and k_{Gx} are the wave vectors of the reciprocal lattice of a square array diffraction Bragg grating along two perpendicular directions. θ is the output coupling angle of the radiative mode and Φ is the in-plane angle, as indicated in Figure 2.13.

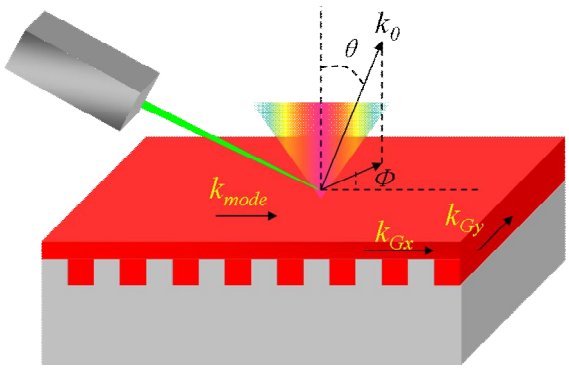

Figure 2.13. Scattering of the periodic gratings

A diagram in vector space can be more straightforward and useful to illustrate the in-plane momentum conservation.

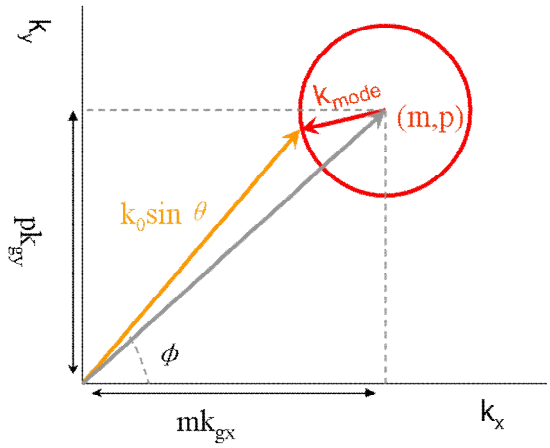

Figure 2.14. vector space for momentum conservation ([61])

In vector space, the unscattered guide mode is represented by a circle with radius equal to $\frac{2\pi n_{eff}}{\lambda}$ located at the origin. Following an mth order diffraction by the periodic grating with wave-vector of k_{gx} along k_x axis, and a pth order diffraction by grating vector of k_{gy} along k_y axis, the circle is displaced in k-space to a new coordinate (mk_{gx}, pk_{gy}) as shown in Figure 2.14. If the scattered wave vectors lie within a radius $\frac{2\pi}{\lambda}$ of the origin, the light will be coupled to free space. The resulting in-plane wave vector would be $k_0 sin\theta$, according to the momentum conservation. So, the light will be coupled out of the thin layer at a polar angle θ

which depends on the azimuth angle Φ (Figure 2.13). The relationship between the output wavevectors and their energies reveals the dispersion relationship in the diffractive resonator. This can be measured experimentally via an angle-resolved photoluminescence measurement[62].

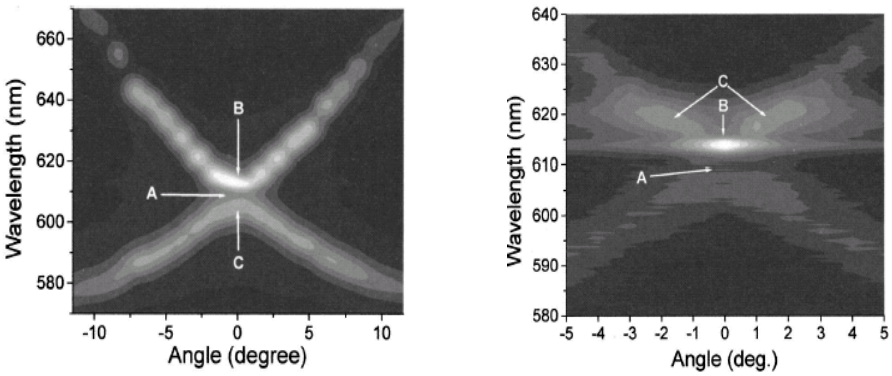

Figure 2.15. Angle resolved PL measurement for PL (left); lasing (right)

([62] Copyright 2010 by The American Physical Society)

The dispersion curve, shown in the left of Figure 2.15, indicates a stop band at A, a dark region arising from the destructive interference between the counter-propagating waveguide modes. The edges of the stop band (B and C) show zero group velocity, meaning standing waves form inside the thin organic layer. Lasing occurs at the edge of the stop band, indicated by the bright spot at B in the right plot of Figure 2.15, due to the largest gain it experienced, in comparison to other travelling waves that spent less time in the waveguide layer.

The stronger feedback in two orthogonal directions in 2D DFB resonators than in 1D DFB resonators often gives lower lasing thresholds. A detailed comparison of lasing spectrum and threshold between 1D and 2D DFB resonator has been demonstrated in polyfluorene lasers by Heliotis [63]. It shows that lasing threshold can be reduced by a factor of 20 with the use of a 2D DFB resonator. Besides the lasing threshold, the pattern of the output beam is different. The

emission from 1D DFB laser forms a double-lobe fan pattern with polarization parallel to the grating grooves. The two lobes of the output beam are in anti-phase and are significantly divergent parallel to the direction of the grating grooves due to the lack of optical confinement. For 2D DFB lasers, the emission pattern is formed by coherent interference between the two double-lobed outputs from the two perpendicular 1D gratings. So, a donut shape pattern, (or cross shape at high pump levels), is often observed. The beam is near diffraction limited and has an azimuthal polarization [63-65].

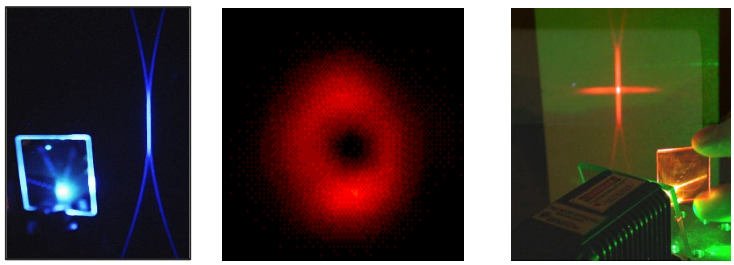

Figure 2.16. Emission patterns of 1 D (left) resonator and 2 D DFB resonator at low (middle) and high (right) pump energy

2.3.3. Pumping sources for organic semiconductor lasers

At present, organic semiconductor lasers are optically pumped by pulsed sources. Continuous-wave (CW) light sources are not suitable due to the short exciton lifetimes (between hundreds of picoseconds and a few nanoseconds). Also, non-radiative decay from intersystem crossing and exciton-exciton annihilation can generate long lived states like triplets, polarons or excimers whose absorption spectra overlap with the lasing wavelength and therefore increase the cavity loss. Consequently, the repetition rate of the pump source should be low enough to give any population of these states enough time to decay before the next excitation pulse.

Prior to the work in this thesis, all organic lasers used a second laser to pump them. The pump laser (usually expensive and big in size), complicates the organic semiconductor laser system, limiting its attractive feature as a low-cost and compact laser source. In recent years, the lasing threshold of organic semiconductor lasers have been gradually reduced with improved materials and resonators. For example, DFB lasers based on polyfluorene decreased the threshold energies down to hundreds of pico-Joules [38, 66-67]. The reduced lasing threshold, in turn, lowers the power requirement from the pump sources, making smaller and less powerful lasers possible excitation sources. The size of the pump sources reduced from a regenerative amplifier [40] to a mobile phone sized microchip laser [64] and further down to a InGaN diode laser [68].

Direct electrical excitation of the gain medium would greatly simplify the organic semiconductor laser system. However, many challenges exist for achieving electrical excitation. Firstly, the current optically pumped lasing thresholds are still too high, if they are converted to current densities for electrical injection. For instance, a threshold of 160pJ/pulse obtained from a 2D DFB laser [67] would be equivalent to 5018A/cm^2, if the exciton lifetime of 800ps for the gain medium is used and assuming 25% of the injected electrons form singlet excitons. Such a high current density can cause enormous heat in the gain medium and damage the material before lasing can be achieved. To solve the problem, higher carrier mobilities in organic semiconductors are required. Recent developments in organic semiconductors show current densities as high as 12000A/cm^2 can be injected into thin films with a thermal conductive substrate [69], although these materials were not efficient light emitters. A simultaneous optimization of carrier mobility and optical gain has also been demonstrated lately on polyfluorene derivatives [70].

Apart from carrier mobility, another obstacle preventing electrical pumping are the electrodes. The metal electrodes strongly absorb the visible photoluminescence from organic semiconductors, acting as an additional loss mechanism in the cavity. Lasing thresholds with electrodes are usually much higher than the case without electrodes. This indicates that an even higher threshold current density is required for electrical excitation than the already high value estimated from optically pumped lasing thresholds. Many efforts have been made to reduce the electrode related loss by minimizing the overlap between the optical modes and the electrodes. The solutions include thick gain layer [71], higher transverse mode lasing [72]. A final obstacle of realizing electrical excitation is the absorbing species present in organic electroluminescent devices. For example, only around 25% of the carriers combine to form singlet excitons, with three quarters of the carriers forming triplets. These triplets can absorb the radiative emission from singlet excitons. Additionally, the charge carriers themselves (polarons) can also absorb the emission from singlets, wiping out the optical gain. All these challenges discussed above must be solved simultaneously to achieve electrically excited organic lasers. Therefore, the path leading to direct electrically excited organic laser diodes still has far to go and requires a great deal of effort.

An alternative approach to electrically pumped organic laser diode is using inorganic LED as the pump source (This is the topic of **Chapter 4**). Driven by the lighting industry, the development of GaN technology has been extremely fast in recent years and has greatly improved the LED output power densities. The combination of inorganic GaN LEDs and organic semiconductor lasers would surpass all the additional losses associated with electrically pumped organic lasers by separating the charge injection region from the light amplification region. Additionally, it would reduce the system cost by a factor of 100, compared to

diode laser pumped organic lasers. Also, it should have the same simplicity of an direct electrically pumped laser. For instance, it is very compact in size and controlled by varying the drive current or voltage. Therefore, although it still belongs to an optical pumping scheme, LED excitation, as described in **Chapter 4**, could be the future for achieving compact and low cost organic semiconductor lasers.

2.4. Reference

[1] Haiman.T.H., *Nature* 1960. **187**: p. 493-494.

[2] G. Clayden, Warren, and Wothers, *Organic chemistry*. 2001: Oxford university press Inc., New York.

[3] J.H. Hsu, M.T. Hayashi, S.H. Lin, W.S. Fann, L.J. Rothberg, G.Y. Perng, and S.A. Chen, *Journal of Physical Chemistry B*, 2002. **106**(34): p. 8582-8586.

[4] V.G. Kozlov, V. Bulovic, and S.R. Forrest, *Applied Physics Letters*, 1997. **71**(18): p. 2575-2577.

[5] W.Butting, *Physics of organic semicondcutors*. 2005: Wiley-VCH Verlang GmbH.

[6] P. Atkins. and J. Paula., *Physical chemistry*. 2006: Oxford university press.

[7] I.D.W. Samuel, B. Crystall, G. Rumbles, P.L. Burn, A.B. Holmes, and R.H. Friend, *Synthetic Metals*, 1993. **54**(1-3): p. 281-288.

[8] R. Kersting, U. Lemmer, R.F. Mahrt, K. Leo, H. Kurz, H. Bassler, and E.O. Gobel, *Physical Review Letters*, 1993. **70**(24): p. 3820-3823.

[9] G.R. Hayes, I.D.W. Samuel, and R.T. Phillips, *Physical Review B*, 1995. **52**(16): p. 11569-11572.

[10] A. Ruseckas, M. Theander, L. Valkunas, M.R. Andersson, O. Inganas, and V. Sundstrom, *Journal of Luminescence*, 1998. **76-7**: p. 474-477.

[11] M.A. Baldo, M.E. Thompson, and S.R. Forrest, *Nature*, 2000. **403**(6771): p. 750-753.

[12] G.J. Hedley, A. Ruseckas, and I.D.W. Samuel, *Chemical Physics Letters*, 2008. **450**(4-6): p. 292-296.

[13] V.A.B. O.S.Avanesjan, V. K. Brikenstein, V. L. Broude, L. I. Korshunov, A. G. Lavrushko, Tartakovskii *II Molecular Crystals and Liquid Crystals*, 1974. **29**: p. 165-174.

[14] C.W. Tang and S.A. VanSlyke, 1987. **- 51**(- 12): p. - 915.

[15] G.J. Denton, N. Tessler, N.T. Harrison, and R.H. Friend, *Physical Review Letters*, 1997. **78**(4): p. 733-736.

[16] M.A. DiazGarcia, F. Hide, B.J. Schwartz, M.D. McGehee, M.R. Andersson, and A.J. Heeger, *Applied Physics Letters*, 1997. **70**(24): p. 3191-3193.

[17] W. Holzer, A. Penzkofer, S.H. Gong, A.P. Davey, and W.J. Blau, *Optical and Quantum Electronics*, 1997. **29**(7): p. 713-724.

[18] G. Heliotis, R. Xia, D.D.C. Bradley, G.A. Turnbull, I.D.W. Samuel, P. Andrew, and W.L. Barnes, *Applied Physics Letters*, 2003. **83**(11): p. 2118-2120.

[19] R.D. Xia, G. Heliotis, and D.D.C. Bradley, *Applied Physics Letters*, 2003. **82**(21): p. 3599-3601.

[20] M. Theander, T. Granlund, D.M. Johanson, A. Ruseckas, V. Sundstrom, M.R. Andersson, and O. Inganas, *Advanced Materials*, 2001. **13**(5): p. 323-327.

[21] J.R. Lawrence, G.A. Turnbull, I.D.W. Samuel, G.J. Richards, and P.L. Burn, *Optics Letters*, 2004. **29**(8): p. 869-871.

[22] P.W. Wang, Y.J. Liu, C. Devadoss, P. Bharathi, and J.S. Moore, *Advanced Materials*, 1996. **8**(3): p. 237.

[23] S.C. Lo, T.D. Anthopoulos, E.B. Namdas, P.L. Burn, and I.D.W. Samuel, *Advanced Materials*, 2005. **17**(16): p. 1945.

[24] T. Spehr, A. Siebert, T. Fuhrmann-Lieker, J. Salbeck, T. Rabe, T. Riedl, H.H. Johannes, W. Kowalsky, J. Wang, T. Weimann, and P. Hinze, *Applied Physics*

Letters, 2005. **87**(16): p. 161103.

[25] T. Spehr, R. Pudzich, T. Fuhrmann, and J. Salbeck, *Organic Electronics*, 2003. **4**(2-3): p. 61-69.

[26] I.D.W. Samuel and G.A. Turnbull, *Chemical Reviews*, 2007. **107**(4): p. 1272-1295.

[27] O. Svelto and D.C. Hanna, *Principles of lasers*, ed. 4th. 1998: Springer.

[28] M.A. Kreger, N.J. Cherepy, J.Z. Zhang, J.C. Scott, G. Klaerner, R.D. Miller, D.W. McBranch, B. Kraabel, and S. Xu, *Physical Review B*, 2000. **61**(12): p. 8172-8179.

[29] B. Kraabel, V.I. Klimov, R. Kohlman, S. Xu, H.L. Wang, and D.W. McBranch, *Physical Review B*, 2000. **61**(12): p. 8501-8515.

[30] S.V. Frolov, Z.V. Vardeny, and K. Yoshino, *Physical Review B*, 1998. **57**(15): p. 9141-9147.

[31] G. Cerullo, S. Stagira, M. Nisoli, S. De Silvestri, G. Lanzani, G. Kranzelbinder, W. Graupner, and G. Leising, *Physical Review B*, 1998. **57**(20): p. 12806-12811.

[32] M.D. McGehee and A.J. Heeger, *Advanced Materials*, 2000. **12**(22): p. 1655-1668.

[33] H. Mattoussi, H. Murata, C.D. Merritt, Y. Iizumi, J. Kido, and Z.H. Kafafi, *Journal of Applied Physics*, 1999. **86**(5): p. 2642-2650.

[34] R. Gupta, M. Stevenson, A. Dogariu, M.D. McGehee, J.Y. Park, V. Srdanov, A.J. Heeger, and H. Wang, *Applied Physics Letters*, 1998. **73**(24): p. 3492-3494.

[35] M. Berggren, A. Dodabalapur, and R.E. Slusher, *Applied Physics Letters*, 1997. **71**(16): p. 2230-2232.

[36] A.K. Sheridan, A.R. Buckley, A.M. Fox, A. Bacher, D.D.C. Bradley, and I.D.W. Samuel, *Journal of Applied Physics*, 2002. **92**(11): p. 6367-6371.

[37] H.J. Brouwer, V.V. Krasnikov, A. Hilberer, J. Wildeman, and G. Hadziioannou, *Applied Physics Letters*, 1995. **66**(25): p. 3404-3406.

[38] T. Rabe, M. Hoping, D. Schneider, E. Becker, H.H. Johannes, W. Kowalsky, T. Weimann, J. Wang, P. Hinze, B.S. Nehls, U. Scherf, T. Farrell, and T. Riedl, *Advanced Functional Materials*, 2005. **15**(7): p. 1188-1192.

[39] D. Moses, *Applied Physics Letters*, 1992. **60**(26): p. 3215-3216.

[40] N. Tessler, G.J. Denton, and R.H. Friend, *Nature*, 1996. **382**(6593): p. 695-697.

[41] F. Hide, M.A. DiazGarcia, B.J. Schwartz, M.R. Andersson, Q.B. Pei, and A.J. Heeger, *Science*, 1996. **273**(5283): p. 1833-1836.

[42] W. Holzer, A. Penzkofer, S.H. Gong, A. Bleyer, and D.D.C. Bradley, *Advanced Materials*, 1996. **8**(12): p. 974-978.

[43] A.E. Seigman, *Lasers*. 1986: University Science Books.

[44] T. Virgili, D.G. Lidzey, M. Grell, D.D.C. Bradley, S. Stagira, M. Zavelani-Rossi, and S. De Silvestri, *Applied Physics Letters*, 2002. **80**(22): p. 4088-4090.

[45] S.E. Burns, G. Denton, N. Tessler, M.A. Stevens, F. Cacialli, and R.H. Friend, *Optical Materials*, 1998. **9**(1-4): p. 18-24.

[46] F. Demartini and G.R. Jacobovitz, *Physical Review Letters*, 1988. **60**(17): p. 1711-1714.

[47] V.G. Kozlov, V. Bulovic, P.E. Burrows, and S.R. Forrest, *Nature*, 1997. **389**(6649): p. 362-364.

[48] V.G. Kozlov, V. Bulovic, P.E. Burrows, M. Baldo, V.B. Khalfin, G. Parthasarathy, S.R. Forrest, Y. You, and M.E. Thompson, *Journal of Applied Physics*, 1998. **84**(8): p. 4096-4108.

[49] G.A. Turnbull, T.F. Krauss, W.L. Barnes, and I.D.W. Samuel, *Synthetic Metals*, 2001. **121**(1-3): p. 1757-1758.

[50] J. Stehr, J. Crewett, F. Schindler, R. Sperling, G. von Plessen, U. Lemmer, J.M. Lupton, T.A. Klar, J. Feldmann, A.W. Holleitner, M. Forster, and U. Scherf, *Advanced Materials*, 2003. **15**(20): p. 1726.

[51] S. Riechel, C. Kallinger, U. Lemmer, J. Feldmann, A. Gombert, V. Wittwer, and U. Scherf, *Applied Physics Letters*, 2000. **77**(15): p. 2310-2312.

[52] K. Yoshino, S. Tatsuhara, Y. Kawagishi, M. Ozaki, A.A. Zakhidov, and Z.V. Vardeny, *Applied Physics Letters*, 1999. **74**(18): p. 2590-2592.

[53] N. Eradat, M. Wohlgenannt, Z.V. Vardeny, A.A. Zakhidov, and R.H. Baughman, *Synthetic Metals*, 2001. **116**(1-3): p. 509-513.

[54] N. Moll, R.F. Mahrt, C. Bauer, H. Giessen, B. Schnabel, E.B. Kley, and U. Scherf, *Applied Physics Letters*, 2002. **80**(5): p. 734-736.

[55] A. Jebali, R.F. Mahrt, N. Moll, D. Erni, C. Bauer, G.L. Bona, and W. Bachtold, *Journal of Applied Physics*, 2004. **96**(6): p. 3043-3049.

[56] G.A. Turnbull, A. Carleton, G.F. Barlow, A. Tahraouhi, T.F. Krauss, K.A. Shore, and I.D.W. Samuel, *Journal of Applied Physics*, 2005. **98**(2): p. 023105.

[57] K. Forberich, A. Gombert, S. Pereira, J. Crewett, U. Lemmer, M. Diem, and K. Busch, *Journal of Applied Physics*, 2006. **100**(2): p. 023110.

[58] M. Notomi, H. Suzuki, and T. Tamamura, *Applied Physics Letters*, 2001. **78**(10): p. 1325-1327.

[59] A. Dodabalapur, M. Berggren, R.E. Slusher, Z. Bao, A. Timko, P. Schiortino, E. Laskowski, H.E. Katz, and O. Nalamasu, *Ieee Journal of Selected Topics in Quantum Electronics*, 1998. **4**(1): p. 67-74.

[60] H. Kogelnik and C.V. Shank, *Journal of Applied Physics*, 1972. **43**(5): p. 2327.

[61] G.A. Turnbull, P. Andrew, W.L. Barnes, and I.D.W. Samuel, *Physical Review B*, 2003. **67**(16): p. 165107.

[62] G.A. Turnbull, P. Andrew, M.J. Jory, W.L. Barnes, and I.D.W. Samuel, *Physical Review B*, 2001. **64**(12): p. 125122.

[63] G. Heliotis, R.D. Xia, G.A. Turnbull, P. Andrew, W.L. Barnes, I.D.W. Samuel, and D.D.C. Bradley, *Advanced Functional Materials*, 2004. **14**(1): p. 91-97.

[64] G.A. Turnbull, P. Andrew, W.L. Barnes, and I.D.W. Samuel, *Applied Physics Letters*, 2003. **82**(3): p. 313-315.

[65] R. Oron, S. Blit, N. Davidson, A.A. Friesem, Z. Bomzon, and E. Hasman, *Applied Physics Letters*, 2000. **77**(21): p. 3322-3324.

[66] C. Karnutsch, C. Pflumm, G. Heliotis, J.C. Demello, D.D.C. Bradley, J. Wang, T. Weimann, V. Haug, C. Gartner, and U. Lemmer, *Applied Physics Letters*, 2007. **90**(13): p. 131104.

[67] C. Karnutsch, C. Gyrtner, V. Haug, U. Lemmer, T. Farrell, B.S. Nehls, U. Scherf, J. Wang, T. Weimann, G. Heliotis, C. Pflumm, J.C. deMello, and D.D.C. Bradley, *Applied Physics Letters*, 2006. **89**(20): p. 201108.

[68] A.E. Vasdekis, G. Tsiminis, J.C. Ribierre, L. O'Faolain, T.F. Krauss, G.A. Turnbull, and I.D.W. Samuel, *Optics Express*, 2006. **14**(20): p. 9211-9216.

[69] H. Yamamoto, H. Kasajima, W. Yokoyama, H. Sasabe, and C. Adachi, *Applied Physics Letters*, 2005. **86**(8): p. 083502.

[70] B.K. Yap, R.D. Xia, M. Campoy-Quiles, P.N. Stavrinou, and D.D.C. Bradley, *Nature Materials*, 2008. **7**(5): p. 376-380.

[71] M. Reufer, S. Riechel, J.M. Lupton, J. Feldmann, U. Lemmer, D. Schneider, T. Benstem, T. Dobbertin, W. Kowalsky, A. Gombert, K. Forberich, V. Wittwer, and U. Scherf, *Applied Physics Letters*, 2004. **84**(17): p. 3262-3264.

[72] P. Gorm, T. Rabe, T. Riedl, and W. Kowalsky, *Applied Physics Letters*, 2007. **91**(4): p. 041113.

Chapter 3

Experimental Methods

3.1. Introduction

The two important elements in a laser are the gain medium and the feedback resonator. One of the advantages of organic semiconductors, as mentioned in **Chapter 2**, is their ease of fabrication. The theme of this chapter is to introduce experimental techniques and equipments for fabricating organic thin films and lasers. In addition, standard characterization methods will also be discussed.

Section 3.2 introduces the fabrication and characterization approaches for organic semiconductor thin films. The fabrication process starts from making organic solutions which can then be used for solid thin film deposition. The photo-physics properties of these thin films will be characterized by absorption & photoluminescence measurements, photoluminescence quantum yield (PLQY) measurement, and amplified spontaneous emission (ASE) measurements. The fabrication of DFB laser resonators will be discussed in **Section 3.3** by using two-beam interference based optical holography. The characterization of organic DFB lasers will be shown in **Section 3.4**.

3.2. Fabrication and characterization of organic thin films

3.2.1. Sample preparation

All the materials used in this thesis are purchased in powder form. To prepare thin films, firstly, the powders are dissolved in solution. Depending on the polarity of the molecular structure of the organic semiconductor, suitable organic solvents, such as chlorobenzene, chloroform and toluene, are required to dissolve these powders. The materials are weighed on a scale with precision up to 0.001 mg, followed by transferring the weighed material into a yellow vial, into which a certain amount of organic solvent is added. The whole process is performed under yellow light in a cleanroom environment to avoid UV exposure. The mixture is then stirred using a magnetic stirrer until the powder is fully dissolved. Depending on the specific molecular structure of the material, the dissolving time varies from ten minutes to twenty-four hours. For some materials, for example polyfluorene, moderate heating (~60 ^{0}C) may also be required to help properly dissolve the material. The concentration of the solution used varies between 1 mg/ml and 100 mg/ml, depending on the solubility and the molecular weight of the material. In chlorobenzene, the typical concentration for MEH-PPV is 5 mg/ml, while fluorene-based polymers requires higher concentration in the range between 20 mg/ml (PFO) and 76 mg/ml (ADS 233 YE).

Various techniques are used to prepare films out of solutions, for example spin coating, drop casting and dip coating. To have high quality thin films, spin coating is usually the best choice. Drop casting and dip coating meanwhile are preferred for fabricating relatively thick films. To make an organic semiconductor laser, the film thickness used is normally between 100 nm and 300 nm. In addition, the quality of the film is very important for achieving good waveguiding and hence low threshold

lasers. Therefore, spin coating is used in this thesis for thin film fabrication. The substrate used for depositing organic materials is either flat glass or corrugated quartz which acts as a DFB resonator. For both cases, before spin coating, the substrate is rinsed in acetone followed by isopropanol inside an ultrasonic bath. The clean substrate is held on the stage of a spin coater by vacuum and a few drops of the organic solution are deposited onto the substrate. For good film uniformity, the solution should cover the whole surface of the substrate, especially for high viscosity solutions. The spinner is set to spin at a constant speed, ranging from 800 r.p.m to 5000 r.p.m, for a certain amount of time (e.g.: 60 seconds) to form a thin solid film. The resulting film thickness is determined by several factors, including the spin speed, solution viscosity, and solvent evaporation rate. The thickness of the film can be measured by a Dektak surface profiler (Veeco).

3.2.2. Photophysical characterization

For films of new materials, the basic photophysicsal properties are first characterized to locate their absorption and emission bands. The absorption measurement is performed in a Cary Vaian 300 UV-Vis spectrometer with the sample in one arm and a reference substrate in the other to compensate for the transmission losses brought by the substrate. The preferred substrate material is quartz which gives high transparency in the UV range below 350 nm. The photoluminescence measurement is carried out in a Jobin Yvon Fluoromax2 spectrometer. The sample is excited at a single wavelength selected by a monochromated xenon lamp. The emission from the film is detected with a photomultiplier tube which is connected via a scanning monochromator. The final photoluminescence spectrum is obtained by correcting the recorded spectrum with a correction file to remove the influence of the spectral response of the instrument.

Besides absorption and emission spectra, another important photophysical property is the photoluminescence quantum yield (PLQY). It is defined as the ratio of the number of photons emitted by the material to the total number of photons absorbed. The PLQY of an organic thin film is usually lower than that of the same material in solution due to intermolecular interactions. However, high PLQY close to 100% can still be achieved in thin films as long as the chromospheres can be effectively separated [1].

To perform the PLQY measurement, the sample is placed in an integrating sphere with the inside surface coated with highly reflective coating, as shown in Figure 3.1. The advantage of using an integrating sphere is to collect all the photons emitted by the sample, independent of the angular emission pattern of the film [2-4].

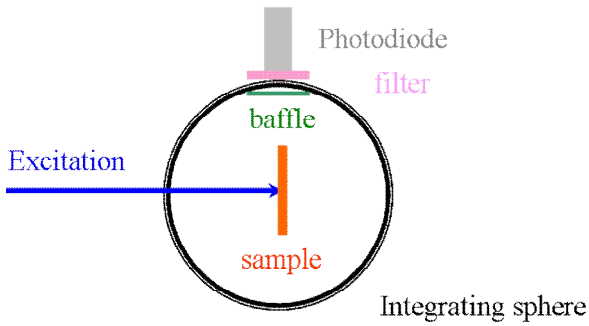

Figure 3.1. PLQY integrating sphere

As shown in Figure 3.1, the excitation laser is incident on the sample through a small hole on the wall of the integrating sphere. The emission from the sample is collected through a second port in the sphere, and passes through a filter which blocks the excitation before it is detected by a calibrated photodiode. The excitation laser used is a CW He-Cd laser whose output wavelength can be switched between 325 nm and 442 nm, with power in the range of 5 mW (325 nm) and 15 mW (442 nm). These two wavelengths are capable of exciting most of the organic materials. The excitation power used in the PLQY measurement can be

measured with the removal of the filter. When the excitation is incident on the sample, a fraction is absorbed. This is determined by measuring the normal reflectance and transmission of the sample. Some of the excitation which is not absorbed on the first pass can be absorbed following diffuse reflections from the walls of the integrating sphere. This can be measured by placing the sample inside the integrating sphere but not directly in the beam path of the excitation. The fluorescence resulting from this fraction of the incident excitation must be subtracted in the PLQY calculation. If the spectral response of the integrating sphere is neglected, the PLQY is given by[5]:

$$x = \frac{X_{sample} - (R+T)X_{sphere}}{(1-R-T)X_{laser}} \qquad \textbf{3-1}$$

In equation 3-1, T and R are the normal transmittance and reflectance of the sample at the excitation wavelength. The measured excitation power is X_{laser}. X_{sample} represents the fluorescence measured with the sample in path of the excitation beam. The fraction of the fluorescence arising form the subsequent absorption is deducted in the denominator in the second term with X_{sphere} measured when the sample is not directly excited.

In reality, the spectral response of the integrating sphere is very important and needs to be taken into account. To do the calibration, the spectrum of a tungsten lamp $S_{lamp}(\lambda)$ is first measured by a CCD spectrograph outside the integrating sphere. When the lamp is shone in the integrating sphere, the spectrum measured through the exit port (where the photodiode is normally connected) is modified by the response of the integrating sphere and becomes $S_{sphere}(\lambda)$. When the sample is placed inside the integrating sphere, the correction factor for the spectral response is:

$$y = \int \frac{S_{sphere}(\lambda)L(\lambda)G(\lambda)F(\lambda)}{S_{lamp}(\lambda)} d\lambda \times [\frac{S_{sphere}(\lambda_{exc})G(\lambda_{exc})}{S_{lamp}(\lambda_{exc})} \int L(\lambda)d\lambda]^{-1} \qquad \textbf{3-2}$$

where $L(\lambda)$ is the emission spectrum of the material measured by Fluoromax 2; $G(\lambda)$ is the quantum efficiency of the photodiode, calibrated by the National Physical Laboratory (NPL)*; $F(\lambda)$ is the filter transmission used in front of the photodiode and λ_{exc} is the excitation laser wavelength. The final absolute PLQY of the material is given by:

$$PLQY = \frac{x}{y} \qquad \textbf{3-3}$$

3.2.3. Gain and loss measurement

Apart from the basic photo-physical characteristics, a good laser gain medium should posses other properties, such as high gain and low loss, to achieve lasing at low pumping energy. Amplified Spontaneous Emission (ASE) measurement is a useful technique to evaluate the stimulated emission of organic semiconductors, through which gain and loss coefficients can be deduced.

3.2.3.1. Excitation source: Optical Parametric Oscillator

In this thesis, if not specified otherwise, the pump source used for ASE and lasing studies is an Optical Parametric Oscillator (OPO) (Panther OPO, Continuum). When excited by the third harmonic beam from a Q-switched Nd:YAG laser at 355 nm, it is capable of generating 4 ns output pulse at 20 Hz in the wavelength range between 410 nm to 2550 nm, with maximum energy up to 15 mJ. UV pulses (205 nm-420 nm) can also be generated by frequency doubling the signal or idler waves from the OPO.

In principle, an OPO consists of a nonlinear crystal and a resonator. As described in Figure 3.2, in the crystal, the pump photon (w_p) splits into a pair of photons called

signal (w_s) and idler (w_i) of different frequencies. The optical components (e.g.: cavity mirrors and lenses) of the resonator determines whether the signal or/and the idler photons will be resonated to achieve efficient conversion.

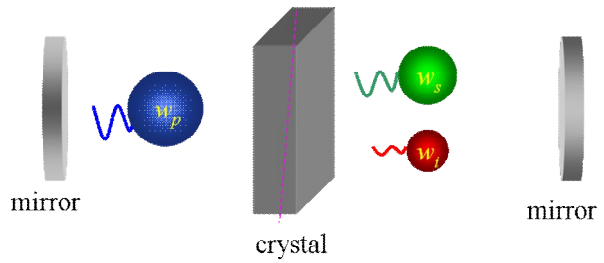

Figure 3.2. OPO cavity: the nonlinear crystal in between two mirrors

The optical parametric process must satisfy both energy and momentum conservation rules:

$$w_p = w_s + w_i$$
$$\vec{k}_p = \vec{k}_s + \vec{k}_i \qquad \textbf{3-4}$$

w_p, w_s and w_i are the frequencies of the pump, single and idler photons; and $\vec{k}$ is the corresponding wavevector. The momentum conservation is not naturally preserved when the energy conservation is satisfied, since the refractive index and hence the velocity in the nonlinear crystal is frequency and polarization dependent. For the Panther OPO used in this thesis, type II phase matching is used in the BBO nonlinear crystal. This means that the extraordinary polarized pump photons interact with ordinary signal and extraordinary idler photons. The parametric conversion efficiency is enhanced by doubling the interaction length between the pump beam and the generated beams through the use of high reflectivity cavity mirrors for the pump beam. The cavity is designed to be singly-resonant for the idler wave with the signal emitted after a single pass through the crystal.

Figure 3.3 shows the experimental setup used for characterizing organic semiconductor films and lasers. A pair of polarizers and a series of ND filters are used in the OPO beam path to vary the excitation energy. A cylindrical lens (for ASE measurement) or a spherical lens (for laser measurement) is used to focus the pump beam onto the sample. The sample is stored inside a vacuum chamber at 10^{-4} mbar during experiments to slow down oxidation and photodegradation. The vacuum chamber is placed on a translation stage which can be moved along the pump beam to select suitable excitation spot sizes. The emission from the films or lasers is collected with a fibre-coupled CCD spectrograph (Jobin-Yvon Triax 180) for spectral measurement.

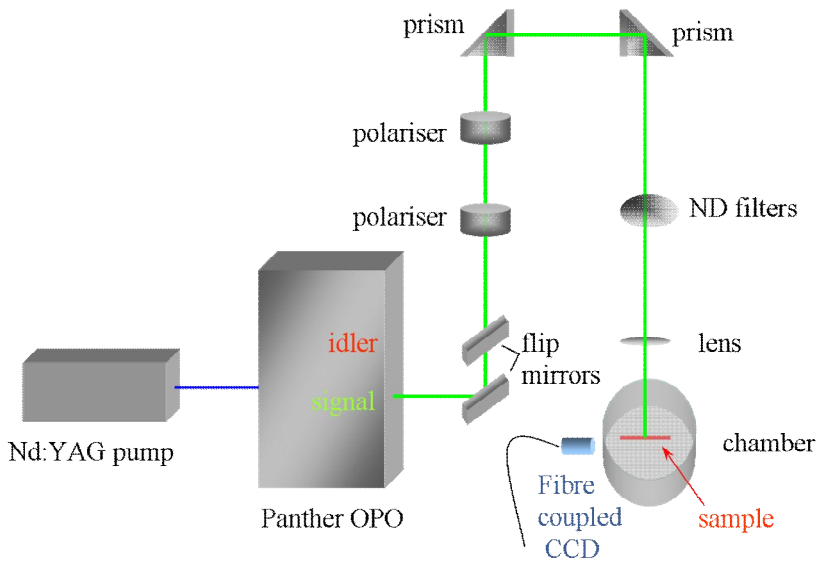

Figure 3.3. Experimental setup for thin film and laser characterization

3.2.3.2. ASE measurements

Variable stripe measurement of amplified spontaneous emission is a widely applied method to measure the gain in organic semiconductors [6-8]. It exploits the amplification of the spontaneous emission from an organic thin film in a slab waveguide. The pump beam is focused into a stripe whose long axis is perpendicular to the edge of the thin film, as described in Figure 3.4.

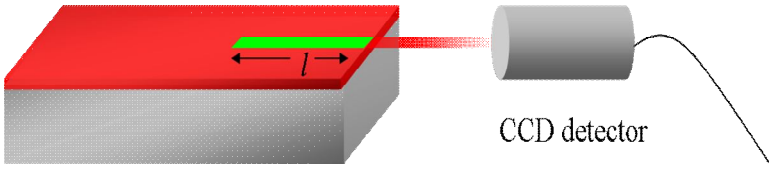

Figure 3.4. ASE measurement

As the spontaneous emission from the organic semiconductor is guided towards the edge in the waveguide formed by the organic layer and the silica substrate, it serves as a probe signal which is amplified by the excitons in the pumped region. When the pump energy exceeds a certain threshold level, the emission spectrum narrows into a peak with a FWHM ranging from 5 nm to 15 nm, depending on the material used. The peak of the output spectrum indicates the wavelength of maximum gain. This information can be used as a guideline for laser design. Ideally, the laser should lase at a wavelength close to the maximum gain in order to have low lasing threshold.

ASE is very similar to lasing, except that it has no feedback resonator. Hence, the amplification experienced by the waveguided emission results from a single pass gain which can be deduced from[9]:

$$I_{out} = \frac{A(\lambda)I_p}{g(\lambda)}(e^{g(\lambda)l} - 1) \qquad \textbf{3-5}$$

$A(\lambda)$ is a constant related to the spontaneous emission cross section of the material, $g(\lambda)$ is the optical gain, I_p is the pump intensity and l is the length of the stripe. By measuring the output emission as a function of the stripe length, the optical gain coefficient $g(\lambda)$ can be extracted from the fitting curve based on equation 3-5 with $g(\lambda)$ and $A(\lambda)$ as the fitting parameters.

If the pumping stripe is gradually moved away from the edge of the film, while its length is kept constant, the change in the emission from the edge carries information about the propagating loss in the unpumped region. Based on equation 3-6, the loss coefficient can be calculated from an exponential fitting curve of the I_{out} vs I_p plot.

$$I_{out} = I_p e^{-\alpha x} \qquad \textbf{3-6}$$

where x is the length of the unpumped region; α is the loss coefficient.

3.3. Laser cavity fabrication

In this thesis, a distributed feedback resonator (DFB) has been chosen as the laser cavity for most of the work on solid state organic semiconductor lasers because of its low lasing threshold and simple fabrication. Two different approaches are used for fabricating periodic resonators directly on silica substrates, namely e-Beam lithography and holography. Compared to holography, e-beam lithography allows design of high quality gratings with complex geometries, such as circular gratings. However, the overall grating area is normally small and is typically limited to 100 μm by 100 μm with the e-beam system in the department. Larger area patterns from a few millimetres to centimetres are possible only with an extremely high precision stepping motor to stitch together the fields. The whole fabrication is very time consuming and expensive, especially for large area resonators. Holography, on the

other hand, has the advantage of patterning large area gratings at low cost. The size of the resonator is dependent on the size of the laser beam. It is an interference based technique and excludes the complicated equipment required in e-beam lithography, maintaining the simple fabrication and low cost characteristics of organic semiconductors. Holography however offers limited control on the duty cycle and grating geometries. The DFB resonators, in this thesis, are all fabricated by holography to fulfil the requirement for the LED pumped organic semiconductor laser, which will be discussed in details in **Chapter 4**.

The basis of the holographic grating fabrication is two-beam interference, as illustrated in Figure 3.5. A thin film of photoresist is exposed to two mutually coherent laser beams of wavelength λ separated by an angle of 2θ. The resulting in-plane wavevectors of these two beams are counter-propagating and form a standing wave interference pattern with period Λ given by:

$$\Lambda = \frac{\lambda}{2\sin\theta} \qquad \textbf{3-7}$$

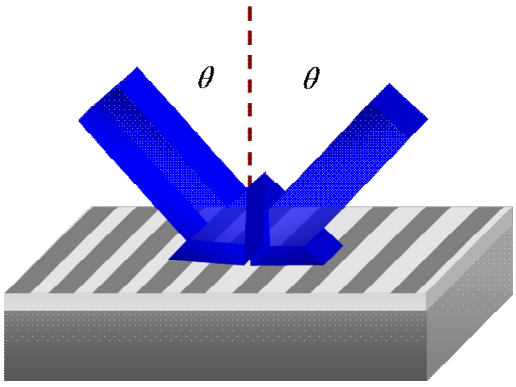

Figure 3.5. Holography made by two beam interference

Figure 3.6 outlines the general steps for making a DFB resonator on a silica substrate. First, a thin layer of UV sensitive photoresist is spin coated onto the substrate, followed by a pre-bake to evaporate any remaining solvent. Two beam interference method was used to define the periodic pattern in the photoresist as

described in Figure 3.5. Depending on the properties of the photoresist, a post-bake process could be required after exposure. A specific developer is then used to wash away the unwanted parts of the photoresist. At this stage, the periodic structures are formed in the photoresist and ready to be etched into the substrate. In the etching process, with the patterned photoresist as a mask, Reactive Ion Etching (RIE) is used to transfer the periodic structure into the substrate. To finalize the fabrication process, the remaining photoresist should be washed off in suitable solvents.

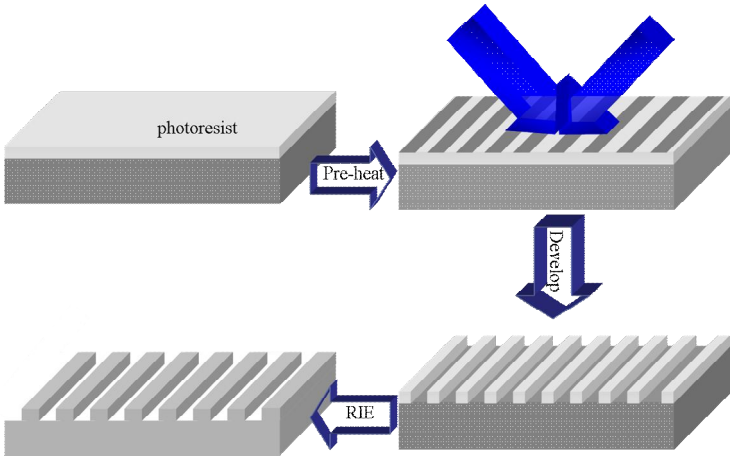

Figure 3.6. Steps for making a DFB resonator on silica substrate

The fabrication apparatus is shown in Figure 3.7. The laser source is the CW He-Cd laser with 325 nm output. The diameter of the laser beam is expanded to 16 mm with the use of a beam expander and a collimating lens to achieve a uniform intensity of 0.044 mW/cm^2. A silica prism was used to reflect the laser beam into the heart of the interferometer, which comprises a beam splitter, two steering prisms and two rotatable mirrors. Refractive index match oil was used in between the prisms to seal the air gap to reduce reflection loss at each interface. The beam splitter separates the incident laser beam into the two interferometer arms with equal intensity. In each arm, the laser beam experiences two reflections before it gets out. The same numbers of reflections can ensure the output intensities in both arms are identical, which can maximize the contrast in the

interference pattern and thus the grating depth. The two output beams are reflected to the photoresist-coated substrate by a pair of highly reflective dichroic mirrors. The period of the grating can be varied by changing the rotating angle α of the mirrors:

$$\Lambda = \frac{\lambda}{2\sin(\pi/2 - 2\alpha)} \qquad \textbf{3-8}$$

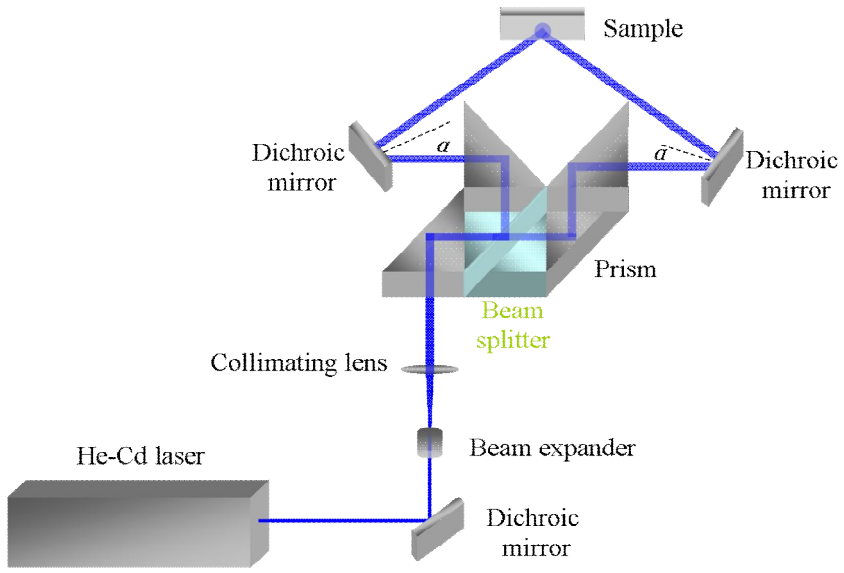

Figure 3.7. Holography setup

The photoresist used is a positive photoresist SR1805 (Shipley), which is widely used in the fabrication of submicron structures [10-11]. The photoresist solution was diluted 1:1 with EC solvent to reduce the film thickness, which could benefit the etching process for obtaining deep gratings in the substrate. The solution was spin coated onto the silica substrate at 3250 r.p.m. to form a 170 nm thick film. The exposure dose, which is related to the exposure time, is critical and needs to be optimized to fabricate high quality gratings. Therefore, a range of exposure durations were investigated in order to optimize the grating depth and uniformity. The exposed samples were then developed in MF 319 for 2 seconds, followed by a rinse in deionised water. For positive photoresists, the exposed fraction of the

film is removed during developing. Figure 3.8 illustrates the two AFM scans of an optimized and a un-optimized gratings.

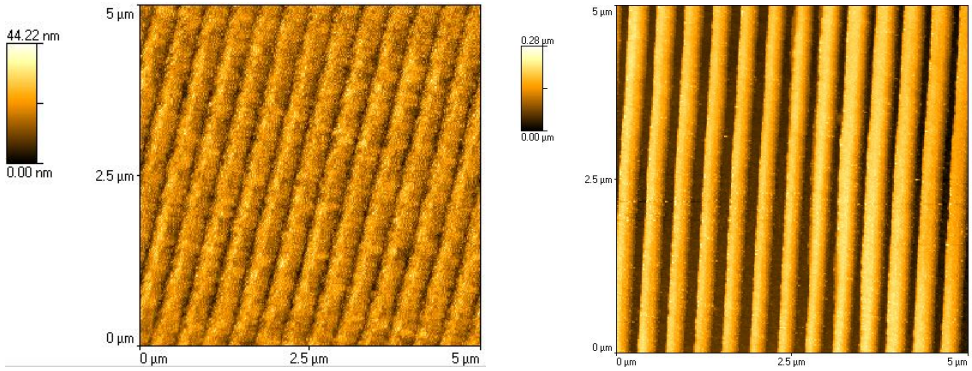

Figure 3.8. AFM image of (left) a un-optimized and (right) an optimized grating with period of 325 nm

The exposure time for the un-optimized structure in Figure 3.8 was 9 minutes, while it was 15 minutes for the optimized structure. It is obvious that in the un-optimized sample, the grating grooves are not as uniform as expected. Moreover, with depth in the range from 12 nm to 20 nm, the gratings are very shallow. Once optimized, the grating depth in the right scan can increase to 150 nm with relatively good uniformity. The grating depth is close to the film thickness of the photoresist, indicating that the exposed fraction was completely removed during developing. This is very important in terms of transferring the grating into the substrate. During RIE, the substrate is etched as the patterned photoresist is etched away. The final depth of the grating inside the silica substrate depends on the etching rate of the photoresist and the silica. If the grating depth in the photoresist is very shallow, the worst scenario is that the gratings in the photoresist could be etched away before the ions can reach the silica substrate, leaving no grating structure in the substrate. Even if the ions have the chance to react with the substrate, the grating depth in the substrate will be much smaller than that in the photoresist. Therefore, deeper gratings are preferred in the photoresist.

To perform RIE, the sample was placed inside a chamber of high vacuum which is gradually filled with appropriate gas, CHF_3 in the case for silica substrate. The applied high RF voltage leads to the ionization of the gas. The etching happens when the substrate reacts with the fluorine gas to form a gas form product. Figure 3.9 gives the AFM image of the etched substrate, based on the optimized gratings in Figure 3.8.

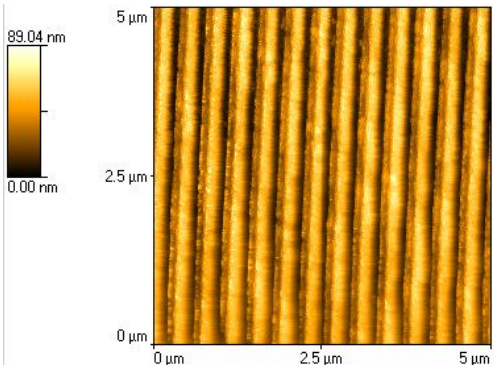

Figure 3.9. AFM scan of the etched substrate

After a fifteen-minute etch, the grating still preserved a similar shape as the photoresist gratings. However, the grating depth was reduced by a factor of 3 to 50 nm. The loss of depth could be due to the different etching rates of SR1805 and silica discussed above.

3.4. Organic semiconductor laser characterization

Following the ASE characterization of the gain medium and the fabrication of the resonator substrate, an organic semiconductor DFB laser can be fabricated by spin coating the gain medium onto the corrugated substrate. In this thesis, all the DFB lasers are surface emitting second order lasers. In the resonator, the second order diffraction of the gratings gives in-plane feedback and the first order diffraction couples the emission out at normal incidence to the surface of the laser.

Several important features of the laser need to be characterized, such as lasing threshold and wavelength, to optimize the performance. The experimental setup used is the same as the one shown in Figure 3.3. To avoid degradation, the laser was placed inside a vacuum chamber. The pump energy was varied with the use of different neutral density filters. Figure 3.10 shows a schematic view of the setup.

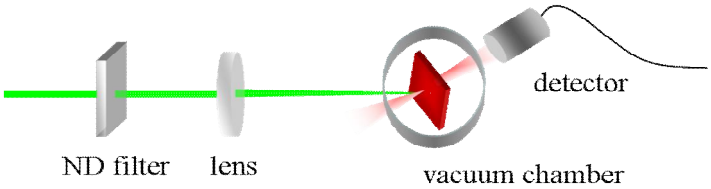

Figure 3.10. Organic semiconductor laser characterization

The CCD fibre-coupled detector is placed at normal incidence to the surface of the film to collect the emission from the DFB laser. The organic laser is tilted at an angle to the pump beam to prevent detector saturation from the pump beam. As the pump energy increases, a kink can be observed in the input vs output graph, accompanied by a sudden change of the slope, indicating the onset of lasing (Figure 3.11(a)). Additionally, the FWHM of the corresponding emission spectrum narrows significantly to approximately 1 nm, as indicated in Figure 3.11(b).

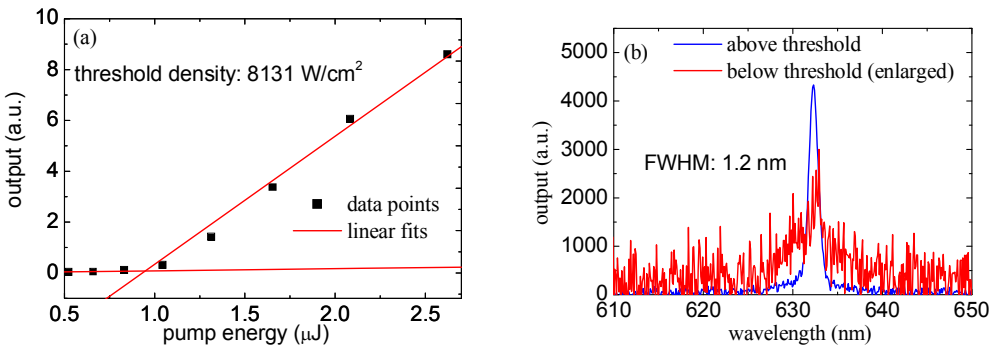

Figure 3.11. (a) Input vs output graph: (black squares) experimental data and (red lines) two linear fits to data points above and below threshold; (b) Emission spectrum of MEH-PPV laser

3.5. Angle resolved photoluminescence

Besides the lasing threshold and emission spectrum, an angle dependent photoluminescence measurement is a very useful technique to reveal the information about the photonic dispersion curves of a DFB resonator, which is also helpful in identifying the lasing peaks of the transverse waveguide modes [12-13]. Figure 3.12 presents the principles of the angle dependent PL measurement.

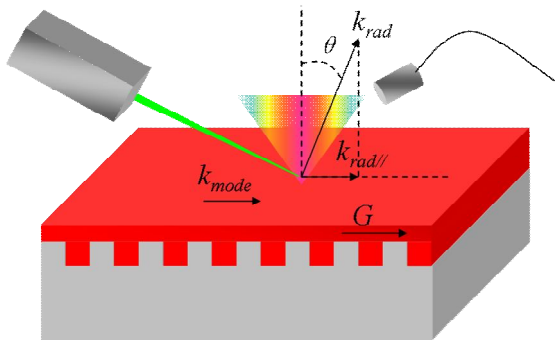

Figure 3.12. Angle dependent measurement setup

As described in **Chapter 2**, light emission from the organic layer is coupled into different waveguide modes with wavevectors k_{mode} inside the thin film. These guided modes can be scattered out of the waveguide by the diffraction gratings. The emission angle of the radiated wave is determined by the conservation of in-plane wavevectors in the diffraction process:

$$k_{rad//} = k_{\text{mode}} + mG$$

$$\frac{2\pi}{\lambda}\sin\theta = \frac{2\pi}{\lambda}n_{eff} + m\cdot\frac{2\pi}{\Lambda} \qquad \textbf{3-9}$$

Where λ is the wavelength of the emission from the organic layer; n_{eff} is the effective refractive index of the waveguide mode; m is the diffraction order of the grating with period Λ; G is the wavevector of the Bragg gratings. Equation 3-9

illustrates the relationship between the emission wavelength and the output coupling angle θ. The photonic dispersion curve of the structure can be obtained by plotting a graph of λ (inversely proportional to the energy) vs θ (proportional to the in-plane wavevector).

To perform the angle dependent measurement, the organic laser is excited by a CW laser to give spontaneous emission. The output spectrum at each angle is recorded by the fibre-coupled CCD used in the lasing measurements, with an angular step of 1 degree. To distinguish the TE and TM modes inside the waveguide, a linear polariser can be placed in front of the detector. Figure 3.13 plots an typical example of the result from the angle dependent PL measurement performed on a 1D DFB resonator.

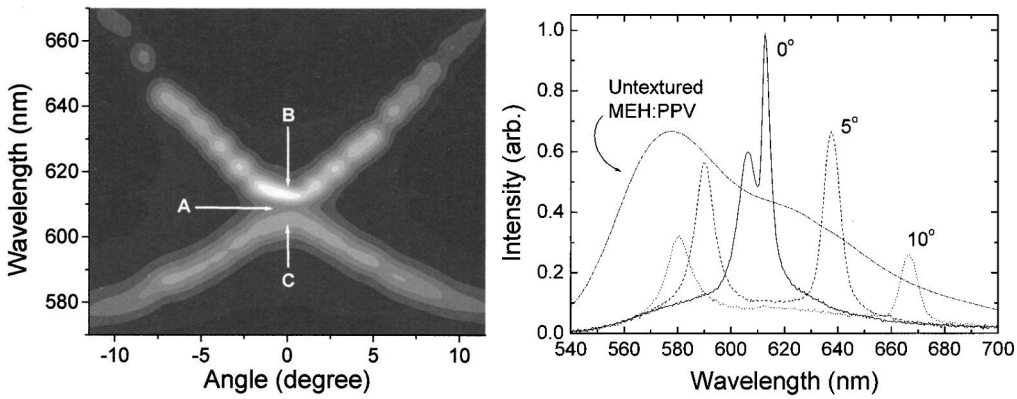

Figure 3.13. Angle dependent measurement on 1D MEH-PPV DFB laser

([14] Copyright 2010 by The American Physical Society)

As indicated in the left density plot, a stop band can be located at zero degree at A. Proportional to the slope of the dispersion curve, the group velocity at the stop band is zero as expected. The output spectra at different collection angles are shown on the right. As the angle is detuned from normal incidence, two emission wavelengths, nearly symmetric to the peak obtained at zero degree, can be detected, corresponding to the upper and lower branches of the dispersion curve.

3.6. Reference

[1] W.Y. Lai, R.D. Xia, Q.Y. He, P.A. Levermore, W. Huang, and D.D.C. Bradley, *Advanced Materials*, 2009. **21**(3): p. 355.

[2] J.C. deMello, H.F. Wittmann, and R.H. Friend, *Advanced Materials*, 1997. **9**(3): p. 230.

[3] H. Mattoussi, H. Murata, C.D. Merritt, Y. Iizumi, J. Kido, and Z.H. Kafafi, *Journal of Applied Physics*, 1999. **86**(5): p. 2642.

[4] N.C. Greenham, S.E. Burns, I.D.W. Samuel, R.H. Friend, S.C. Moratti, and A.B. Holmes, *Molecular Crystals and Liquid Crystals Science and Technology Section a-Molecular Crystals and Liquid Crystals*, 1996. **283**: p. 51.

[5] N.C. Greenham, I.D.W. Samuel, G.R. Hayes, R.T. Phillips, Y.A.R.R. Kessener, S.C. Moratti, A.B. Holmes, and R.H. Friend, *Chemical Physics Letters*, 1995. **241**(1-2): p. 89.

[6] N. de la Rosa-Fox, *Optical Materials*, 1999. **12**(2-3): p. 267.

[7] M.D. McGehee, R. Gupta, S. Veenstra, E.K. Miller, M.A. Diaz-Garcia, and A.J. Heeger, *Physical Review B*, 1998. **58**(11): p. 7035.

[8] G. Jordan, M. Flammich, M. Ruther, T. Kobayashi, W.J. Blau, Y. Suzuki, and T. Kaino, *Applied Physics Letters*, 2006. **88**(16).

[9] K.L. Shaklee and R.F. Leheny, *Applied Physics Letters*, 1971. **18**(11): p. 475.

[10] V. Berger, O. GauthierLafaye, and E. Costard, *Electronics Letters*, 1997. **33**(5): p. 425.

[11] N. Nagy, J. Volk, A. Hamori, and I. Barsony, *Physica Status Solidi a-Applications and Materials Science*, 2005. **202**(8): p. 1639.

[12]G.A. Turnbull, P. Andrew, W.L. Barnes, and I.D.W. Samuel, *Physical Review B*, 2003. **67**(16): p. 165107.

[13] D. Schneider, T. Rabe, T. Riedl, T. Dobbertin, M. Kroger, E. Becker, H.H. Johannes, W. Kowalsky, T. Weimann, J. Wang, and P. Hinze, *Journal of Applied Physics*, 2005. **98**(4).

[14] G.A. Turnbull, P. Andrew, M.J. Jory, W.L. Barnes, and I.D.W. Samuel, *Physical Review B*, 2001. **64**(12): p. 125122.

Chapter 4

Hybrid Optoelectronics: A Polymer Laser Pumped by an InGaN LED

4.1. Introduction

As mentioned in **Chapter 2**, in the past decades, great effort has been made on reducing the cost and size of the pumping sources for organic lasers, from a giant regenerative amplifier [1] to microchip lasers with size of a cookie box [2-4] and to small diode lasers [5-6]. However, the pump laser remains an expensive, delicate and often complex component in the organic laser system, potentially limiting their use in applications. Electrically excited organic lasers could change the situation. However, the low carrier mobilities of organic semiconductors have meant that direct electrical excitation has not been possible to date [7-8], although some useful progress has been made [9-11]. On the other hand, the rapid development of III-IV LEDs provides alternative solution for making compact organic laser systems with low cost. Driven by the lighting industry, these LEDs have extended their emission into the blue and UV range [12-14] with attractive high power and with efficiency exceeding 10%. An LED pumped organic laser would dramatically reduce the cost by two orders of magnitude from hundreds of pounds to a few pounds. It effectively bypasses the challenges of an electrically pumped laser and preserves all the benefits of a direct electrically pumped laser, such as direct electrical control, low cost and being very compact.

In this chapter, the possibility of LED pumped lasers is explored. To pump an organic semiconductor laser, the LED must be pulsed, since it is difficult to achieve CW organic lasers due to triplet/polaron absorption losses. Additionally, pulsing the LEDs can increase the peak power of the LED emission significantly, in comparison to DC driven LEDs. In **Section 4.2**, the potential of pulsing and focussing the LEDs is investigated. In order to use the LED output intensity effectively, different pumping geometries are attempted in **Section 4.3** in terms of LED pumped lasers. In **Section 4.4**, with the aim of lowering the organic laser thresholds to match the peak power intensity of the LEDs, a number of polymers or blends are characterized. Finally, by combining the high power LED and low threshold polymer laser, the world's first LED pumped polymer laser is successfully demonstrated in **Section 4.5**. The achievement has been highlighted in Nature after being published in Applied Physics Letters.

4.2. Characterization of GaN LEDs

The rapid development of GaN devices improves the energies of royal blue LEDs, making them potential useful excitation sources for organic lasers. The LEDs chosen for pumping organic lasers were purchased from Lumiled Ltd, which offers robust performance, exceptional long lifetimes and, most importantly, high output power and efficiency under DC driving. Table 4.I lists five high power blue LEDs.

Part number	typical power (mW @1A)	wavelength (nm)	emission angle (deg.)	type
LXHL-PR09	450	455	120	Emitter
LXHL-PR02	700	455	140	Emitter
LXHL-LR3C	450	455	120	Star Hex
LXHL-LR5C	700	455	140	Star Hex
LXK2-PR14-Q00	475	455	150	Emitter

Table 4.I. List of Lumiled LEDs

The powers shown in the table are measured under a DC drive current of 1 A. The output power from PR09, PR02 are identical to LR5C and LR3C with the difference lying in the packing. PR09 and PR02 are packed as emitters, while LR5C and LR3C are Star Hex, as shown in Figure 4.1. Compared to the first four LEDs (LUXEON III), LXK2-PR14-Q00 is from a different series (LUXEON K2) with advanced thermal management, leading to a higher DC power.

Figure 4.1. Image of emitter (left) and Star Hex (right)

4.2.1. Focusing ability

As indicated in Table 4.I, the incoherent emission of these LEDs is highly divergent with angles between 120^0 and 150^0. To make these LEDs suitable excitation sources for organic lasers, the emission should be focused into a small spot of hundreds of micrometers in diameter to improve the power intensity.

A microscope condenser, used to concentrate the light from the illumination source onto an object, is a major component in transmitted light compound microscopes. The basic element of a condenser is a lens with short focal length and high numerical aperture (NA). Hence it is suitable for focusing the highly divergent emission of the LEDs. Prior to placing the condenser in front of the LED, a specifically designed plastic transparent lens (L2 Optics Ltd.), shown in Figure 4.2, was mounted directly onto the LED. This lens can reduce the emission angle down to 5 degrees with a beam diameter of 30 mm. With the use of the plastic lens and the condenser, the LED emission can be focused into a spot approximately the same size as the light emitting chip of the LED (1.5 mm by 1.5 mm). However, the power intensity is lower than that at the surface of the LED.

Figure 4.2. Image of the transparent lens mounted on the LED

Alternatively, to cope with the highly divergent emission, two lenses of 50 mm in diameter were placed in series in front of the LED, as indicated in Figure 4.3. Separated by 44 mm apart, the two lenses have focal lengths of 63 mm and 55 mm respectively. Lens 1 was in contact with the plastic lens mounted on the LED in order to collect as much LED emission as possible. Lens 2 was added to enhance the focusing strength to the beam passing through Lens 1. The combination of these two lenses can concentrate most of the output energy into a spot of 5.1 mm in diameter for LR3C and 7.5 mm for LR5C. The smaller spot size obtained for LR3C arises from the smaller size of the light emitting chip in the LED.

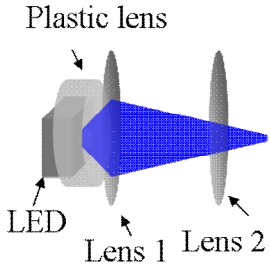

Figure 4.3. Two-lens setup

To further reduce the spot size, three additonal lenses can be introduced after lens 2, as indicated in Figure 4.4. The diameters and focal lengths of the extra three lenses are listed in Table 4.II. Lens 3 was used to collimate the beam from the previous two-lens system, which was then refocused by lens 4 and lens 5. With the help of these three lenses, the spot sizes were reduced to 3.8 mm for LR3C and 5.1 mm for LR5C.

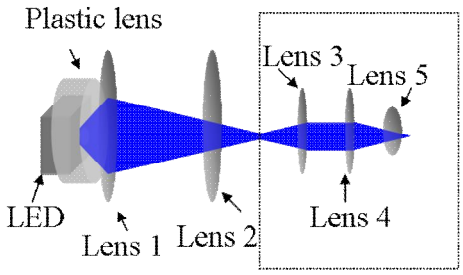

Figure 4.4. Five-lens setup

	Lens 3	Lens 4	Lens 5
f (mm)	50	32	20
Diameter (mm)	25	25	20
Distance (from previous lens)	53	45	11

Table 4.II. Parameters of lens 3, lens 4 and lens 5

Despite the small spot sizes achieved after lens 5, when driven by a 10 ns current pulse at 2 A, the peak power densities measured at the focus were 106 mW/cm^2 and 227 mW/cm^2 for LR5C and LR3C respectively, nearly an order of magnitude lower than the power densities on the surface of the LED.

The results from both the microscope condenser and the lens system suggest that conventional imaging technique cannot concentrate the highly divergent emission from the LEDs effectively. Instead of focusing, an alternative approach is to attach the light emitting chip directly onto the organic gain layer to ensure most of the LED output intensity can be harvested. To get access to the LED chip, the encapsulating epoxy dome of the LED was removed by immersing the LED in chlorobenzene for 60 minutes, followed by rinsed with acetone and IPA.

4.2.2. LEDs under pulsed operation

The Lumiled LEDs offer high output power under DC driving, with a maximum power quoted in the specification sheets of 700 mW, corresponding to 20 W/cm^2. However, this power intensity is much lower than the normal threshold densities of organic lasers. Commonly, organic semiconductor lasers have threshold of tens

of kW/cm^2, although lasers with low thresholds close to tens of W/cm^2 have been demonstrated [15-16]. On the other hand, there may be an advantage in driving the LEDs in pulsed mode where the higher peak power than a DC driven LED would bring the LED power intensity close to the required threshold densities of organic semiconductor lasers. Conventionally, organic semiconductor lasers are pulsed at relatively low repetition rates between 10 Hz and 10 kHz with excitation pulse widths in the regime between 100s of fs to 10s of ns to prevent triplet population dissipating between pump pulses. Indeed, continuous-wave (CW) pumping has not yet been achieved in organic lasers due to the accumulation of the triplet excitons through intersystem crossing, leading to the competition between stimulated emission and excited-state absorption loss [17].

To make the LEDs suitable pump sources for organic semiconductor lasers, the electronics used to pulse these LEDs should give short current pulses between hundreds of picoseconds and tens of nanoseconds with high current/voltage amplitude and low or variable repetition rate. In this section, the compatibility of two possible laser diode drivers (Direct Energy Inc.) for pulsing the Luimiled LEDs is tested. The operating parameters of these two drivers are shown in Table 4.III.

PCO-7100 model	40-4	120-15
current (A)	4-40	5-120
pulse width (ns)	4	15
maximum frequency	50 KHz	2 KHz

Table 4.III. Driver parameters

The first driver tested is PCO-7810-40-4, which is able to give 4 ns current pulse with maximum current of 40 A at variable repetition rate up to 50 kHz as indicated in Table 4.III. LR3C and LR5C were tested as prototypes and connected to the driver by wires. Figure 4.5 shows the temporal profiles of the current pulse measured through the integrated current monitor.

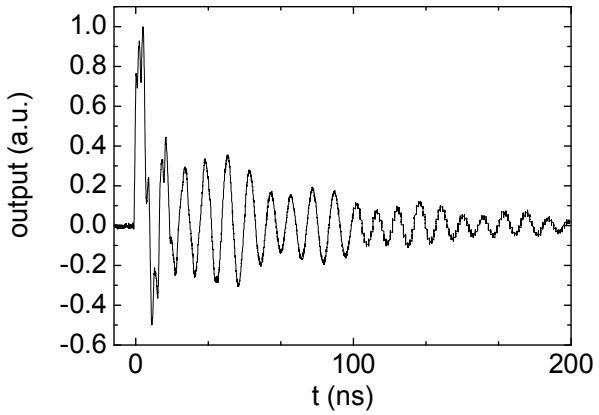

Figure 4.5. Current pulses of PCO-7810-40-4

From the oscilloscope trace, the FWHM of the initial current pulse is 5 ns with a 1 ns rising edge. However, it has a strong oscillation in the tail, extending to 300 ns, which could arise from the built in electronics used for discharging the drive current in a short time scale of 4 ns. The ringing of the drive current pulse has a strong impact on the temporal profile of the LED (LR5C) emission, as shown in Figure 4.6.

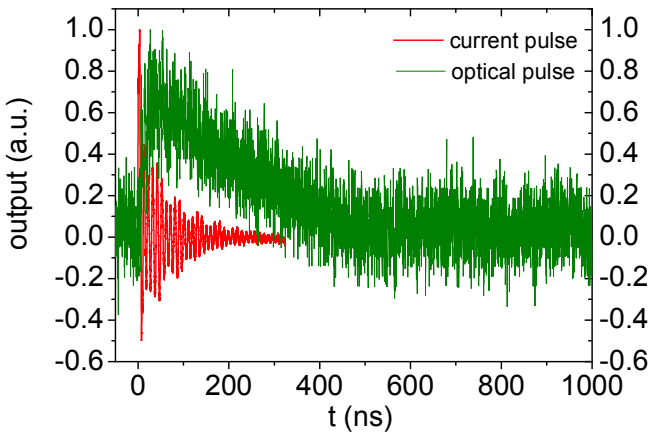

Figure 4.6. (Red) Current pulse profile measured at 40 A; (Green) Optical pulse profile measured by a high-speed photodiode (Standa 11HSP-V2)

The FWHM of the LED emission is measured to be 160 ns, 40 times longer than the current pulse and overlapping well with the ringing of the current pulse. As we are limited by the resolution of the detecting system, it is not possible to resolve

how the oscillation in the current pulse affects the LED output pulse. Besides the long tail of the drive current, another possible factor contributing to the long optical pulse could be the mismatched impedance between the LED and the driver.

Figure 4.7 shows the dependence of the FWHM of the measured optical pulse and the corresponding peak power on the drive current for LR3C and LR5C. The values of the power in the plots are uncalibrated numbers measured with the LEDs placed at a fixed distance away from the pyroelectric energy detector (Molectron) to minimize pick-up of the electrical spikes. Such measurement is sufficient at this stage to reveal the impact of the drive current on the power and the LED pulse width.

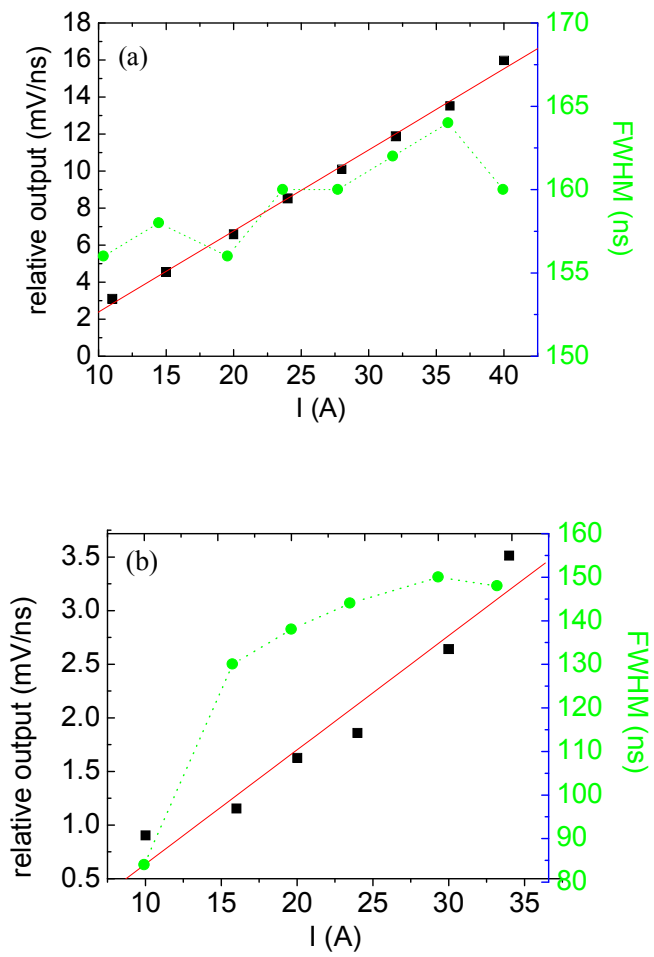

Figure 4.7. The dependence of the drive current on the output power and the optical pulse FWHM for LR3C (a) and LR5C (b)

The average pulse widths are 160 ns and 140 ns respectively for LR3C and LR5C with slight increase at high drive currents. The variation in pulse width is larger for LR5C (~60 ns) than for LR3C (~10 ns), which may be caused by the different electronic designs and packaging in these two LEDs. The output power increased linearly with the increase of the drive current for both LEDs, indicated by the red linear fit line. To evaluate the maximum power intensity, an absolute energy measurement were performed at the maximum drive current for both LEDs. By assuming that the LED chip sizes are 2.1 mm by 2.1 mm for LR5C and 1.5 mm by 1.5 mm for LR3C, the absolute maximum power densities are 50 W/cm^2 and 52 W/cm^2 respectively, corresponding to 330 nJ and 120 nJ per pulse. The fact that the LEDs are not saturating or breaking down at the highest drive current of 40 A suggests that it may be possible to extract more power from the LEDs at even higher drive currents.

In comparison to continuous-wave driving, the output power densities of the pulsed LEDs were successfully increased by a factor of 2.5. However, the power densities are still well below the required lasing threshold densities. Based on the linear fitting in Figure 4.7, to reach a lasing threshold of say 1 kW/cm^2, at least 800 A peak current would need to be driven through the LED. It is highly possible that the LEDs would break down from the enormous amount of heat produced by such high drive current. To relieve the pressure on the requirements of the drive current, the optical pulse width of the LED could be manipulated by choosing a driver providing shorter and smoother current pulses.

To improve the LED performance, another diode laser driver PCO-7100-120-15 (Energy Direct Inc.) in Table 4.III was tested. Unlike the integrated PCO7810-40-4 driver which has a built-in unit for current and repetition rate control, this module needs an external high voltage DC source (maximum voltage of 495 V) to control the current amplitude and an external function generator to vary the repetition rate. With this driver, the maximum current can be increased to 120 A in 15 ns pulses. Repetition rates at as high as 2 kHz are available. Figure 4.8 presents a typical output current pulse.

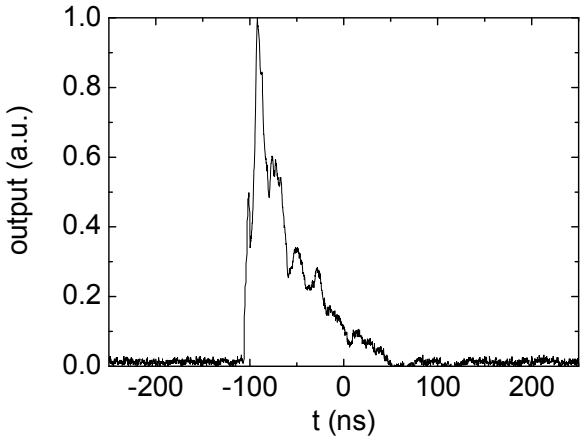

Figure 4.8. Current pulse of PCO 7100-120-15

The measured current pulse width is 16 ns with a 2.5 ns rise time, close to the 15 ns FWHM quoted in the manual. Compared to the current pulse from PCO-7810-40-4, the drive current pulse is 4 times longer, but no obvious oscillation in the tail. Figure 4.9 shows the optical pulse from the LED when driven at a peak current of 40 A. The measurement shows a FWHM of 62 ns, 4 times longer than the current pulse but 2.6 times shorter than the optical pulse obtained from PCO7810-40-4.

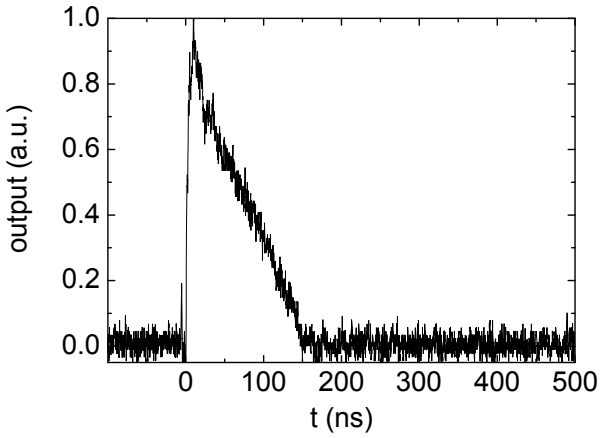

Figure 4.9. Optical pulse from the LR5C measured at 40 A drive current

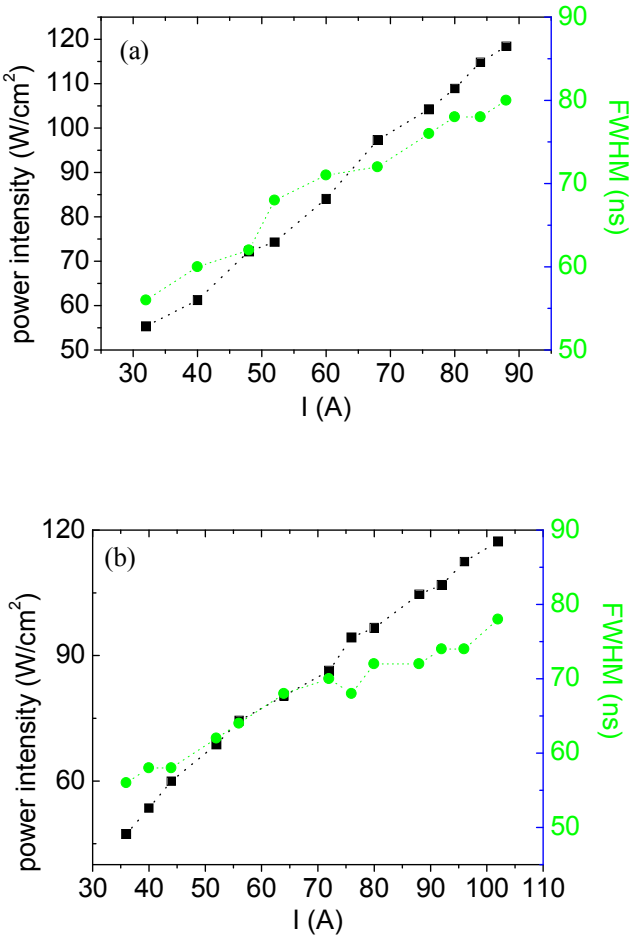

Figure 4.10. The impact of the current on the output power intensity and optical pulse width for LR3C (a) and LR5C (b)

Figure 4.10 shows the dependence of the optical pulse width and absolute power intensity on the drive current. Similar to Figure 4.7, an increase in the drive current slightly increased the optical pulse width from 60 ns to 80 ns. Despite the 20 ns increase of the optical pulse width, the maximum pulse width is only 80 ns for both LEDs and the highest peak power densities are 120 W/cm^2, significantly increasing the power intensity by a factor of 2.3 compared to the PCO-7810-40-4 driver and by a factor of 6 compared to DC operation.

In the previous measurements, the LEDs were connected to the circuit board via wires of 8 cm long, which functions as an additional RC circuit between the

circuit board and the LED and hence prolonging the optical pulse width. To further reduce the optical pulse width and to improve the output power intensity, the LEDs were directly soldered onto the circuit board. Emitter LEDs, PR02 and PR09, were used to replace the previous used LR3C and LR5C for soldering convenience. The output power of the emitter LEDs under DC driving is identical to the Star Hex LEDs. Figure 4.11 gives the output pulse of the directly mounted PR09.

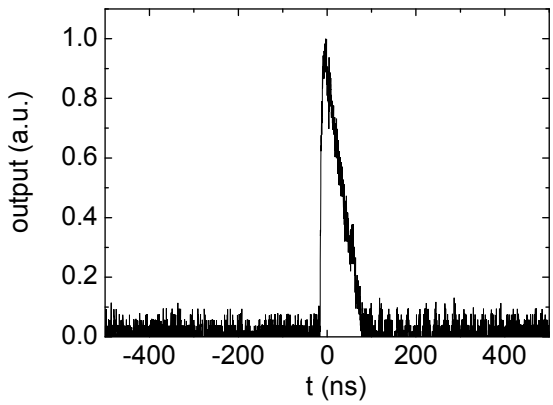

Figure 4.11. Optical pulse profile of the directly mounted PR09

A 45 ns output pulse was achieved at the maximum drive current of 120 A. The corresponding peak power intensity measured was increased to 197 W/cm^2, which is 1.6 times higher than that for the LR5C LED in Figure 4.10, matching well with the shortening of the optical pulse.

Using the same driver PCO-7100-120-15, a small further improvement in the output power intensity was achieved by using LXK2-PR14-Q00, the fifth LED in Table 4.I. This belongs to the LUXEON K2 series which has the lowest thermal resistance, and highest operation temperature of 185 ^{0}C. The better electronic and thermal designs increase the DC output power to 475 mW.

Figure 4.12 indicates the temporal profile of the optical and current pulses from the LED at the maximum current. Similar to the LUXEON III LEDs, the optical pulse width increased slightly with the drive current with the broadest pulse measured to be 50 ns.

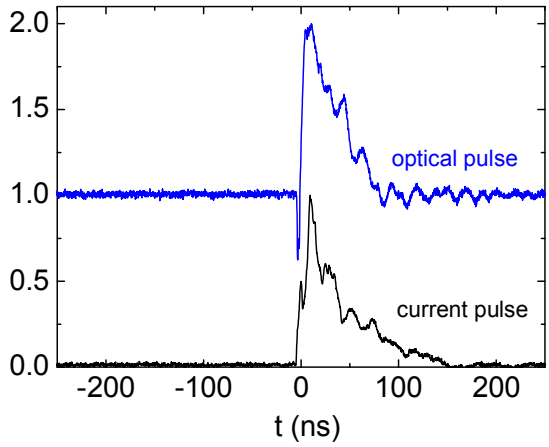

Figure 4.12. Optical and current pulse profile from LXK2-PR14-Q00, pulsed by PCO-7100-120-15

Figure 4.13 shows the dependence of the output energy and the corresponding peak power intensity on the drive current. The maximum drive current can be further increased from the quoted 120 A from the specification to 160 A by increasing the output of the high voltage unit slightly beyond the limit. In Figure 4.13, both the output energy and intensity increase linearly with the drive current. The highest power intensity, with a 50 ns optical pulse width across 1.5 mm by 1.5 mm LED chip, was measured to be 255 W/cm^2.

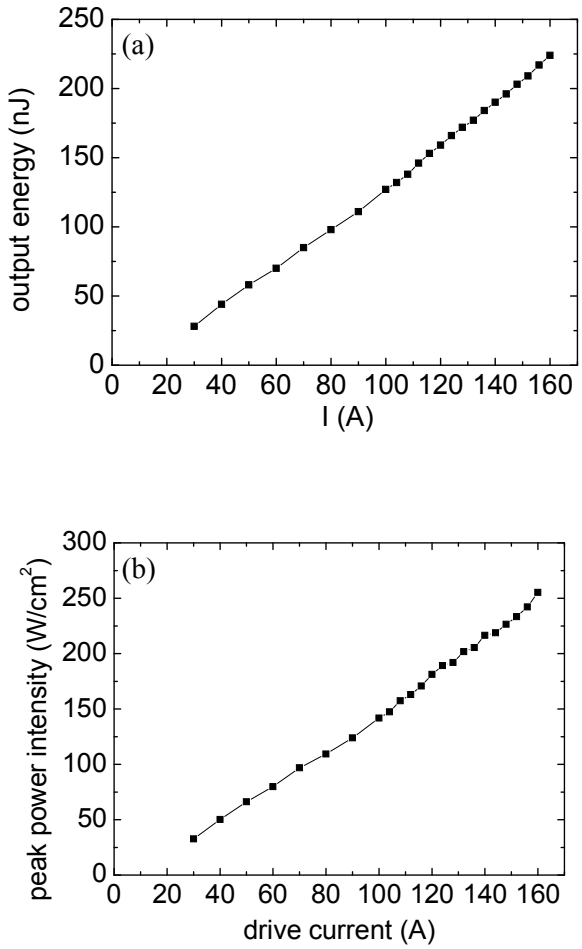

Figure 4.13. (a) Output energy and (b) power intensity of LXK2-PR14-Q00

As mentioned earlier, the normal threshold densities of organic lasers lie in the range from tens of W/cm^2 to tens of kW/cm^2 or even MW/cm^2, depending on the laser resonator design and the gain medium. Close to the lower limit of the lasing threshold requirement, the LED power intensity of 255 W/cm^2 is promising for achieving LED pumped organic lasers, as long as a suitable gain medium and a good resonator are used.

4.3. Pumping geometries

In this section, the suitability of two pumping geometries is investigated for pumping organic lasers with the LED. The gain medium used is the prototypical polymer MEH-PPV whose absorption spectrum overlaps well with the emission

spectrum of the blue LED with only 50 nm mismatch between the two peaks (shown in Figure 4.14). Although the thresholds of the MEH-PPV lasers are not the lowest in the literature, these lasers are suitable for testing the pumping geometries.

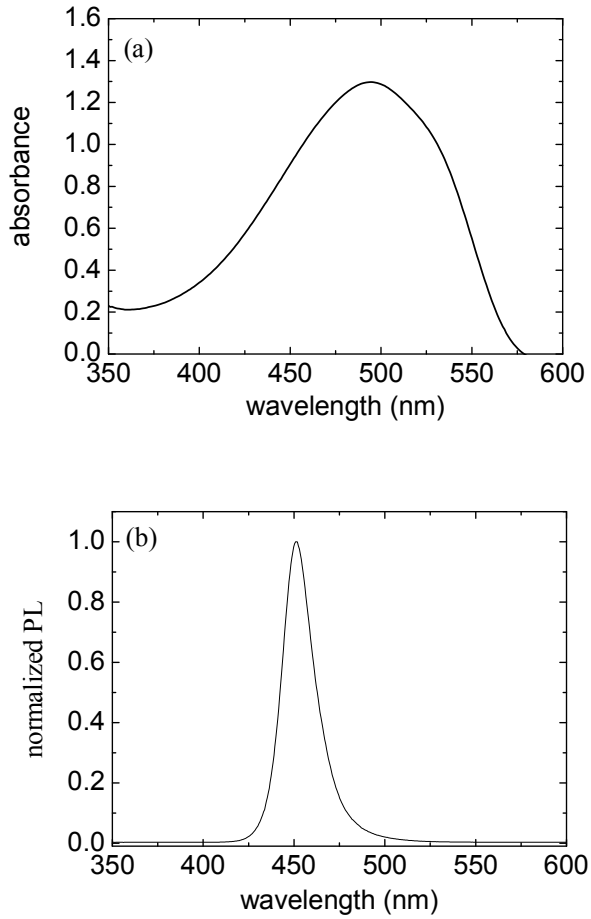

Figure 4.14. (a) Absorption spectrum of MEH-PPV and (b) LED emission spectrum of LXK2-PR14-Q00

The choice of the laser resonator is the distributed feedback (DFB) grating due to its ease of fabrication and attractive low lasing threshold. To use the LED as the pumping source, the first approach (referred to as the first case) was to spin coat the polymer layer directly onto the LED chip, ensuring that most of the LED emission can be absorbed. To complete the DFB resonator fabrication, gratings could be patterned onto the gain medium by soft lithography. However, the small chip area of 1.5 mm by 1.5 mm and the patterned circuits on the chip resulted in a

non-uniform film thickness and poor edge quality, which could lead to an increase in lasing threshold. Alternatively (referred to as the second case), to guarantee the quality of the polymer laser, the laser was fabricated by the normal procedure with an MEH-PPV layer coated on a corrugated silica substrate. Simulating the conventional pumping geometry, the LED chip is brought into contact with the silica substrate.

To test the suitability of these two pumping methods, specifically on how efficiently the LED emission can be absorbed by the MEH-PPV layer, the emission spectra with and without the MEH-PPV layer were measured in a calibrated integrating sphere, while the LED was DC driven. Pulsed LEDs should give similar results, since the MEH-PPV absorption is independent of excitation conditions. For both the first and the second cases, only planar films were coated on the chip or a glass substrate. Figure 4.15 and Figure 4.16 compares the emission spectra of the two pumping geometries.

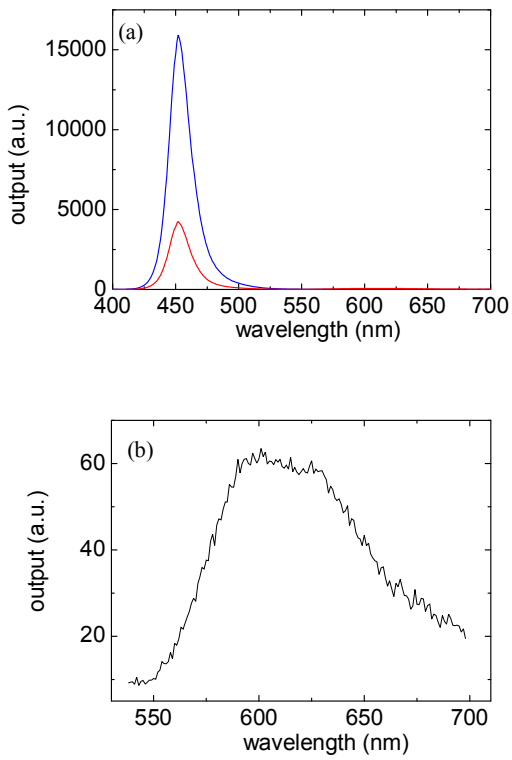

Figure 4.15. (a) Spectra of LED without (blue) and with (red) the MEH-PPV coated on the chip; (b) Enlarged spectrum of the red curve between 550 nm and 700 nm

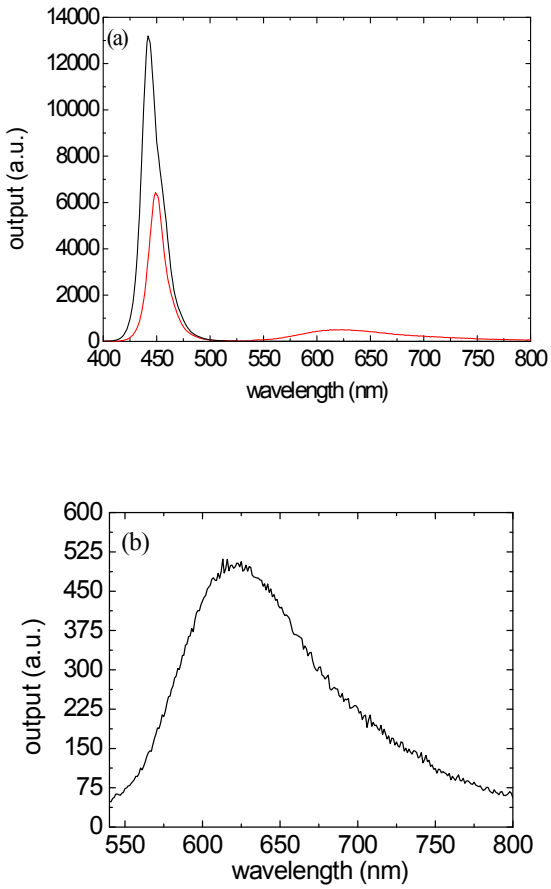

Figure 4.16. (a) Spectra of LED without (black) and with (red) MEH-PPV film coated on glass; (b) Enlarged spectrum of the red curve between 550 nm and 800 nm

For both cases, the reduction of the emission spectrum in the region of 450 nm at the presence of the MEH-PPV layer indicates the LED emission was absorbed by the MEH-PPV layer. The weak emission around 610 nm in the enlarged graphs arises from the emission from the MEH-PPV layer. It is obvious that the MEH-PPV layer absorbed a fraction of the LED emission and re-emitted in the red with spectra similar to the photoluminescence spectrum of MEH-PPV, both when MEH-PPV is coated on the chip and on a glass substrate. Table 4.IV lists the absorption fractions of the LED emission and the calculated fluorescence efficiencies of the MEH-PPV based on the absorbed LED emission.

	Absorption (%)	Fluorescence (%)
MEH-PPV on the chip	73	9
MEH-PPV on glass substrate	54	40

Table 4.IV. Comparison between two approaches

Directly spin coating the MEH-PPV layer on the LED chip can absorb 73% of the LED emission. It is more effective than coating the MEH-PPV on the glass substrate which wasted nearly half of the LED emission. However, 40% of the absorbed LED emission can be converted to the MEH-PPV emission in the second case, a factor of 4.5 higher than that in the first case. The 40% efficiency is close to the PLQY of MEH-PPV (52%). The lower fluorescence efficiency of the first case could be caused by the quenching and additional reabsorption losses introduced by the metal coated LED chip. The absorption and fluorescence efficiencies indicates that the separated active layer and the LED chip is more suitable than the direct coating approach for LED pumped laser.

4.4. Laser gain medium and resonator

The maximum power intensity of 255 W/cm^2 from the LXK2-PR14-Q00 sets the upper limit of the threshold for the organic lasers. To achieve low lasing threshold, an optimized combination of gain medium and laser resonator is critical. Diffractive resonators, for example DFB and distributed Bragg reflectors (DBR), are proven to give lower lasing thresholds compared to other resonators such as Fabry-Perot waveguide resonators [18-19], microcavity resonators [20-21] and microring resonators [22-23]. With some efforts to reduce the 2nd order output coupling loss, mixed 1st and 2nd order DFB resonators have been demonstrated to achieve lasing thresholds as low as 14 W/cm^2 with a polyfluorene derivative as the gain medium [16]. However, to fabricate such gratings in an area as large as 1.5 mm by 1.5 mm remains challenge for electron beam lithography. Similar difficulties exist for large area DBR resonators which gave low thresholds in laser diode pumped organic lasers [6]. DFB resonators, on the other hand, can be fabricated by holography to very large areas with relatively high quality and low

cost, as mentioned in **Chapter 3**, making it the choice for LED pumped organic lasers.

Besides the laser resonator, the appropriate choice of gain medium is very important. The material should have a strong absorption at the pump wavelength, in this case at 450 nm of the LED emission peak. In addition, it should exhibit high PLQY, high optical gain and low loss in the waveguide, and low excited-state absorption. Most of the lowest threshold lasers in the literature are based on blue emitting polyfluorene and its derivatives (e.g.: PFO, F8DP, BN-PFO) [24-27]. These materials absorb in the UV and hence not suitable for the blue LEDs. To reduce lasing thresholds, a lot of effort has been spent on characterizing suitable laser gain media in terms of their PLQY and lasing thresholds. In the following two sections, emphasis will be placed on two materials which give low lasing thresholds among these candidates. In the laser characterization, to simulate LED pumping conditions, the lasers were pumped at 450 nm by OPO with pump beams of 1.5 mm diameter.

4.4.1. MEH-PPV and its blends

MEH-PPV, as mentioned in **Section 4.3**, is a well developed and studied PPV derivative and capable of giving thresholds as low as a few kW/cm^2 [28]. As shown in Figure 4.14, it has a high absorbance at 450 nm in a 150 nm film. Figure 4.17 gives the absorption and photoluminescence spectra of MEH-PPV spin coated from chlorobenzene. It is red emitting with absorption peak at 500 nm. The emission spectrum shows two vibronic band structures at 590 nm and 625 nm respectively. Film PLQY as high as 50% can be achieved.

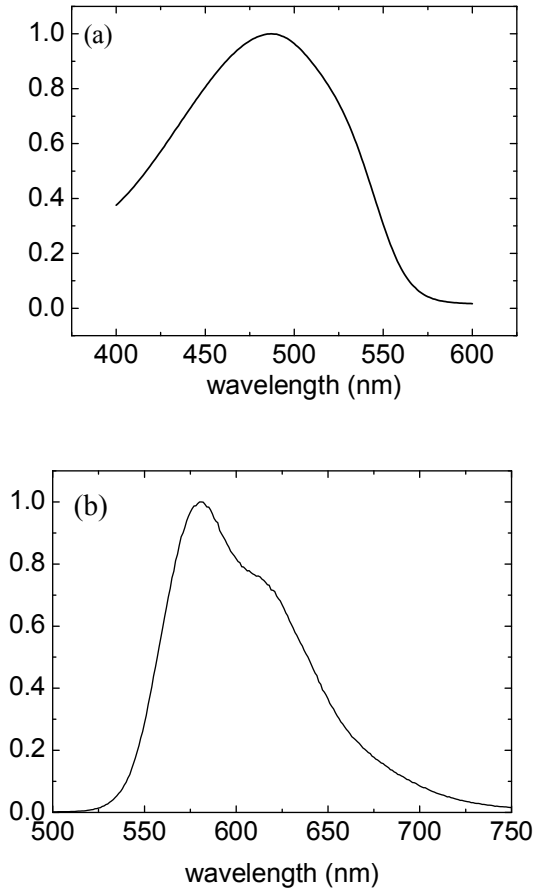

Figure 4.17. (a) Absorption and (b) photoluminescence spectra of MEH-PPV

Figure 4.18 shows the ASE line-narrowed spectrum from a film of MEH-PPV. The highest gain occurs at 625 nm with a 15 nm FWHM. Using the variable stripe method, as described in **Chapter 3**, the gain and loss are measured to be 38 cm^{-1} and 3.2 cm^{-1} respectively.

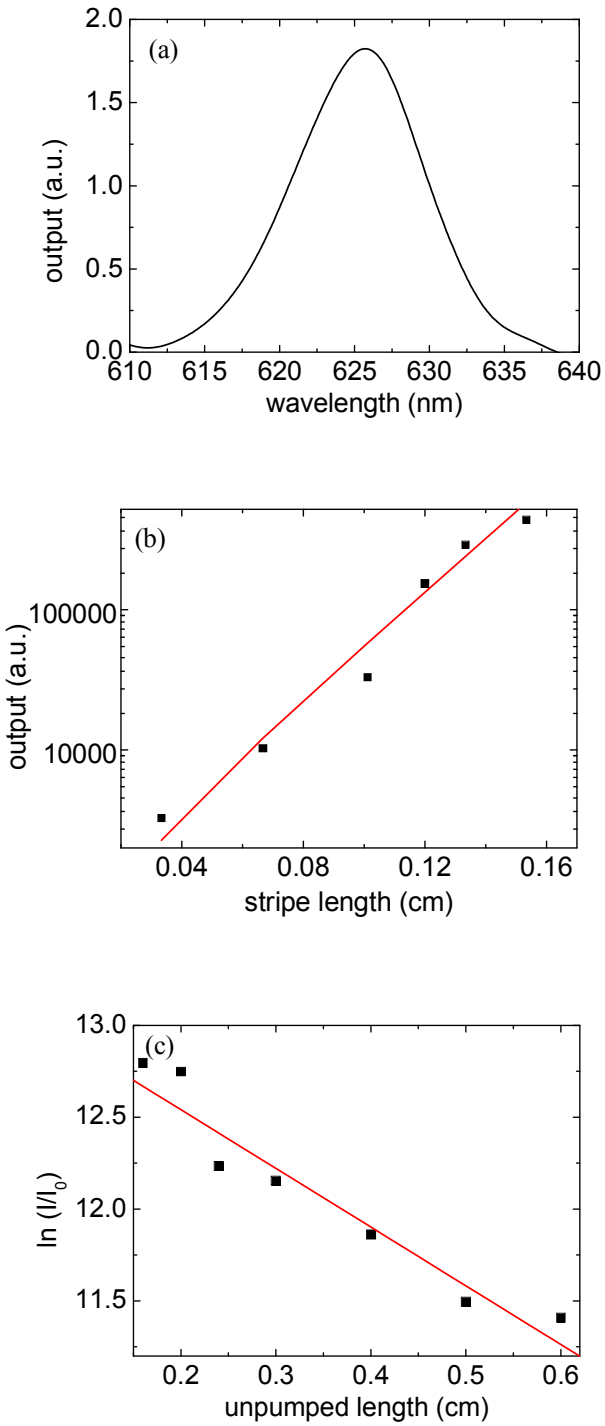

Figure 4.18. (a) ASE spectrum of MEH-PPV; (b) Gain; (c) Loss of MEH-PPV

The threshold and spectrum of an MEH-PPV DFB laser are given in Figure 4.19. When the pump energy increased, a sharp lasing peak near 630 nm with FWHM of 1.2 nm appeared. The threshold energy is 940 nJ, corresponding to 8.1 kW/cm^2.

This is 32 times higher than the peak power intensity from the blue LED, making it unsuitable for LED pumping.

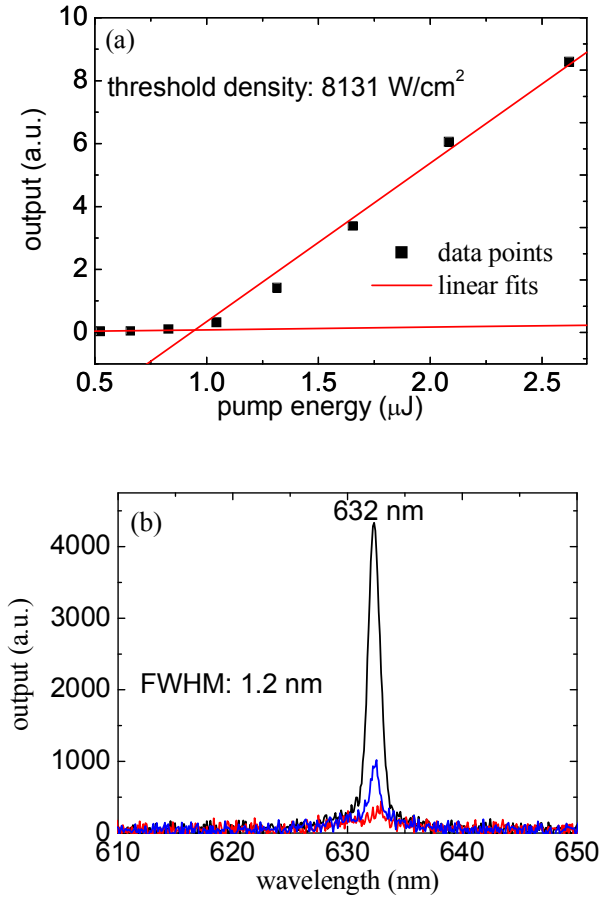

Figure 4.19. (a) MEH-PPV lasing threshold: (black square) experimental data and (red lines) linear fits for below and above thresholds; and (b) lasing spectrum

Vasdekis et. al. has demonstrated that blending MEH-PPV with coumarin 102 can effectively shift the absorption spectrum to the desired wavelength and reduce the ASE threshold in a laser diode pumped organic DBR laser [6]. A similar approach could be adapted here to increase the absorption at the LED emission wavelength of 450 nm by blending MEH-PPV with organic dyes. Non-radiative Forster energy transfer can occur between the excited donor dye molecules and the polymer acceptor (MEH-PPV). Such a blend also increases the separation of the absorption and PL spectra, due to the blue shift of the absorption spectrum, which can reduce reabsorption loss in the waveguide. The dye molecules could also

potentially change the packing condition of the polymer chains to prevent quenching and therefore increase PLQY.

With its absorption spectrum centred at 450 nm (shown in Figure 4.20), Coumarin 334 was chosen to blend with MEH-PPV.

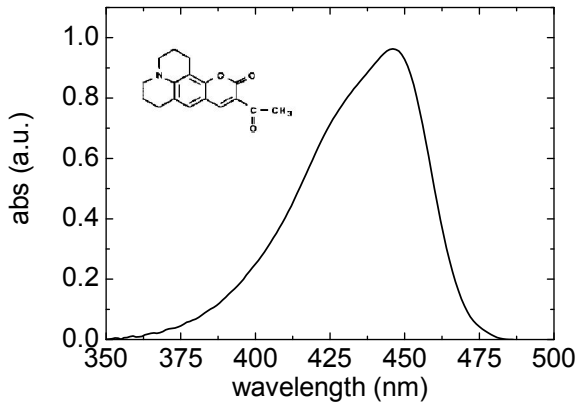

Figure 4.20. Absorption spectrum of Coumarin 334 in chlorobenzene; inset: molecular structure

Figure 4.21 shows the absorption and emission spectrum of several blends with different blending ratios. It can be observed that increasing the dye concentration shifted the absorption peak towards 450 nm. The PL spectrum slightly shifted to longer wavelengths by increasing dye concentration.

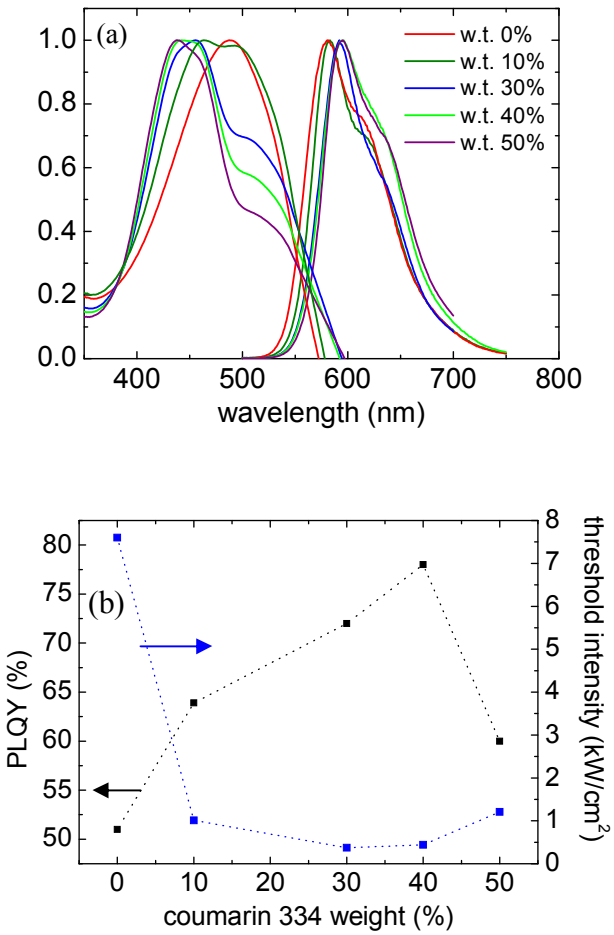

Figure 4.21. (a) Absorption and emission spectra of MEH-PPV blended with coumarin 334; (b)PLQY (black) and threshold intensity (blue) at different dye ratio

Figure 4.21 (b) shows the dependence of PLQY and lasing threshold on the coumarin dye concentration. The PLQY increased from 52% to 78% with the increase of the blending ratio of the dye molecules up to 40%, followed by a drop from 78% to 60% for the 50% blend, indicating 40% ratio is the optimized dye concentration. Similarly, blending the dye molecules reduced the lasing threshold by a factor of 20 from 7.8 kW/cm^3 to 370 W/cm^2. This lowest threshold is very close to the maximum power intensity of 255 W/cm^{2}from the LED. Although the coumarin 334 blended MEH-PPV could not be used as gain medium for the current blue LED, the low lasing threshold and high PLQY makes it still a very promising gain medium for future LED pumping, with the fast development of the InGaN technology and future improvements in low threshold resonators.

4.4.2. Fluorene- based Copolymer

Copolymers, like dye doped polymer blends, tend to give better laser performance with high gain and low loss due to their more separated absorption and photoluminescence spectra. Fluorene-based polymers have been demonstrated to give low threshold lasers in the order of between tens and hundreds of W/cm^2. Among the fluorene family, the yellow emitting copolymer poly(9,9-dioctylfluorene-co-benzothiadiazole) (F8BT) [29-30] presents strong absorption at 450 nm. However, its lasing threshold is higher than its blue counterparts mentioned ealier. The same occurs for the proprietary red-emitting material Lumation Red F [31].Recently, a new fluorene-based copolymer, poly[(9,9-dioctylfluorenyl-2,7-diyl)-co-(1,4-benzo-(2,1',3) -thiadiazole)] (ADS 233YE) became commercially available and has been proved to be an excellent material in optical amplifiers [32]. ADS 233 YE comprises F8 and BT units with ratio of 9 to 1 in the core. Figure 4.22 shows its absorption and photoluminescence spectra together with its molecular structure.

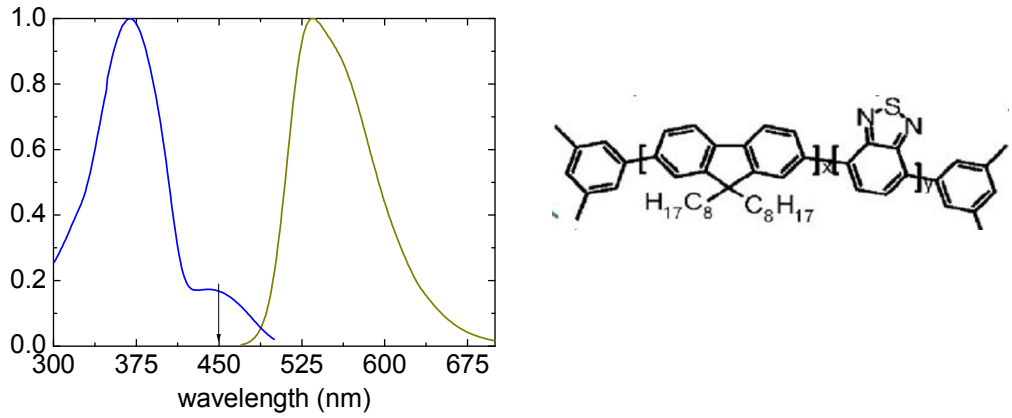

Figure 4.22. (Left) absorption (blue)and PL spectrum (black) of ADS 233YE and (right) its molecular structure (x:y=9:1)

In Figure 4.22, two peaks appear in the absorption spectrum at 375 nm and 450 nm, corresponding to F8 and F8BT units respectively. The much stronger 375 nm

peak is caused by the existence of larger number of F8 units than BT. The emission spectrum is similar to the F8BT PL spectrum with a peak at 535 nm, and shows no emission from the F8 unit at 450 nm. This indicates the efficient energy transfer from F8 to localised F8BT. For compatibility with LED pumping, the low energy F8BT sites are directly excited at 450 nm. This means that no energy transfer occurs in the copolymer and the F8 units only act as passive spacers to prevent potential aggregation quenching of the localised F8BT.

To find the peak gain wavelength of the copolymer, ASE experiments were undertaken with a pump wavelength at 450 nm on a 150 nm thick film. Figure 4.23 shows the resulting ASE spectrum. The ASE is centred at 559 nm with a FWHM of 15 nm. The input vs output curve confirms a threshold around 440 nJ/pulse, accompanied with a reduction in the FWHM from 26 nm to 15 nm. The refractive index of the material was measured between 200 nm and 800 nm by ellipsometry. The refractive index at the ASE peak (559 nm) is 1.68. This is lower than many polymers. For instance, MEH-PPV and PFO have refractive indices of 1.8.

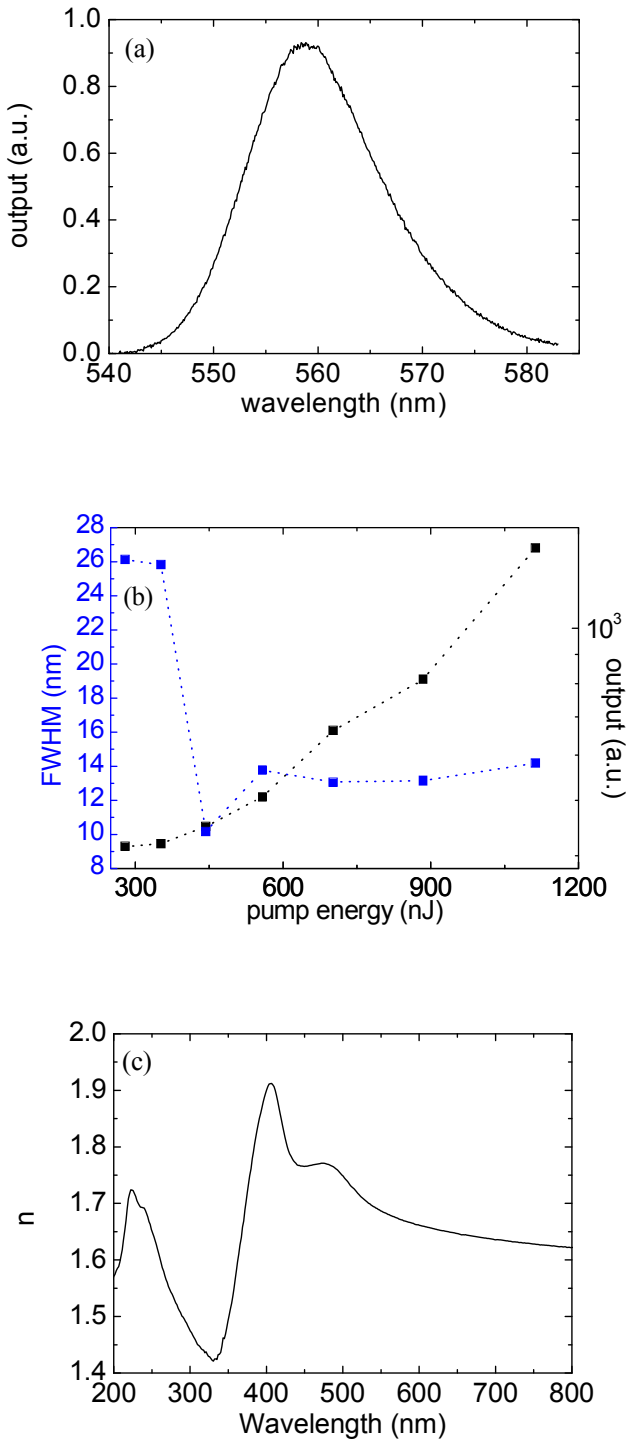

Figure 4.23. (a) ASE spectrum of ADS 233YE; (b) The dependence of the FWHM and output on the pump energy; (c) Refractive indices from 200 nm to 800 nm

Usually, for polymer DFB lasers, the film thickness should be thin (typically ~100 nm) to support only the lowest order transverse mode. A thicker film could result

in transverse mode competition and a reduced interaction between the guided mode and the diffraction gratings, leading to an increase in lasing threshold. For ADS 233 YE, the cut-off film thickness to support the first transverse mode in the air-polymer-silica waveguide is just below 120 nm. Figure 4.24 plots the profile of the fundamental TE_0 mode for a film of 120 nm thickness. The low refractive index (1.68) in the copolymer results in a strong penetration of the guided mode into the substrate. It reduces the overlap between the guided mode and the active polymer layer and hence potentially increases the lasing threshold. Therefore, thicker films are preferred for better waveguiding and to minimize lasing threshold for ADS 233YE.

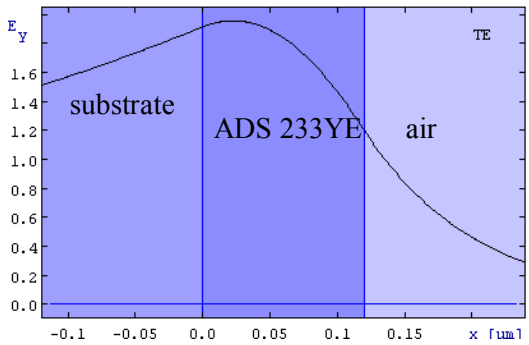

Figure 4.24. TE_0 mode profile (black curve) for a 120 nm thick film. (from http://wwwhome.math.utwente.nl/~hammer/oms.html)

Additionally, thicker film can improve the absorption at 450 nm. Figure 4.25 exhibits the absorption of the film in percentage at 450 nm with thickness varied from 133 nm to 356 nm. The increase of the film thickness increased the absorption by a factor of 3 from 20% to 60%. Compared to the previously discussed MEH-PPV and its blends, which show a 90% absorption from a 150 nm thick film, the absorption of ADS 233 YE is significantly lower. The weaker absorption in the copolymer could waste pump energy, making it less attractive for LED pumping. To increase the absorption, a dielectric mirror (520 IY, Comar Ltd.) was added on the back side of the substrate to double pass the pump beam back through the polymer layer. The dielectric mirror has a high reflectivity more than 99.9% between 400 and 475 nm, overlapping well with the LED emission spectrum.

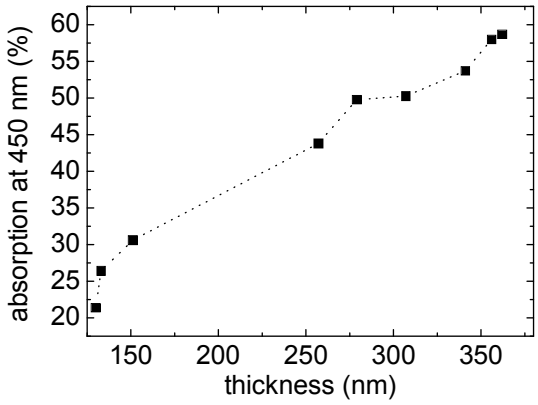

Figure 4.25. Absorption of ADS 233YE of different film thickness

The next step was to optimize the design of the DFB laser to achieve low threshold lasing. To make a DFB laser, a grating of 373 nm period was initially used, coated with a thin film of ADS 233YE. To optimize lasing threshold, a range of film thickness was tried, as shown in Figure 4.26.

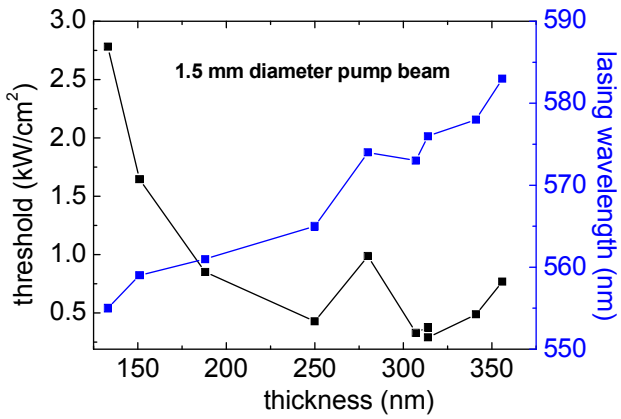

Figure 4.26. Lasing threshold (black) and wavelength (blue) for different film thickness

The threshold intensity decreased with the increase of the film thickness, reaching its lowest value of 289 W/cm^2 with lasing wavelength of 576 nm, when the film thickness was 314 nm. This threshold is closer to the maximum power intensity from the LED (255 W/cm^2) than the coumarin dye doped MEH-PPV. For the 373 nm grating period, according to the Bragg equation, to get the lasing wavelength close to the ASE peak at 560 nm, the effective refractive index should be 1.5 by

assuming a flat silica substrate. The corresponding film thickness of the copolymer was calculated to be 180 nm, which one might expect to give the lowest threshold. The 180 nm thick film, however in Figure 4.26, had high threshold intensity of 852 W/cm^2, though its lasing wavelength was close to the ASE peak at 561 nm as expected. The origin for the higher threshold of the 180 nm film than the 314 nm film could be due to the poor overlap between the guided mode and the gain medium in the 180 nm thin layer, as discussed earlier. The threshold intensity then started increasing again for thicker films due to the increasing mismatch of the lasing wavelengths (~ 580 nm) and the ASE peak (560 nm).

A further reduction of the lasing threshold could be achieved by blue shifting the lasing wavelength to the ASE peak to experience larger gain, while maintaining the film thickness at around 300 nm to have a good waveguiding effect. This could be achieved by reducing the grating period Λ to compensate for the larger n_{eff} in the thicker layer. A 1D grating with period of 355 nm was therefore used. Similar to the optimization done for the 373 nm grating, the film thickness was varied to obtain the lowest threshold intensity. Figure 4.27 presents the lasing threshold and spectrum of the lowest threshold laser. The AFM image of the 355 nm grating is given in Figure 4.28.

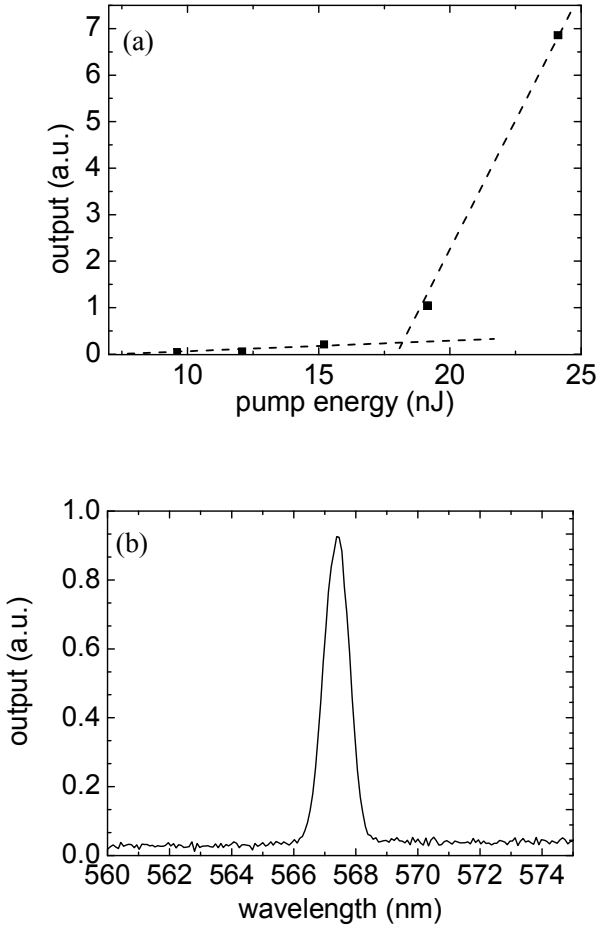

Figure 4.27. (a) Input vs output curve; (b) Lasing spectrum pumped at 24 nJ/pulse (the threshold obtained with the 520 IY filter)

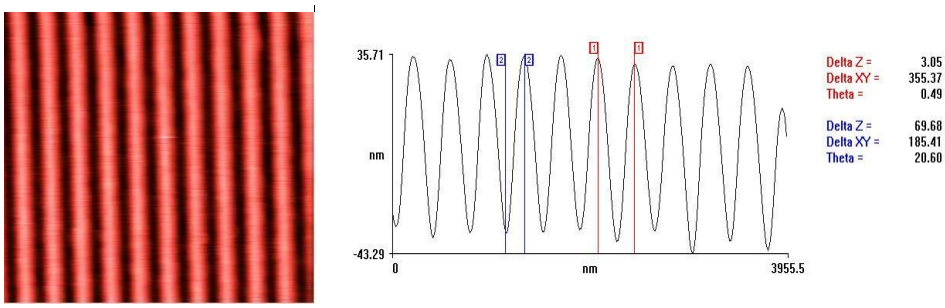

Figure 4.28. AFM scan of the 355 nm grating:
(left) Area of 4 μm by 4 μm; (right) Cross section of the grating

The AFM scan shows that the holographic gratings have good uniformity with a modulation depth of 70 nm. When a 307 nm thick film was coated on this grating, the threshold intensity reached the lowest value of 160 W/cm^2, corresponding to

18 nJ/pulse. The FWHM of the lasing peak measured with a pump energy of 24 nJ (1.5 times above the threshold) was 1.1 nm, limited by the resolution of the spectrograph. Compared to the threshold obtained with the 373 nm grating, the threshold intensity is reduced by a factor of 1.5, with the lasing wavelength shifting from 576 nm to 567 nm.

4.4.3. LED pumped polymer laser

The low threshold intensity of the ADS 233YE copolymer DFB laser is 1.6 times lower than the maximum power intensity from the blue InGaN LED, which improves the possibility of having the LED as the pumping source. A remaining issue was how to encapsulate the laser before combining it with the LED. As discussed in **Chapter 2**, polymer lasers normally are vulnerable to oxygen and water in the surrounding environment, which demands encapsulation to prolong their lifetimes. It has been demonstrated that encapsulation with curable Norland UV glue can efficiently increase the lifetime of the polymer lasers by a factor of 2500, making it equivalent to the lifetime in vacuum [33]. However, such an encapsulation approach makes it difficult to remove the encapsulation and reuse the glass corrugated substrate. Alternatively, temporary encapsulations, such as spin coating transparent passive polymer layer on top of the gain layer, can also extend the lifetime of the polymer laser, though not as robustly as the permanently encapsulated devices.

The material used for encapsulating the ADS 233 YE laser was CYTOP. CYTOP is a highly innovative amorphous fluoropolymer invented by ASAHI GLASS company in Japan. It is highly transparent in the visible and UV with a low refractive index of 1.35 and is processed with solvents which would not redissolved the underlying ADS 233 YE layer.

To complete the encapsulation, a CYTOP layer was spin coated on to the ADS 233YE copolymer layer. The CYTOP layer shows little impact on the lasing threshold and wavelengths. A degradation study was carried out using the OPO

with pump energy at 1.7 times above the lasing threshold, simulating the LED pumping situation, because the maximum power intensity from the LED is 1.6 times higher than the lowest threshold of the copolymer laser. Figure 4.29 shows the laser performance within the first 100 minutes. The lasing peak at 568 nm fluctuated about the average counts of 1800 and exhibited no obvious decrease. The fluctuation could be due to the instability of the OPO pump laser energies. No obvious degradation validates the effectiveness of the CYTOP layer as the temporary encapsulation for ADS 233YE. Besides slowing down the degradation, another advantage of having an encapsulation layer on top of the gain medium is to prevent the potential physical damage of the copolymer layer, when the LED is brought into contact with the polymer laser. The low refractive index of the CYTOP makes it also a good cladding buffer layer between the LED chip and the ADS 233YE layer.

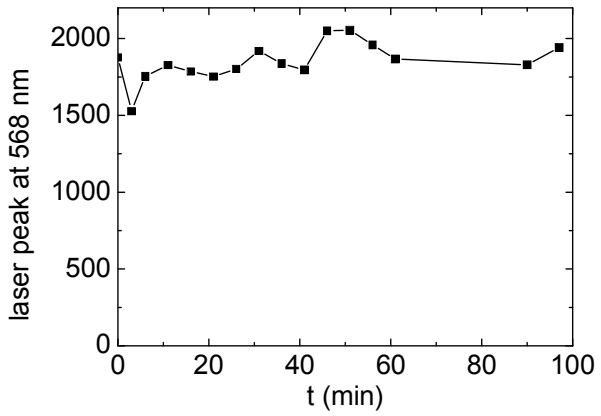

Figure 4.29. Degradation of the ADS 233YE copolymer laser in air

To perform LED pumping, the copolymer laser was initially pumped by the OPO at 450 nm to ensure the threshold intensity is lower than the LED maximum output power intensity. The lasing spectra obtained from the OPO pumping will be used to compare with the spectra observed under LED excitation. Figure 4.30 shows the lasing threshold is 27 nJ/pulse (208 W/cm^2), slightly higher than the threshold obtained previously.

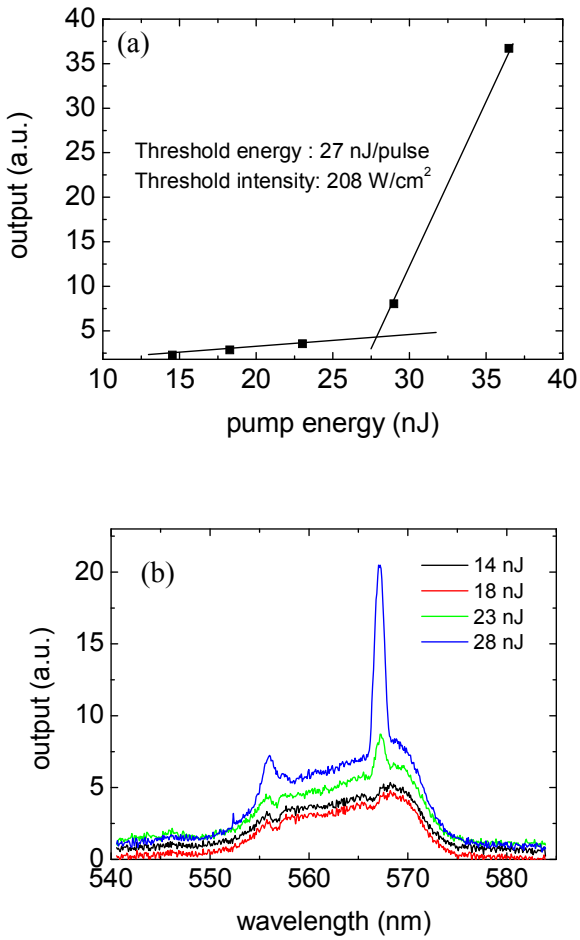

Figure 4.30. ADS 233YE (a) laser threshold and (b) spectra under different pump energies by OPO

The slight increase of the threshold could be attributed to a small difference in the copolymer film thickness and the grating quality of the pumped area. When the laser was below threshold (at pump energy of 14 nJ/pulse), two Bragg stop bands were observed at 555 nm and 568 nm, corresponding to the TE_0 and TM_0 transverse mode respectively. When the pump energy increased from 14 nJ to 28 nJ, the emission at 568 nm increased faster than the output at 555 nm, showing threshold intensity of 208 W/cm^2. The 555 nm mode has slightly higher threshold because of its lower modal confinement. The angle dependent PL measurement of the laser structure, exited by a 390 nm diode laser, clearly shows the existence of these waveguide modes (shown in Figure 4.31).

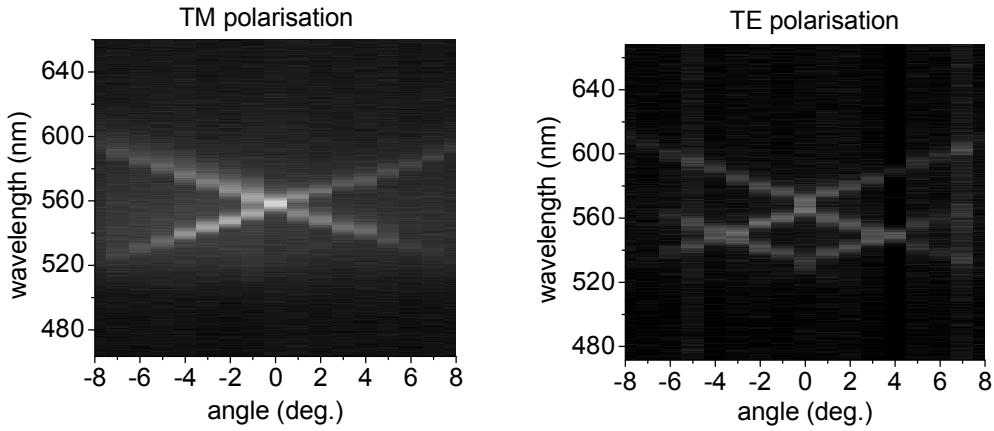

Figure 4.31. Angle dependent PL measurement of the laser resonator: the 0° is parallel to the normal direction of the film

Besides the TE_0 mode, the TE_1 mode located at 530 nm can also be observed. However, no lasing peak appeared in this mode, since its wavelength overlaps with the tail of the absorption in ADS 233 YE.

The left figure in Figure 4.32 sketches the pumping setup for the LED pumped polymer laser. The LED was connected to the PCO-120-15 driver which provides up to 160 A current in 15 ns pulse. The output power is as high as 255 W/cm^2 as discussed in Figure 4.13. On the other side of the polymer laser, the high reflective 520 IY filter was used to reflect the blue pump beam back into the ADS 233YE layer to increase the absorption efficiency at the LED emission. The yellow arrows are the indicators of the laser beam in the feedback and output directions from the first and second order scattering of the DFB resonator.

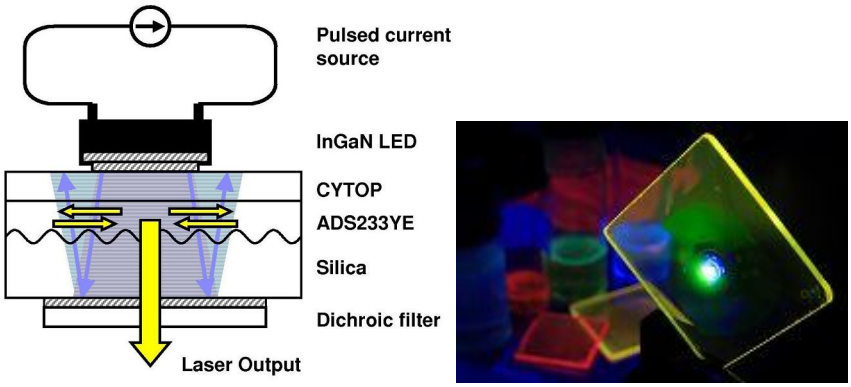

Figure 4.32. Sketch (left) and the picture (right) of the LED pumped polymer laser

In Figure 4.33, when the polymer laser was excited by the LED, two Bragg bands, corresponding to the TE_0 and TM_0 modes, appeared in the output spectra at the similar wavelengths observed from the OPO pumped spectra below thresholds. The exact spectrum is very sensitive to the position of the detector, which could account for the small change in the shapes of the spectra in comparison to the OPO pumped spectra. When the drive current was increased, the output energy from the polymer laser increased linearly at both 555 nm and 568 nm till 152 A. A sharp peak with a FWHM of 1.1 nm began to rise at 568 nm and became more and more obvious as the current continued to increase. The input vs output plot at 568 nm shows a clear threshold around 150 A. On the contrary, the output energy at 555 nm increased always linearly with the LED drive current. Both the spectra and the input vs output plot suggest that the LED successfully pumped the laser above the threshold.

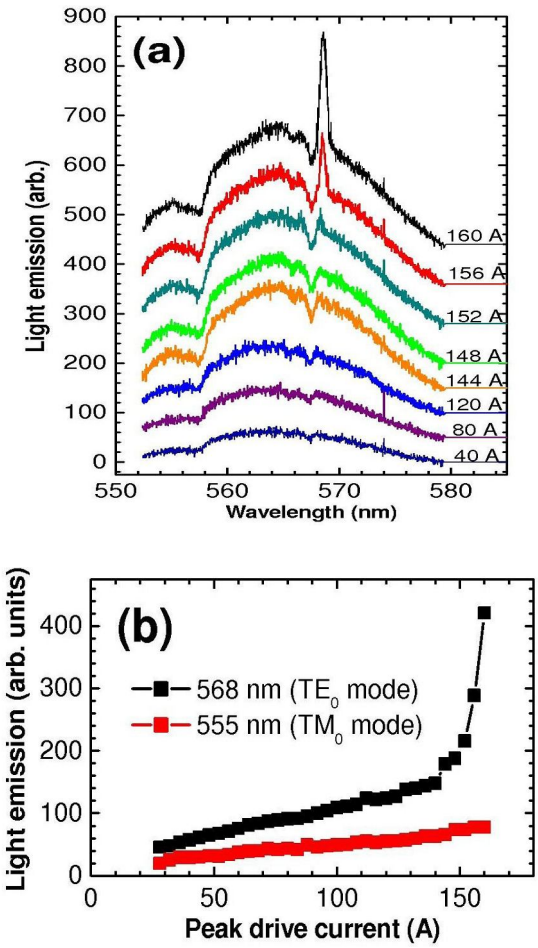

Figure 4.33. LED pumped polymer laser: (a) Spectra under different drive current ; (b) Input vs output plots of emission at 568 nm and 555 nm

To eliminate the strong PL background in the spectra above the lasing threshold in Figure 4.33 requires higher pump power to excite the laser further above the threshold. It is shown in Figure 4.34 that the peak at 568 nm can dominate the output spectrum as the pump energy increased to 36 nJ by using the OPO as the pump source. To achieve this pump power intensity with the LED, the drive current should be further increased to 175 A, assuming the linear relationship between the drive current and the output power intensity preserves.

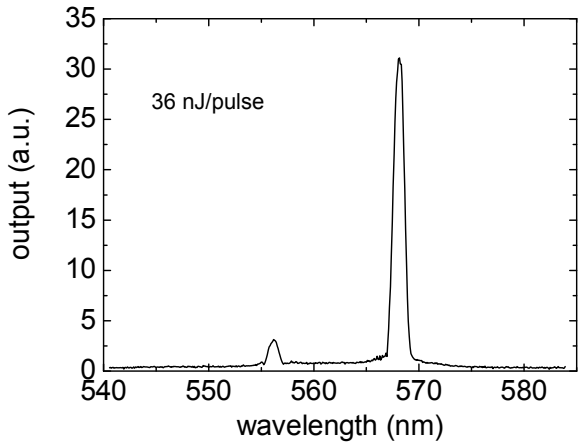

Figure 4.34. Spectrum recorded at 36 nJ pump energy with OPO

4.5. Conclusion

In this chapter, the suitability of using LEDs as the pumping sources for polymer lasers was investigated, leading to the world's first demonstration of an LED pumped organic laser. A series of high power blue LEDs were purchased from LUMILED Ltd. The highly divergent incoherent emission of the LEDs makes it difficult to collect and refocus the output beam effectively. To address this, the encapsulation dome of the LED was removed to expose the LED chip which would be coupled directly onto the surface of the polymer laser. To achieve high output power intensity, these blue Lumiled LEDs were pulsed by two different laser diode drivers with high current amplitude in short pulse of nanosecond. With the PCO-120-15 driver, the Luxeon K2 LED, LXK2-PR14-Q00, gave the highest output power intensity of 255 W/cm^2, nearly an order of magnitude higher than the power intensity obtained under DC driven.

To minimize the threshold densities of organic semiconductor lasers, the gain medium was carefully selected. Different polymers and blends were characterized. The yellow emitting fluorene-based copolymer ADS 233YE, consisting of F8 and BT units in the core with the ratio of 9 to 1, was chosen as the most suitable gain medium for the surface emitting DFB laser. It has a low lasing threshold intensity of 160 W/cm^2, making LED pumped laser very promising. To slow down the photo-oxidation of the polymer laser, a highly transparent temporary encapsulation layer of CYTOP was coated onto the gain layer. The encapsulated polymer laser show no degradation in the output within the first 100 minutes, when it was pumped 1.6 times above the threshold. With the LED as the pump source, the polymer laser started lasing at 152 A, corresponding to 233 W/cm^2 in power intensity. The lasing was accompanied by the appearance of a sharp peak at the edge of the Bragg stop band together with a change in the output slope efficiency. The limitation of the maximum output power intensity of the LED resulted in a strong PL background in the output spectra of the LED pumped laser. When pumped by OPO, it was demonstrated that the lasing peak would quickly dominate the output spectrum, if the pump intensity could be increased to 278 W/cm^2, requiring the LED drive current to be increased by only 9.3%.

In summary, the world's first LED pumped polymer laser was demonstrated as an alternative approach of direct electrically pumped organic lasers. The successful integration of the high power nitride LED with the polymer laser is very promising towards the practical application of polymer lasers with substantial reduction in the complexity, size and cost of the pump source.

4.6. Reference

[1] N. Tessler, G.J. Denton, and R.H. Friend, *Nature*, 1996. **382**(6593): p. 695-697.

[2] G. Heliotis, R. Xia, D.D.C. Bradley, G.A. Turnbull, I.D.W. Samuel, P. Andrew, and W.L. Barnes, *Applied Physics Letters*, 2003. **83**(11): p. 2118-2120.

[3] G.A. Turnbull, P. Andrew, W.L. Barnes, and I.D.W. Samuel, *Applied Physics Letters*, 2003. **82**(3): p. 313-315.

[4] S. Riechel, U. Lemmer, J. Feldmann, S. Berleb, A.G. Muckl, W. Brutting, A. Gombert, and V. Wittwer, *Optics Letters*, 2001. **26**(9): p. 593-595.

[5] T. Riedl, T. Rabe, H.H. Johannes, W. Kowalsky, J. Wang, T. Weimann, P. Hinze, B. Nehls, T. Farrell, and U. Scherf, *Applied Physics Letters*, 2006. **88**(24): p. 241116.

[6] A.E. Vasdekis, G. Tsiminis, J.C. Ribierre, L. O'Faolain, T.F. Krauss, G.A. Turnbull, and I.D.W. Samuel, *Optics Express*, 2006. **14**(20): p. 9211-9216.

[7] M. Redecker, D.D.C. Bradley, M. Inbasekaran, and E.P. Woo, *Applied Physics Letters*, 1998. **73**(11): p. 1565-1567.

[8] N.C. Giebink and S.R. Forrest, *Physical Review B*, 2009. **79**(7): p. 073302.

[9] H. Yamamoto, H. Kasajima, W. Yokoyama, H. Sasabe, and C. Adachi, *Applied Physics Letters*, 2005. **86**(8): p. 083502.

[10] T. Matsushima, H. Sasabe, and C. Adachi, *Applied Physics Letters*, 2006. **88**(3): p. 033508.

[11] E.B. Namdas, J.S. Swensen, P. Ledochowitsch, J.D. Yuen, D. Moses, and A.J. Heeger, *Advanced Materials*, 2008. **20**(7): p. 1321.

[12] H. Morkoc and S.N. Mohammad, *Science*, 1995. **267**(5194): p. 51-55.

[13] F.A. Ponce and D.P. Bour, *Nature*, 1997. **386**(6623): p. 351-359.

[14] S. Nakamura, *Science*, 1998. **281**(5379): p. 956-961.

[15] A. Rose, Z.G. Zhu, C.F. Madigan, T.M. Swager, and V. Bulovic, *Nature*, 2005. **434**(7035): p. 876-879.

[16] C. Karnutsch, C. Pflumm, G. Heliotis, J.C. Demello, D.D.C. Bradley, J. Wang, T. Weimann, V. Haug, C. Gartner, and U. Lemmer, *Applied Physics Letters*, 2007. **90**(13): p. 131104.

[17] T. Rabe, K. Gerlach, T. Riedl, H.H. Johannes, W. Kowalsky, J. Niederhofer, W. Gries, J. Wang, T. Weimann, P. Hinze, F. Galbrecht, and U. Scherf, *Applied Physics Letters*, 2006. **89**(8): p. 081115.

[18] V.G. Kozlov, V. Bulovic, P.E. Burrows, and S.R. Forrest, *Nature*, 1997. **389**(6649): p. 362-364.

[19] V.G. Kozlov and S.R. Forrest, *Current Opinion in Solid State & Materials Science*, 1999. **4**(2): p. 203-208.

[20] V. Bulovic, V.G. Kozlov, V.B. Khalfin, and S.R. Forrest, *Science*, 1998. **279**(5350): p. 553-555.

[21] T. Virgili, D.G. Lidzey, M. Grell, D.D.C. Bradley, S. Stagira, M. Zavelani-Rossi, and S. De Silvestri, *Applied Physics Letters*, 2002. **80**(22): p. 4088-4090.

[22] S.V. Frolov, M. Shkunov, Z.V. Vardeny, and K. Yoshino, *Physical Review B*, 1997. **56**(8): p. R4363-R4366.

[23] Y. Kawabe, C. Spiegelberg, A. Schulzgen, M.F. Nabor, B. Kippelen, E.A. Mash, P.M. Allemand, M. Kuwata-Gonokami, K. Takeda, and N. Peyghambarian, *Applied Physics Letters*, 1998. **72**(2): p. 141-143.

[24] G. Heliotis, R.D. Xia, G.A. Turnbull, P. Andrew, W.L. Barnes, I.D.W. Samuel, and D.D.C. Bradley, *Advanced Functional Materials*, 2004. **14**(1): p. 91-97.

[25] T. Rabe, M. Hoping, D. Schneider, E. Becker, H.H. Johannes, W. Kowalsky, T. Weimann, J. Wang, P. Hinze, B.S. Nehls, U. Scherf, T. Farrell, and T. Riedl, *Advanced Functional Materials*, 2005. **15**(7): p. 1188-1192.

[26] C. Karnutsch, C. Gyrtner, V. Haug, U. Lemmer, T. Farrell, B.S. Nehls, U. Scherf, J. Wang, T. Weimann, G. Heliotis, C. Pflumm, J.C. deMello, and D.D.C. Bradley, *Applied Physics Letters*, 2006. **89**(20): p. 201108.

[27] W.Y. Lai, R.D. Xia, Q.Y. He, P.A. Levermore, W. Huang, and D.D.C. Bradley, *Advanced Materials*, 2009. **21**(3): p. 355-360.

[28] A.E. Vasdekis, G.A. Turnbull, I.D.W. Samuel, P. Andrew, and W.L. Barnes, *Applied Physics Letters*, 2005. **86**(16): p. 161102.

[29] R.D. Xia, G. Heliotis, and D.D.C. Bradley, *Applied Physics Letters*, 2003. **82**(21): p. 3599-3601.

[30] R. Xia, G. Heliotis, P.N. Stavrinou, and D.D.C. Bradley, *Applied Physics Letters*, 2005. **87**(3): p. 031104.

[31] G. Heliotis, R. Xia, D.D.C. Bradley, G.A. Turnbull, I.D.W. Samuel, P. Andrew, and W.L. Barnes, *Journal of Applied Physics*, 2004. **96**(12): p. 6959-6965.

[32] D. Amarasinghe, A. Ruseckas, A.E. Vasdekis, G.A. Turnbull, and I.D.W. Samuel, *Advanced Materials*, 2009. **21**(1): p. 107-110.

[33] S. Richardson, O.P.M. Gaudin, G.A. Turnbull, and I.D.W. Samuel, *Applied Physics Letters*, 2007. **91**(26): p. 261104.

Chapter 5

The Development of Luminescent Concentrator for Pumping Organic Lasers

5.1. Introduction

In **Chapter 4**, the first LED pumped polymer laser has been successfully demonstrated. A lasing peak was observed at the Bragg band edge, when the polymer laser was pumped above the threshold. However, the performance of the polymer laser is limited by the output power intensity from the blue LED. A strong Bragg scattered photoluminescence background was comparable to the lasing peak. Higher pump energy is required to remove the PL background to make the polymer laser function properly. Currently, the LED was pulsed by a high current pulse of tens of nanoseconds. It is possible that further enhancement in the drive current or compression in the pulse width could cause saturation in the LED output power or, even worse, damage of the LED, since the drive condition was close to the extreme of the LED. As a result, it is better to find an alternative approach to improve the LED power intensity.

Focussing the LED beam is another effective approach to increase the power intensity. However, as proven in **Chapter 4**, the incoherent nature of the LED emission makes it difficult for light focussing with conventional imaging technique. On the other hand, non-imaging optics finds their applications in a

wide range of areas [1-3]. It distinguishes itself from imaging technique by not preserving the phase information of the object and thus only concerns with the optimal transfer of light radiation between a source and a target [4]. Hence, the focused spot is not limited by the size, or the divergence of the incident beam. Usually, it involves the design of the light path between the source and the target to change the angular and spatial distribution of the radiation so as to maximize the intensity or flux incident on the target. Therefore, non imaging optics could be a promising approach for increasing the LED power intensity.

As one category of non-imaging techniques, luminescent concentrators (LCs) have been the subject of studies in solar cells for achieving low cost and high photovoltaic conversion efficiency since the 1980s. It is proved to be efficient in harvesting and transporting energies [5-7]. Hence, it could be useful to collect and reshape the LED emission.

Many challenges need to be coped with to make the LCs operate as expected for organic semiconductor lasers. In this chapter, the suitability of using a LC for LED power intensity enhancement and thus threshold reduction in polymer lasers is investigated.

The principle of the LC is introduced in **Section 5.2**. The difference between the LC used for polymer lasers and those used in solar systems are also discussed. **Section 5.3** shows the experimental methods for LC characterization. Optimization of the LC performance is discussed in **Section 5.4**. It involves the selection of active and passive materials, film thickness adjustment and the studies of PLQY, absorbance and waveguide losses. A theoretical model has been developed in **Section 5.5** to understand and predict the performance of the LC, based on which further optimization of the LC was carried out in **Section 5.6**.

Section 5.7 and **Section 5.8** emphasize on polymer lasers in terms of the laser gain medium and the impact of pump beam on the lasing threshold. A term of effective light concentration ratio is introduced in **Section 5.9** to predict the threshold reduction for a LC pumped polymer lasers according to the results obtained in the previous two sections. LC pumped polymer lasers are tested experimentally in **Section 5.10** for both 1D and 2D DFB lasers.

5.2. Principles of Luminescent concentrator (LC)

A LC is a thin flat slab containing highly fluorescent dyes (represented by the small dots in the Figure 5.1) dispersed in a transparent passive matrix. The dye molecules absorb light incident on the surface and reemit in another wavelength because of the Stokes shift between its absorption and photoluminescence spectra. Usually, the refractive index of the matrix is higher than the substrate. A waveguide between the matrix layer and the substrate can be formed. Much of the re-emitted light will be travelling through total internal reflection (TIR) of the waveguide towards the edge of the film. In practice, conventional plastic solar concentrators are formed by a free standing dye doped slab of a few millimetres thick to gain a better waveguide confinement due to the higher refractive index contrast between the active layer and air.

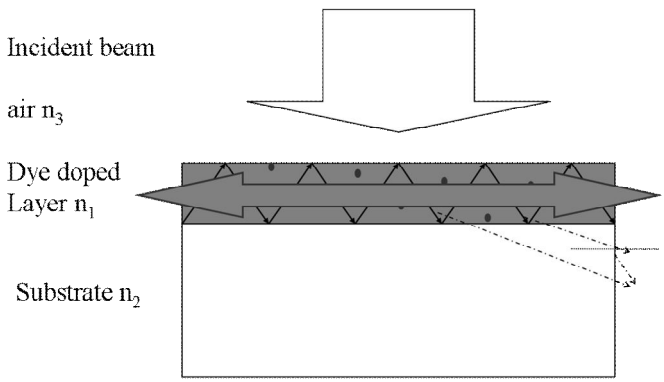

Figure 5.1. Sketch of the luminescent concentrator

In Figure 5.1, the ray optics suggests that to achieve TIR, the travelling angle of the light should be larger than the critical angle determined by the refractive indices of the matrix layer and the substrate. Equation 5-1 gives the fraction of the light can be guided by TIR [5]:

$$Q = \frac{1}{2}[\sqrt{1-(\frac{n_1}{n_2})^2} + \sqrt{1-(\frac{n_3}{n_2})^2}] \qquad \textbf{5-1}$$

n_1, n_2 and n_3 are refractive indices of the active layer, substrate and top layer respectively. For glass substrate and air, n_1 and n_3 are equal to 1.46 and 1.0. Besides the guided waves, when the light travels at a angle equal to the critical angle, a partial guiding effect occurs in the leaky waves (represented by the dotted arrows in Figure 5.1) These leaky waves propagate in a direction nearly parallel to the layer interface in a very thin region inside the substrate and can eventually be coupled out from the edge [8-9].

The light concentration ratio (LCR) of a LC, defined as the ratio of emission intensity from one edge to the incident beam excitation intensity, is very important for improving the power intensity of LED emissions. The LCs used here are slightly different from the conventional LCs for solar cells. Firstly, the size of the LC is much smaller than conventional LCs in order to match the size of the Lumiled K2 LED chip of 1.5 mm by 1.5 mm. Secondly, to have high LCR, the LC is specifically designed for improving the power intensity rather than harvesting power/energy in solar power modules. Hence, to achieve light concentration from a 1.5 mm by 1.5 mm excitation area, the film of the guiding layer (~μm) would be much thinner than solar LCs (~mm). The direct consequence of using a thin film is the redistribution of the waveguide and leaky modes through thin film interference effects [10] in the layer interface.

5.3. Experimental

The LC is formed by depositing a thin film on a quartz substrate. The edge of the coated film was carefully cut to get rid of the thick edge bead. The solution preparation and thin film deposition were mentioned in **Chapter 3**. The LC was excited by a CW He-Cd laser at 442 nm with a beam diameter of 1.5 mm to mimic the LED excitation used in **Chapter 4**. The edge emission profile from the concentrator was recorded by a beam profiler (Coherent. Inc) with a yellow filter to block the blue excitation. To evaluate the edge emission energy, a calibrated integrating sphere with a photodiode, as described in **Chapter 3** for PLQY measurements, was used to capture the highly divergent edge emission. In the energy measurement, to lower the impact of the surface emission from the concentrator, only the edge of the LC was inserted into the integrating sphere through an aperture of similar size as the concentrator edge. The edge emission energy was then converted from the photodiode reading. The resulting edge emission intensity can therefore be calculated via dividing the energy by the edge emission dimensions measured by the beam profiler.

For the loss measurement of the LC, a fibre coupled CCD spectrograph was used to collect the edge emission as the excitation moves away from the edge. In front of the fibre, a series of lenses was used to ensure that most of the light emitting from the edge was collected. The relative position of the film edge and the fibre was kept constant, as the excitation spot was moved away from the film edge in steps of 0.5 mm. The propagation loss coefficient can be obtained from the following equation:

$$I = I_0 \exp(-\alpha_{loss} d) \qquad \textbf{5-2}$$

I_0 is the edge intensity with excitation beam aligned at the edge; α_{loss} is the loss coefficient and d is the distance between the excitation and the film edge. To test the impact of LC for pumping polymer lasers, OPO with excitation at 450 nm was used as the pump source for both LC and polymer lasers. As described in **Chapter 3**, a fibre coupled CCD spectrograph was used to collect the output spectrum from the laser.

5.4. Selection of materials

5.4.1. Active organic dye

The dye molecules in the LC must absorb the excitation strongly and re-emit very efficiently at a wavelength that will be strongly absorbed by the gain medium of the polymer laser. This requires that the chosen dye have an absorption peak at 450 nm where the LXK2-PR14-Q00 LED emits. Two highly efficient green emitting coumarin dyes, coumarin 334 and coumarin 6, exhibit strong absorption at 450 nm in ethanol, as shown in Figure 5.2, making them suitable candidates for the LC.

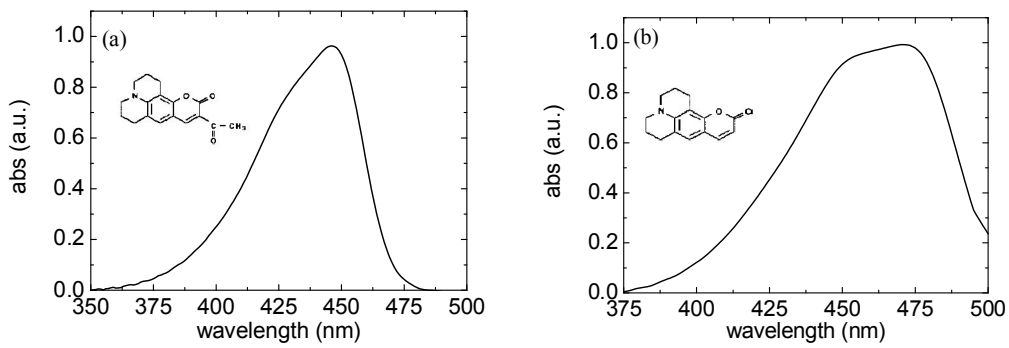

Figure 5.2. Absorption spectra of (a) coumarin 334 and (b)coumarin 6

5.4.2. Passive matrix material

One of the challenges for making a high performance LC is the choice of the passive matrix material. A good passive matrix can help to prevent aggregation quenching in concentrated dye molecules and give low waveguide and reabsorption losses, as the re-emitted light travels in the active layer towards the edge. Besides, based on equation 5-1, to have an efficient waveguide of high TIR, the refractive index of the active layer should be much higher than the substrate. In addition, the entire structure should be easy to fabricate, maintaining the simple fabrication feature of organic semiconductor lasers.

The first attempt is to use poly (methyl 2-methylpropenoate) (PMMA) as the passive matrix. It is a commonly used transparent thermoplastic material with refractive index of 1.49, higher than the silica substrate of 1.46. Hence, a waveguide can be formed between the dye doped PMMA layer and the underlying substrate. 200 mg/ml PMMA was dissolved with coumarin 334 (w.t.: 2%) in chloroform to make a film of 9.8 μm from spin coating. The blend has PLQY as high as 74.5%. Figure 5.3 shows the edge emission profile recorded by the beam profiler.

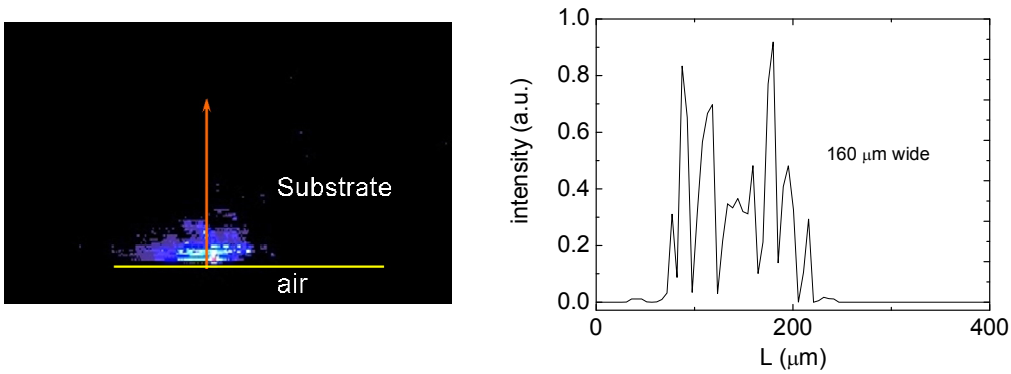

Figure 5.3. Edge emission profile from a dye doped PMMA:

(Left) image from beam profiler; (Right) cross section across the red line

In Figure 5.3, the left picture taken from the beam profile gives the cross section of the edge emission with air-polymer interface at the bottom. The intensity of the emission is represented by the colour with red being the strongest. It can be observed that most of the emission is concentrated at the air-polymer interface and gradually decreases into the glass substrate. The right graph plots the intensity distribution along the red line in the left picture. The edge emission is 160 μm wide. The irregular spikes could arise from the scatter centers in the poor quality edge. Compared to the 9.8 μm film thickness of the LC, the edge emission width is 16 times broader. Several reasons could contribute to the broad edge emission, for instance the TIR efficiency, waveguide confinement in the active layer, leaky waves and the thin film interference effect.

According to Equation 5-1, the low refractive index contrast between PMMA and silica resulted in a TIR efficiency of 47%. The weak waveguide effect could broaden the edge emission, since most of the emission would leak into the thick substrate. Figure 5.4 simulates the intensity distribution of the waveguide modes in the air-PMMA-substrate structure.

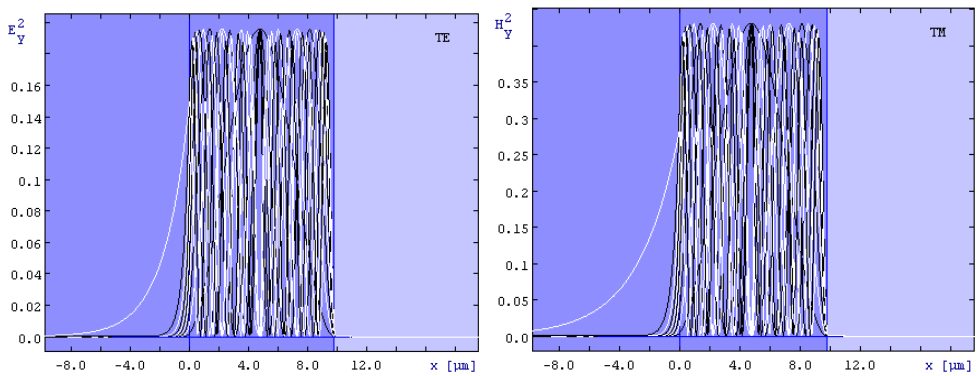

Figure 5.4. Intensity distribution of the TE(left) and TM (right) guided modes in the PMMA-glass waveguide (http://wwwhome.math.utwente.nl/~hammer/oms.html)

The simulation was performed based on Maxwell equations. The refractive index of each layer is represented by the background colour. From left to right, the layers are glass substrate, dye doped PMMA and air. The curves indicate different transverse modes guided in the dye doped PMMA layer. In the 9.8 μm dye doped PMMA layer, there are 18 transverse modes, including nine TE modes and nine TM modes. As can be seen, the small refractive index contrast between the substrate and the dye doped PMMA layer weakens the waveguide confinement of the transverse modes, especially for the higher order modes such as TE_9 and TM_9 modes. They have very long tail propagating into the substrate. Hence, in addition to the unguided modes, a fraction of the 47% guide modes can still leak into the substrate.

Moreover, thin film interference effect plays an important role on redistributing the emission intensity inside the waveguide layer and hence has an impact on how much of the emission would be coupled into the leaky waves. The emission coupled into the leaky waves (dotted lines in Figure 5.1) can broaden the edge emission through scattering in the PMMA-silica interface as it travels.

Broad edge emission tends to have a negative impact on the LCR which is inverse proportional to the edge emission beam width. The wider the edge emission, the lower the LCR is. The LCR measured from this specific 2% coumarin 334 doped PMMA is 15%, implying that with PLQY of 74%, the PMMA LC lost, rather than gained, 85% of the excitation intensity. To improve the LCR, the edge emission needs to be minimized. A different passive matrix material with better refractive index contrast to the silica substrate could be helpful for enhancing the waveguide effect.

SU-8 is a widely used epoxy-based negative photoresist and can be deposited by spin coating over a thickness ranging from 200 nm up to 2 mm. It is designed for patterning high aspect ratio (>20) structures [11-12]. Its molecular structure is shown in Figure 5.5.

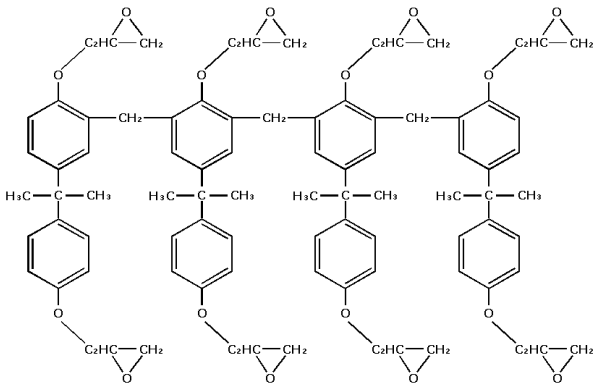

Figure 5.5. Molecular structure of photoresist SU8

It is highly transparent across the visible spectrum from 400 nm to 700 nm with refractive index of 1.63 at 450 nm, much higher than the refractive index of PMMA. The SU8 used was purchased from MicroChem in solvent form. Two different SU8 solutions with different viscosities of 2.49 cSt (SU8 2000.5) and 380 cSt (SU8 2010) were mixed with different ratios to change the film thickness. With coumarin 334 as the dopant, Figure 5.6 presents the edge emitting beam width from films varied from 4 μm to 11 μm, which corresponds to the SU8 solvent ratio of 2000.5 to 2010 increasing from 1:1 to 1:3. The spin coating speed for all the films was 3250 r.p.m..

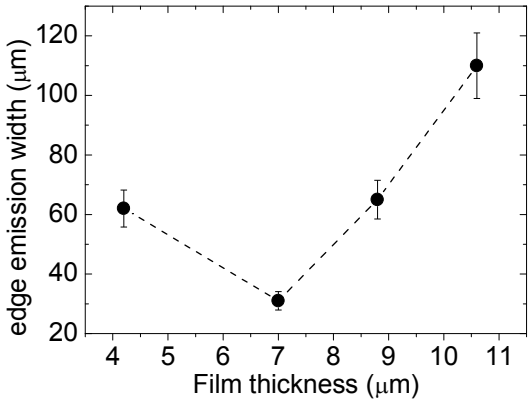

Figure 5.6. The dependence of the edge emission beam width on the film thickness for SU8

The narrowest emission can be achieved is 31 μm, when the film thickness is 7 μm. Further increase of the film thickness leaded to wider edge emission beam, which could be attributed to the increasing number of scattering centers in the film brought by the SU8 2010 solution. The mixing of the SU8 2000.5 and 2010 can effectively control the film thickness, but the quality of the spin coated film decreased with higher mixing ratio of SU8 2010 due to higher solution viscosity.

In comparison to the PMMA waveguide, the edge emission width was reduced by a factor of 5. The narrower edge emission could result from the stronger waveguide effect in the SU8-sillica waveguide, as shown in Figure 5.7. Inside the 7μm SU8 waveguide, 21 TE and 21 TM modes were supported. The decay of the transverse mode into the substrate is 4 times shorter than the PMMA waveguide in Figure 5.4. More importantly, the high refractive index of the SU8 increased the TIR efficiency to 62%, which reduced the energy leaking into the substrate.

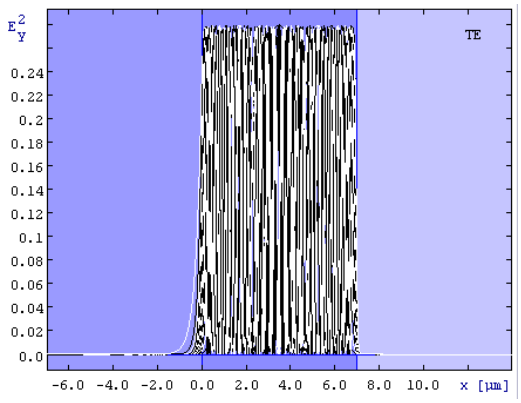

Figure 5.7. TE mode distribution in the 7 µm SU8 waveguide (http://wwwhome.math.utwente.nl/~hammer/oms.html)

5.4.3. Optimization of the LC

Having identified a film thickness giving narrow edge emission, the effect of the dye concentration on the LCR was investigated in this section. When doped in the photoresist SU8, the dye molecules should present high PLQY so that it can efficiently convert most of the incident excitation into emission. TIR could guide the emission towards the edge to pump a polymer laser. The normal treatments for SU8 in photo-patterning involves thin film deposition, soft pre-bake, exposure, post bake, developing and the final hard bake. However, these fabrication steps tend to have a negative impact on LCs. It has been observed that the exposure and subsequent baking steps lead to a reduction of 0.014 in refractive index, reducing the waveguide confinement and TIR [13]. More importantly, heating and UV exposure usually have a bad impact on the PLQY of organic materials.

To evaluate the impact of the normal fabrication process on LCs, two samples made from coumarin 334 doped SU8 were prepared. One was made without the normal treatments and left in a nitrogen atmosphere at room temperature to allow the remaining solvent to evaporate slowly, while the other was prepared with the photo-patterning full process. The film thickness of the two samples was

controlled at 7 μm. Figure 5.8 compares the absorption and PL spectra from these two samples.

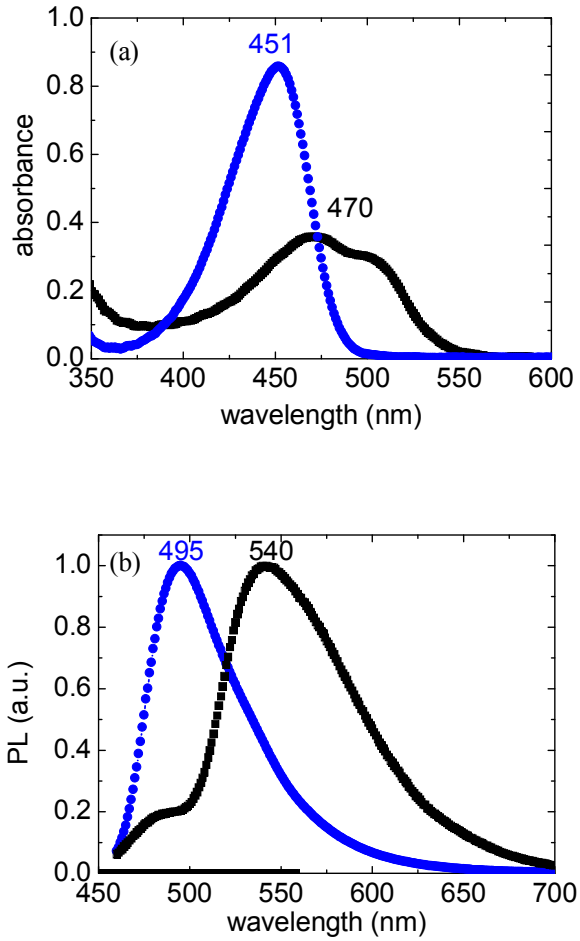

Figure 5.8. (a) Absorption and (b) PL spectra of the full processed sample (black) and the spin coated sample (blue)

The absorption spectrum of the full processed sample has a red shift of 20 nm, in comparison to the other one. The red shift pushes the absorption peak away from the LED emission peak. A similar red shift also occurs in the PL spectrum, moving the PL peak from 495 nm to 540 nm. Also, both absorption and emission spectra were broadened. The spectral broadening and red shift could be due to a solvatochromic effect from the photoacid. The UV exposure and developing cross-links the long SU8 molecular chains, forming a rigid network structure that

can change the polarity of the SU8. Therefore, the electronic states of the dye molecules in the cross-linked SU8 matrix could be different. Additionally, after UV exposure, developing and heating, the film absorbance was decreased by 58% and the PLQY dropped to 15%. All these negative effect makes the blend less attractive for LCs. Hence, to have high absorption and quantum efficiency, the dye doped SU8 layer will not be treated in conventional approaches.

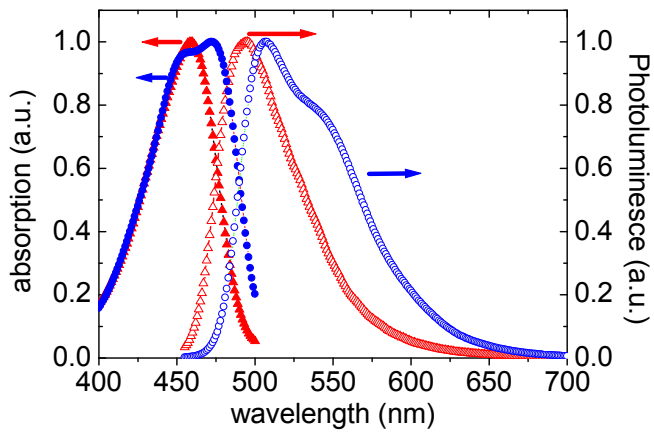

Figure 5.9. Absorption and PL spectra of coumarin 334 (red) and coumarin 6 (blue) doped SU8

Figure 5.9 shows the absorption and PL spectra of coumarin 334 and coumarin 6 doped SU8 blend without photo-patterning treatment. Both blends have absorption peaks close to 450 nm, matching well with the blue LED emission spectrum. Compared to the coumarin 334 doped SU8, the absorption and PL spectra of the coumarin 6 doped SU8 showed a 15 nm red shift.

To optimize the LCR, the concentration of the coumarin dyes needs adjustment, while the film thickness was kept at 7 μm. Generally, the increase of the dye concentration can improve the absorption due to the increasing number of dye molecules. However, the large number of dye molecules may lead to a reduction in the quantum efficiency by aggregation quenching, when they are packed together. Additionally, high concentration of dye molecules may introduce more

scattering centres into the waveguide to increase the waveguide losses. Also, the reabsorption loss could become severe at high dye concentration, as the light travels towards the edge, since the tail of the absorption spectrum extends to the PL spectrum.

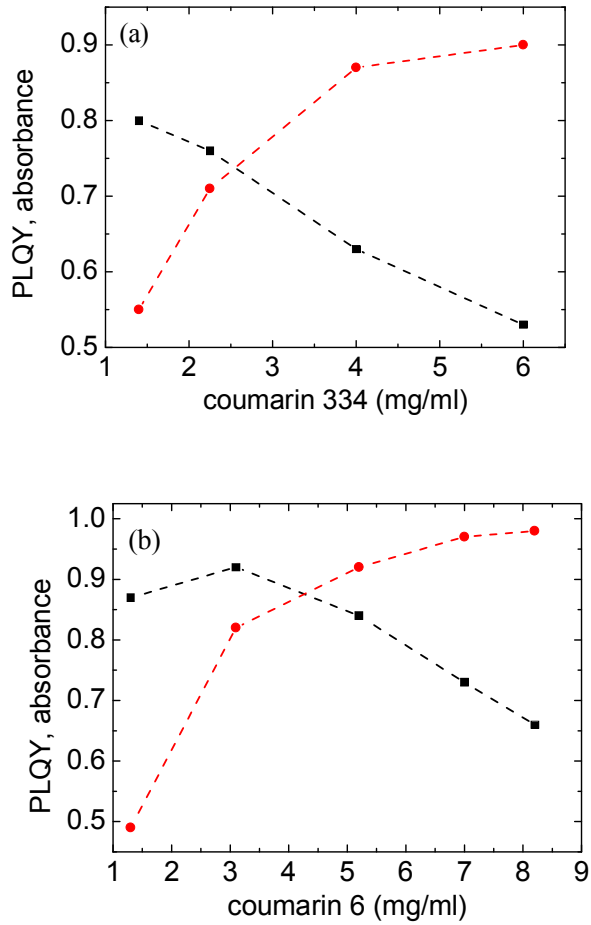

Figure 5.10. The influence of the dye concentration on PLQY (black square) and absorbance (red circle) for (a) coumarin 334 and (b) coumarin 6

In Figure 5.10, the PLQY and absorbance (at 450 nm) were measured for coumarin 334 and coumarin 6 blends at different dye concentrations. For coumarin 334 doped SU8, the increase of the dye concentration from 1.4 mg/ml to 6 mg/ml decreased the quantum efficiency from 80% to 53%, while the absorbance increased from 0.55 to 0.9. Similar trends occur to coumarin 6 doped

SU8. The highest PLQY of coumarin 6 doped SU8 is 92%, which is 12% higher than the coumarin 334 doped SU8.

The corresponding waveguide losses, including intrinsic waveguide loss and reabsorption loss, for these two blends at different dye concentration were plotted in Figure 5.11.

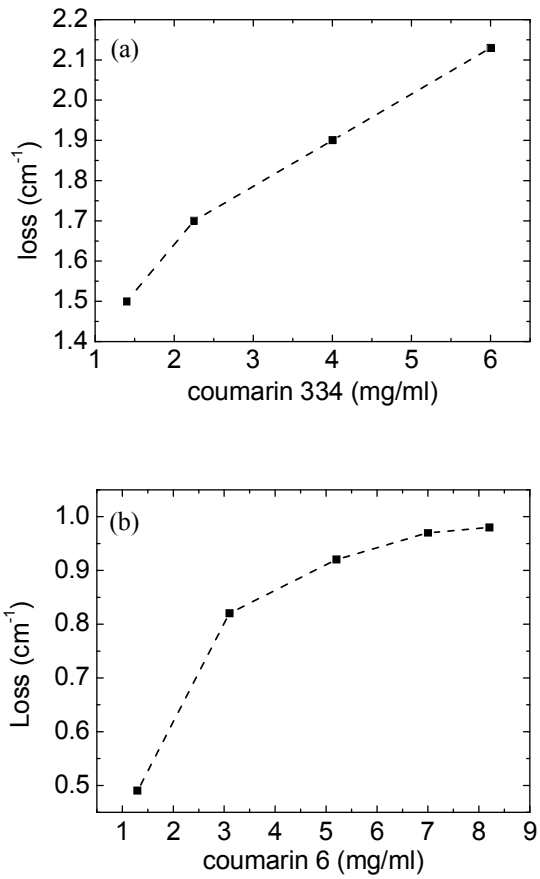

Figure 5.11. Waveguide losses of (a)coumarin 334 and (b)coumarin 6 doped SU8 waveguide for different dye concentrations

It is suggested that the increase of the dye concentration for both coumarin 334 and coumarin 6 increased the waveguide loss. For coumarin 334 doped SU8 waveguide, the loss increased from 1.5 cm^{-1} to 2.1 cm^{-1}. The coumarin 6 waveguide has lower losses, lying in the range between 0.46 cm^{-1} and 2 cm^{-1}. The

slightly higher waveguide loss from coumarin 334 doped SU8 could be attributed to the lower solubility of the dye which could form larger aggregates at high concentrations.

The measured LCR values for the coumarin 334 and coumarin 6 LCs were shown in Figure 5.12 with different dye concentrations. It reflects the total effect between the PLQY, absorbance and the waveguide losses discussed above.

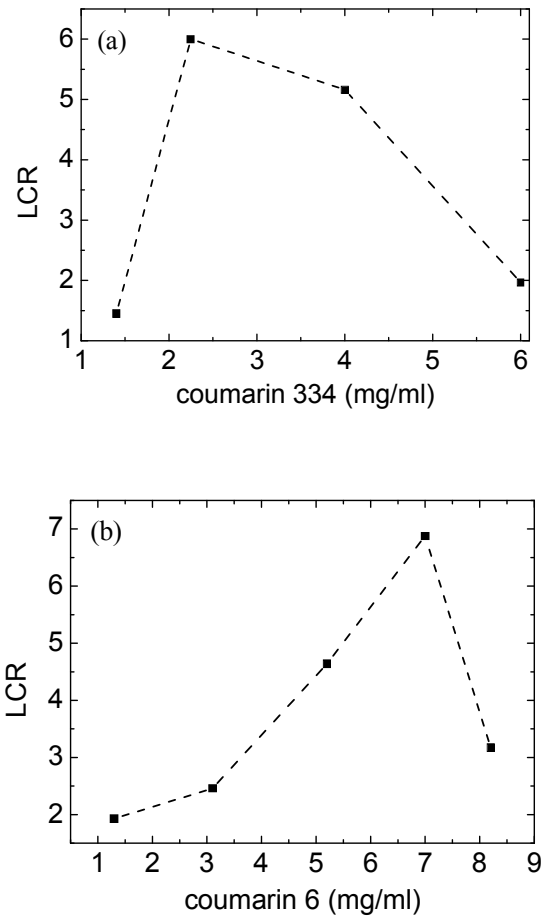

Figure 5.12. LCR for (a) coumairn 334 and (b)coumarin 6 doped SU8 LCs

From Figure 5.12, the increase of the coumarin dye concentration did not lead to a monotonic increasing in the LCR for both LCs, unlike the case in the absorbance or waveguide losses shown in Figure 5.10 and Figure 5.11. The highest LCR was achieved at a certain dye concentration, when all the effects in the active layer

were optimized. For coumarin 334, the highest LCR of 6 occurred at a concentration of 2.5 mg/ml. Coumarin 6 doped SU8 has a slightly higher LCR of 7.5, occurring at a higher concentration of 7.5 mg/ml due to its better solubility.

5.5. Theoretical simulation

To improve the understanding of the effect of coumarin dye concentration on the LCR, a model has been developed to simulate the LCs, based on the prior approaches on modelling such devices [14-17]. The flow chart in Figure 5.13 exhibits how the LC usually performs.

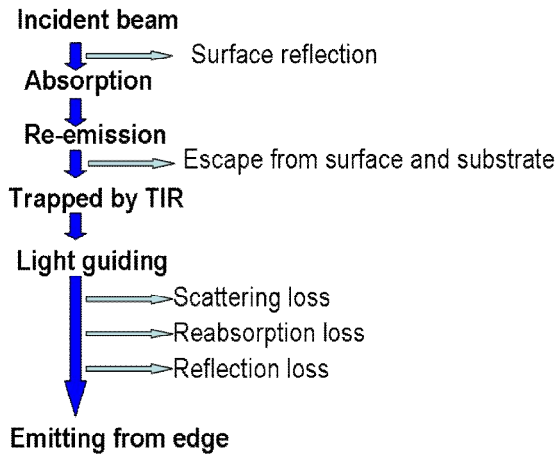

Figure 5.13. Flow chart of the LC performance

The light concentration ratio (LCR) C can be described as:

$$C = G \times \eta_{opt} = \frac{\sqrt{S}}{d}\eta_{opt} = \frac{\sqrt{S}}{d}\Phi_{ex}\Phi_{PL}\Phi_{trapped}\Phi_{abs} \qquad \textbf{5-3}$$

Where G is the geometrical gain that is proportional to the square root of the excitation area S and inverse proportional to the edge emission width d for a square shape LC. d can be measured experimentally by the beam profiler and S is taken to be 1.5 mm by 1.5 mm for the excitation used in the characterization. The

LCR is determined by both the optical efficiency (η_{opt}) in the waveguide layer and the geometry (G) that is related to the edge emission dimensions and the excitation area. The optical efficiency (η_{opt}) depends on various steps, including the excitation efficiency, absorbance, PL quantum efficiency and TIR.

Following the flow chart in Figure 5.13, when the pump beam is incident on the surface of the LC, a fraction of it would be reflected though Fresnel reflection, determined by the refractive index n_1 of the active layer. The absorbance of the film determines how much transmission can be absorbed by the dye molecules as it passes through the active layer. For normal incidence, the excitation efficiency (Φ_{ex}) of the pumped beam is:

$$\Phi_{ex} = [1-10^{-\alpha d}][1-(\frac{n_1-1}{n_1+1})^2] = \frac{4n_1(1-10^{-\alpha d})}{(n_1+1)^2} \qquad \textbf{5-4}$$

where α is the absorption coefficient at the pump wavelength. The absorbance can be measured experimentally from absorption experiments. By absorbing the excitation, the excited dye molecules re-emit the light as fluorescence with an efficiency determined by the PLQY (Φ_{PL}). The value of Φ_{PL} in the simulation was determined experimentally.

A fraction of the re-emission can be guided in the SU8 layer through TIR and travels towards the edge of the film:

$$\Phi_{trapped} = \frac{1}{2}[\sqrt{1-(\frac{n_1}{n_2})^2} + \sqrt{1-(\frac{n_3}{n_2})^2}] \qquad \textbf{5-5}$$

Equation 5-5 is the same as equation 5-1 with the use of a simple ray optics. In the simulation, the values for n_1, n_2 and n_3 were 1.62, 1.46 and 1 respectively for a dye doped SU8 layer in between a glass substrate and air.

The trapped emission experiences waveguide losses (Φ_{abs}) as it is guided towards the edge. Φ_{abs} consists of matrix and self-absorption loss from the dispersed dye molecules [18-19], assuming the reflection losses from each total internal reflections and the edges are negligible. The matrix loss depends on the absorbance of the matrix material at the wavelength of the re-emission. For SU8, the matrix absorption is fairly low, since SU8 is nearly transparent in the visible wavelength range. In terms of the self-absorption loss, the spectral overlap between the absorption and PL spectra indicates a fraction of the dye emission would be absorbed by the molecules over a sufficient long propagation length. The self-absorption increases as the travelling path of the emission increases. It mainly affects the short wavelength region of the PL spectrum where the spectral overlap is the largest. Owing to the self-absorption loss, the edge emission spectrum will normally be red shifted compared to the PL spectrum. The re-absorbed light has the chance to be re-emitted and waveguided again in the dye layer, governed by the PLQY and TIR. Therefore the dye emission may undergo several generations of reabsorption and re-emission, as travelling to the edge. It has been suggested that the attenuation of the first generation of emitted photons from the reabsorption process would be sufficient for simulating the self-absorption process [19]. Therefore, Φ_{abs} can be represented by the product of the matrix loss and the re-absorption loss [15]:

$$\Phi_{abs} = \Phi_{waveguide}\Phi_{reabsorption} = 10^{-\varepsilon_m \gamma \beta \sqrt{S}} \times K \times 10^{-\varepsilon_d \gamma \beta \sqrt{S}} \qquad \textbf{5-6}$$

In equation 5-6, ε_m and ε_d are the absorption coefficients of the matrix and dye at the emission wavelength, γ is a constant that takes into account the reflection from each edge of the LC. ε_m, ε_d, γ together with the product of β and the square root of the absorbing surface $\sqrt{S}$ determines the mean optical path length of the beam travels inside the LC before it emits from the edge. For a square substrate, the value for γ is 3.52 [15]. β can be calculated from

$$\beta = \sqrt{\frac{1}{\frac{m}{2}\sin(\frac{2\pi}{m})}} \qquad \textbf{5-7}$$

where m is the number of edges in the substrate of the LC [15]. For a square substrate, $m = 4$, which implies $\beta = \frac{\sqrt{2}}{2}$.

In equation 5-6, K is a constant related to the first generation of the reabsorption. Both K and the absorption coefficients (ε_m and ε_d) can be deduced from the edge emission spectra, when the excitation spot is moved away from the film edge by l:

$$\Phi_{abs}(l) = \Phi_{waveguide}\Phi_{reabsorption} = 10^{-\varepsilon_m l} \times K \times 10^{-\varepsilon_d l} = K \times 10^{-(\varepsilon_m + \varepsilon_d)l} \qquad \textbf{5-8}$$

Experimentally, $\Phi_{abs}(l)$ can be measured as the ratio of the edge emission band area with a given l to the emission band area obtained from front surface excitation.

Taking the LC made of 7mg/ml coumarin 6 doped in SU8 as an example, Figure 5.14 plots the change of the edge emitting spectra, when the pump spot was moved away from the edge.

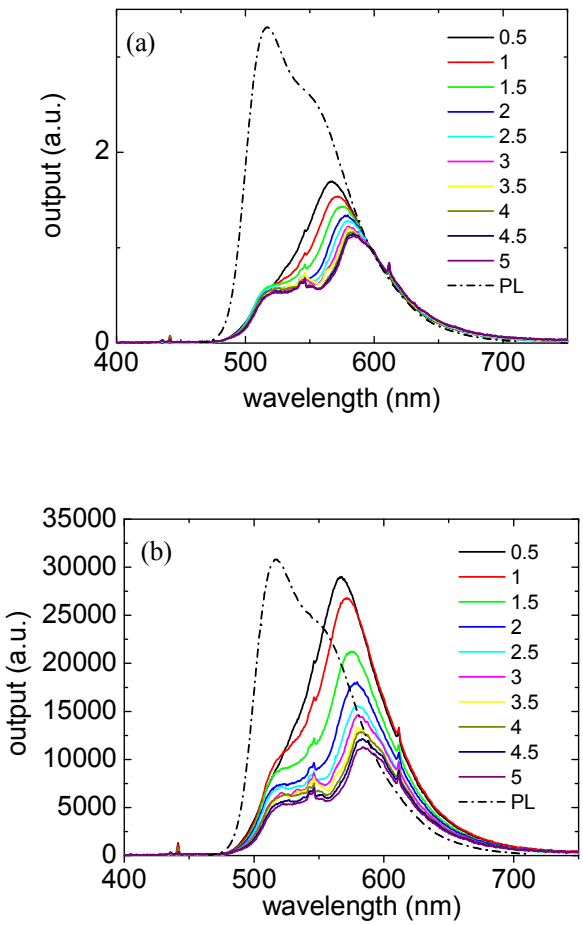

Figure 5.14. Edge emission spectra at different pump beam position: (a) normalized at 597 nm; (b) non-normalized. *l* is indicated in the labels

The spectra in graph (a) were normalized at 597 nm to give a clear illustration of the red shifting, as the distance between the pump spot and the film edge increased from 0.5 mm to 5 mm. In comparison to the PL spectrum (the dotted curve), the 0-0 vibronic peaks in the edge emission spectra were much weaker than the 0-1 vibronic peaks due to the strong self-absorption. To extract *K* and the absorption coefficients (ε_m and ε_d), according to equation 5-8, $\Phi_{abs}(l)$ the ratios between the edge emission band area and the PL band area were calculated from Figure 5.14 (b) for different *l* and is plotted in Figure 5.15.

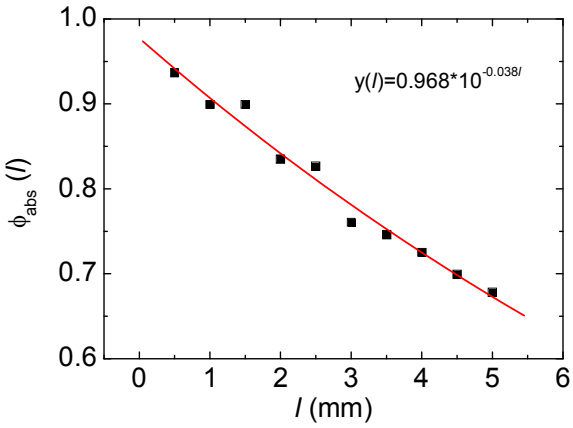

Figure 5.15. $\Phi_{abs}(l)$ (black squares) obtained from Figure 5.14 with fitting curve (red line)

$\Phi_{abs}(l)$ decreased gradually as the pump spot was moved away from the edge. The data points can be well fit by the $\log_{10}$ function (red curve) with the equation:

$$\Phi_{abs}(l) = 0.968 \times 10^{-0.038l} \quad \textbf{5-9}$$

By comparing equation 5-8 and equation 5-9, K and ($\varepsilon_m + \varepsilon_d$) can be deduced to be 0.968 and 0.38 cm^{-1} respectively.

By knowing the values of K and ($\varepsilon_m + \varepsilon_d$), the theoretical LCR value *C* can be calculated from equation 5-3. The input parameters are excitation efficiency (Φ_{ex}) calculated from equation 5-4 by using 0.97 as the measured absorbance, measured PLQY of 0.73, $\Phi_{trapped}$ of 62% obtained from equation 5-4, and Φ_{abs} calculated by using K and ($\varepsilon_m + \varepsilon_d$) extracted from equation 5-8. The theoretical LCR value is calculated to be 9.9, which is close to the experimental measured LCR of 7.5.

Following the same approaches, the theoretical LCR values for different coumarin 6 and coumarin 334 LCs measured in Figure 5.12 can be obtained. The simulated and measured LCRs are plotted in Figure 5.16 for comparison.

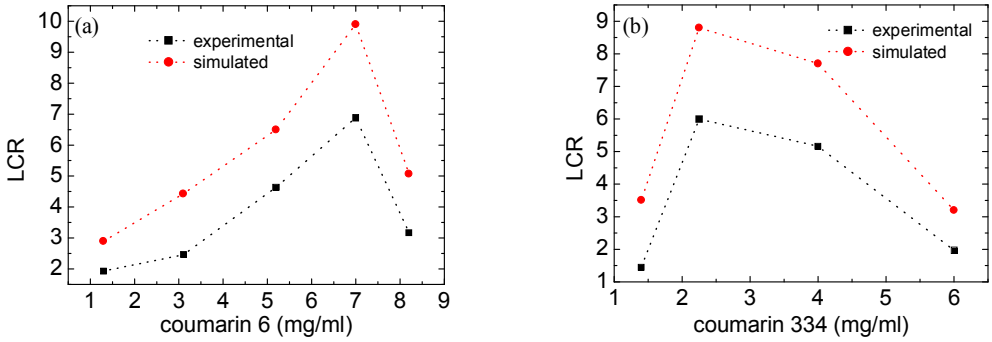

Figure 5.16. Simulated (red) and measured (black) LCRs for (a) coumarin 6 and (b) coumarin 334 LCs

The simulation successfully predicted the dependence of the LCR on the coumarin dye concentration in SU8 for both LCs. The absolute LCR values, however, were larger than the experimental results. This could be understood to arise from the difference of the substrate size used in the experiments and in the simulation. The substrate used in the simulation was restricted to the pump beam size of 1.5 mm by 1.5 mm, meaning that the whole front surface of the concentrator acts as an absorption surface so that the whole concentrator was excited to give emission. In contrast, the substrate used in the experiment (~10 mm by 10 mm) was larger than the pump beam. Consequently, the surface was partially excited. Without lateral confinements, the emission in the waveguide could experience additional in-plane lateral losses in the unpumped region, leading to lower LCR values. Therefore, the simulation indicates the LCR value could be further improved, if lateral confinements or smaller substrates are used.

5.6. Further improvement of LCR

It is not straightforward to introduce lateral confinement on a spin coated film. Alternatively, a smaller substrate was used in this section with the aim of further increasing the LCR. To have a smaller substrate, the sample was cut after spin coating to remove the unwanted parts and poor quality thick edges. For the coumarin 334 LC with the highest LCR in Figure 5.16, when the substrate dimensions were reduced from 10 mm to 3.5 mm, the LCR was successfully increased from 6 to 8.2, getting close to the simulated value of 9. Similarly, for the coumarin 6 LC, the highest LCR can be improved from 7 to 8.8.

Besides lateral losses, another factor limiting the LCR is the waveguide losses. In Figure 5.11, the losses measured for both coumarin 334 and coumarin 6 doped SU8 are in the range between 0.5 cm^{-1} and 2 cm^{-1}. At the optimized coumarin dye concentrations, the waveguide losses for coumarin 334 and coumarin 6 doped SU8 are 1.7 cm^{-1} and 1.1 cm^{-1}, higher than the intrinsic SU8 waveguide loss of 0.4 cm^{-1} [20]. The high waveguide loss could be caused by the reabsorption and scattering from the coumarin dye molecules in the SU8 matrix. Low waveguide loss, especially low reabosrption waveguide loss, is critical for the further improvement of the LCR. However, it is not straightforward to reduce the waveguide losses, while maintaining the LCR. Reducing the dye concentration could lead to a lower waveguide loss. However, it also changed the LCR as shown previously. To solve the problem, an additional layer could be introduced in between the substrate and dye doped SU8 layer. Preferably, this layer should be transparent and refractive index matched to the dye doped SU8 layer. Hence, a fraction of the emission can be coupled into this layer absent of dye molecules and waveguided to the edge without reabsorption loss.

The material selected for the transparent layer is NORLAND UV curable adhesive NOR 68 with refractive index of 1.56. It was spin coated onto the substrate at 4000 r.p.m, followed by a five-minute exposure under a UV lamp at 360 nm. Compared to the SU8 layer with refractive index of 1.68, the low refractive index of the NORLAND adhesive is not ideal. However, it does have a high transparency in the visible spectral range. Figure 5.17 shows the TE mode distributions in this three layer waveguide structure for a 2 μm thick NORLAND layer.

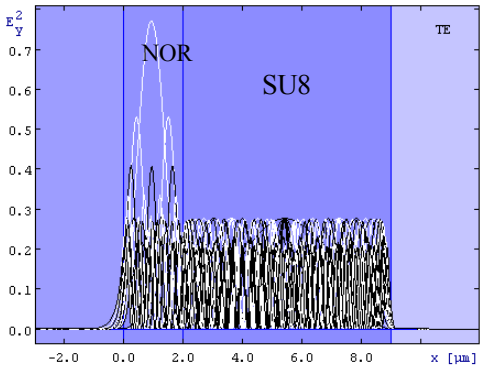

Figure 5.17. TE mode distribution in the three layer waveguide (http://wwwhome.math.utwente.nl/~hammer/oms.html)

From Figure 5.17, part of the guided modes can be guided into the NORLAND layer without significantly increasing the decay depth into the substrate. The same occurs for the TM modes. The edge emission was measured to be 30 μm, barely influenced by the additional NORLAND layer.

Figure 5.18 plots the dependence of the edge emission intensity on the pump beam position in logarithmic scale for both dye doped SU8 films at the optimized dye concentration obtained from Figure 5.16. The loss coefficients deduced from the red fitting curves for coumarin 334 and coumarin 6 were 0.5 cm^{-1} and 0.4 cm^{-1} respectively.

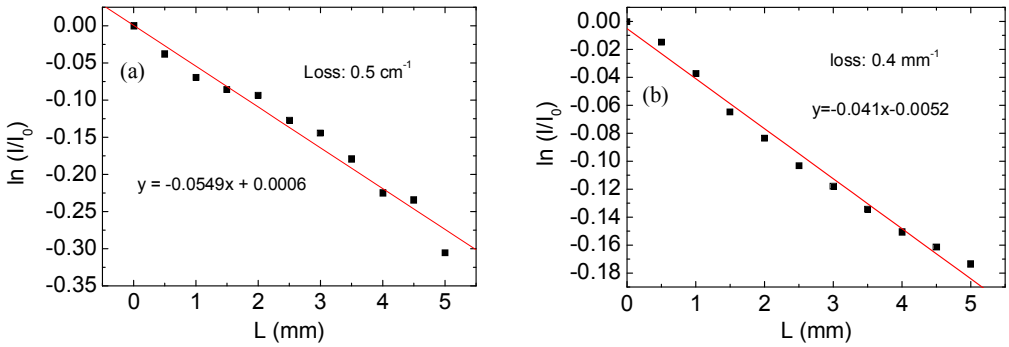

Figure 5.18. Loss coefficients for coumarin 334 at (a) 2.25 mg/ml and (b) coumarin 6 at 3 mg/ml doped SU8. (Black square): experimental data; (red line): fitting curve

In comparison to the loss in Figure 5.11, the loss coefficient of the coumarin 334 LC with the additional transparent layer was reduced by a factor 3.4. The corresponding reduction for coumarin 6 was 2.5. The larger reduction in coumarin 334 LC could arise from the more scattering centres in the previous coumarin 334 waveguide due to the poorer solubility of the dye in SU8. The reduction of the reabsorption loss can also be observed in the edge emission spectrum. In Figure 5.19, the spectra were normalized at 609 nm to give a better comparison.

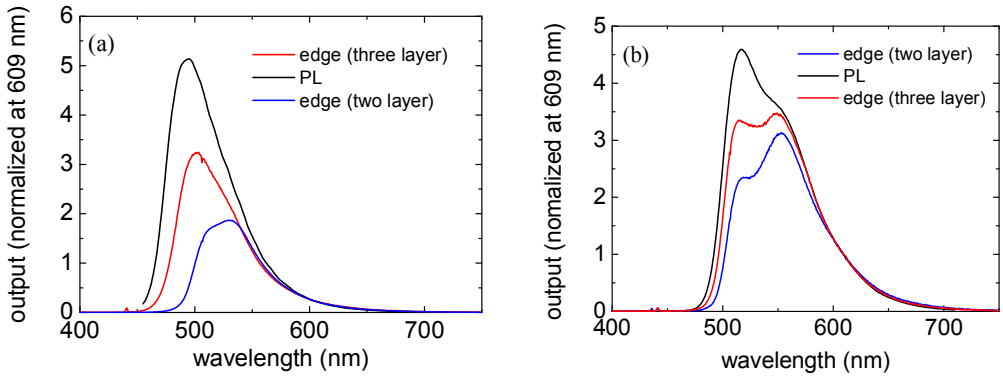

Figure 5.19. Comparison of the edge emission spectra for two layer and three layer waveguides of (a) coumarin 334 and (b) coumarin 6 doped SU8

Although the edge emission spectra for both LCs still have a red shift compared to the PL spectra, the degree of red shift were reduced. Take the coumarin 6 doped SU8 as an example. In Figure 5.19 (b), the strong self-absorption loss in the two-layer waveguide makes the 0-0 vibronic peak weaker than the 0-1vibronic peak in the edge emission spectrum. The three-layer LC, nevertheless, has equally strong 0-0 and the 0-1 vibronic peaks due to the reduced absorption loss. In terms of the edge emission intensities, represented by the area under the spectra, the three-layer waveguide give stronger output than the two-layer structure.

By combing the use of the three-layer waveguide with a 3.5 mm by 3.5 mm substrate, the highest LCR of coumarin 334 LC can be further increased to 9.5, 1.7 times higher than the value obtained in Figure 5.12. For coumarin 6, the highest LCR can be improved from 8.8 to 9.8. The more modest improvement in the coumarin 6 LC than that in the coumarin 334 LC could arise from the smaller reduction in the waveguide losses with the three-layer waveguide as discussed previously.

5.7. Organic laser gain medium

Both coumarin 334 and coumarin 6 LCs emit in the green region around 500 nm. In order not to waste the LCR of the concentrators, the polymer laser gain medium should have an absorption spectrum matching the edge emission spectrum of the LCs. With absorption peak at 495 nm, MEH-PPV is a good candidate for the laser gain medium. Figure 5.20 shows the absorption spectrum of MEH-PPV for a 150 nm thick film, the PL and the edge emission spectra of the two coumarin dye doped LCs.

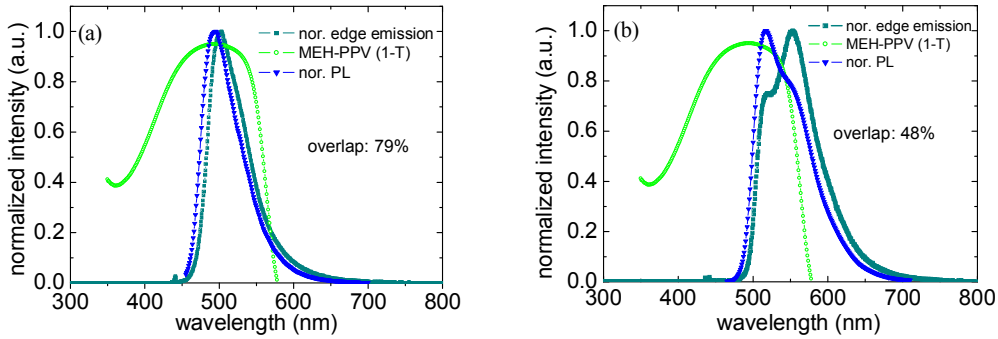

Figure 5.20. Spectral overlap between MEH-PPV and (a) coumarin 334 and (b) coumarin 6

In Figure 5.20, the absorption spectrum of MEH-PPV is plotted as the absorption fraction of the incidence beam which is defined as:

$$abs(\lambda) = 1 - 10^{-\alpha(\lambda)} \qquad \textbf{5-10}$$

α is the wavelength dependent absorbance measured for a 150 nm thick MEH-PPV film. The PL and edge emission spectra of the LCs were normalized to their peaks. The spectral overlap η equals to the fraction of the edge emission from the LCs that can be absorbed by the MEH-PPV film, as described in equation 5-11:

$$\eta = \frac{\int [MEH - PPV_abs(\lambda) \times LC_edge(\lambda)] d\lambda}{\int LC_edge(\lambda) d\lambda} \quad \textbf{5-11}$$

MEH-PPV_abs is the absorption fraction calculated from equation 5-10 and LC_edge is the normalized edge emission spectrum of the LCs. As discussed in the previous sections, in comparison to the PL spectrum, the reabsorption loss red shifted the edge emission spectrum, pushes the edge emission peak away from the absorption peak of MEH-PPV. This would reduce the spectral overlap and hence lower the absorption efficiency of the LC emission. Therefore, the effective LCR used as the pump beam will be lower than the highest LCR value obtained in the previous sections. Based on equation 5-11, MEH-PPV can only absorb 48% of the edge emission from the coumarin 6 LC. The slight blue shift of the coumarin 334 emission increased the MEH-PPV absorption to 79%. Consequently, coumarin 334 LC was chosen to subsequently pump the MEH-PPV lasers in the following sections.

5.8. Impact of pump geometries on lasing threshold

150 nm MEH-PPV was spin coated on a 400 nm period corrugated substrate to make surface emitting 1D and 2D DFB surface emitting lasers, according to the Bragg equation [21]. In the application of LCs for pumping polymer lasers, it is important to note that the LC transforms the pump beam shape from a circular spot (1.5 mm in diameter) to a narrow stripe (30 μm by 1.5 mm). As a preliminary experiment, the effect of the pump beam shape on the lasing threshold intensity for 1D and 2D DFB MEH-PPV lasers was explored.

Figure 5.21 indicates the relationship between the lasing threshold and the pump beam size for 1D and 2D DFB lasers. The width of the pump beam changed from 30 μm to 1.5 mm, while the length was kept constant at 1.5 mm. It means the

shape of the pump beam changed from a narrow stripe, which was the same as the LC edge emission profile, to a circular spot similar to the LED chip.

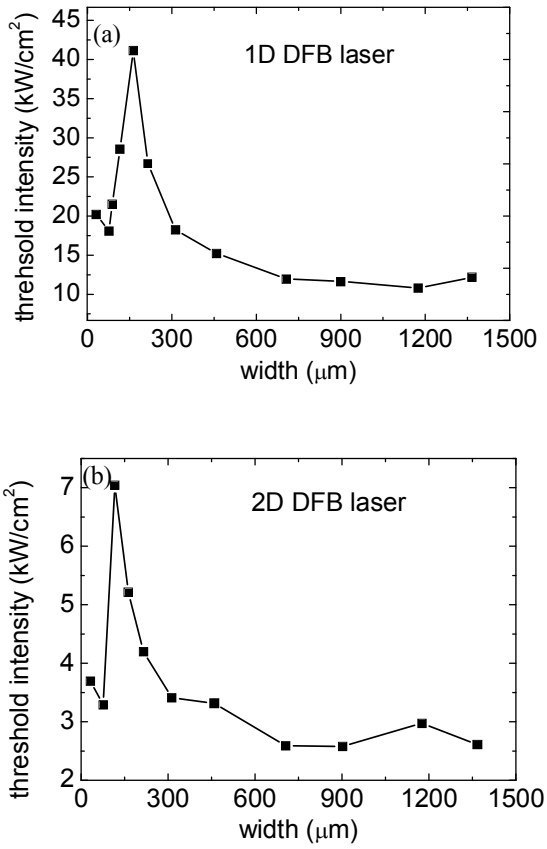

Figure 5.21. The change of the relative threshold intensity on the pump beam width for (a)1D and (b) 2D DFB MEH-PPV lasers

For both 1D and 2D DFB lasers, the relative threshold intensity increased smoothly as the pump stripe width changed from 30 μm to about 120 μm where a sharp peak formed, followed by a drop and gradual flattening tail with stripe wider than 1 mm. The threshold densities were increased by a factor of 1.4 and 1.8 for 2D and 1D DFB lasers respectively, when the width of the stripe was increased from 30μm to 1.5 mm.

The origin of the peak appearing in Figure 5.21 is not clear. It is possible that it arises due to a misalignment effect as the substrate was moved along the pump beam axis. Alternatively, it could be due to the change of the feedback strength inside the DFB resonators as the shape of the pump beam changed. For example, in the 2D DFB cavity, when the pump beam is narrow, for instance 30 μm, the excitation is in the shape of a stripe and thus only the gratings with grooves perpendicular to the stripe act as a resonator to provide feedback. It functions more like a 1D DFB resonator. As the width increases, light propagating perpendicular to the stripe sees significant gain and the gratings with grooves parallel to the stripe start giving feedback. The asymmetry of the stripe shape results in different lasing thresholds along the two feedback directions. Hence, while lasing is achieved in one feedback direction, light in the other feedback direction still experiences spontaneous emission, which makes the overall lasing threshold higher than the case excited by a symmetrical circular pump beam. As the width continuously increases and approaches the length of the stripe, the pump beam becomes more and more symmetric and the threshold intensity starts reducing and finally gets saturated. The situation is different in the 1D DFB resonator case. In 1D DFB lasers, feedback is only provided in the direction perpendicular to the grating grooves. The change in the lasing threshold intensity could depend on both the emission in the feedback direction and along the grating grooves. The broadening of the stripe gives emission along the grating grooves which can not experience optical feedback so that the threshold intensity starts increasing. In an ideal case, the threshold intensity is expected to increase continuously for wider and wider stripes. However, as the light travels along the feedback direction, it might be scattered due to defects in the material or gratings. It could be possible that the narrower the excitation area, the higher the possibility of the light to be scattered out of the excitation region and thus higher losses. On the contrary, for a wide pumping stripe, the scattered beam might still travel inside

the excited region, even thought it is deflected from the length of the stripe. A low lasing threshold intensity could occur when these two effects compromise.

The threshold intensity not only depends on the pump beam geometry but also on the alignment between the pump stripe and the grating grooves. Details are show in Figure 5.22.

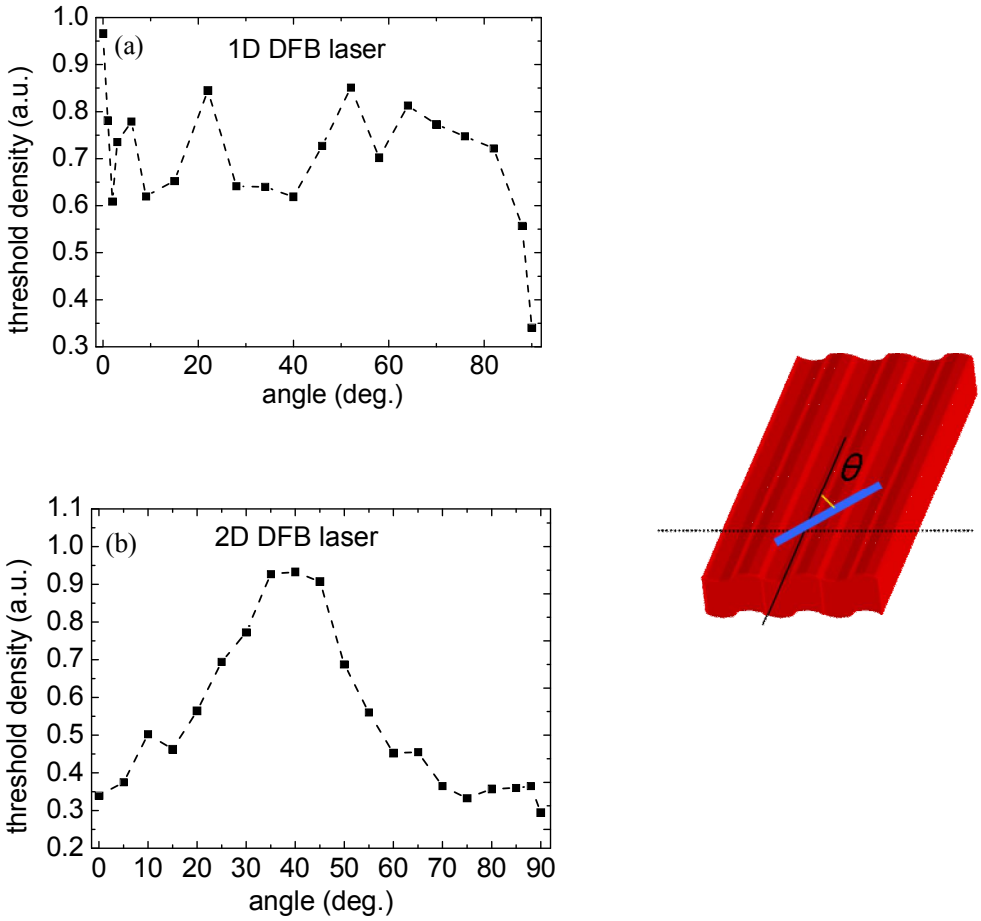

Figure 5.22. Threshold intensity change over alignment angles for (a) 1D and (b) 2D DFB lasers

The alignment angle plotted for the 1D DFB laser is indicated in the right graph in Figure 5.22. θ is the angle between the pump stripe (the blue line) and the grating grooves. It also applies for the 2D DFB lasers. The lasing threshold of 1D DFB

laser was very sensitive to misalignment, with a 2.5 times increase within a 5 degree deviation from the perfect alignment. For the 2D case, the alignment was less sensitive – a 45 degree misalignment was required to cause the same amount of change in threshold. Therefore, to ensure a low lasing threshold intensity, the edge of the LC should be alignment carefully for both 1D and 2D DFB lasers.

5.9. Effective Light Concentration Ratio (ELCR)

As discussed in **Section 5.7** and **Section 5.8**, the pump beam has an impact on the lasing thresholds. Also, not all the edge emission from the LC can be used to pump the laser due to the non-complete spectral overlap between the LC and the MEH-PPV. Hence, a concept of effective light concentration ratio (ELCR) can be introduced to help describe the behaviour of the LC as the pump source for polymer lasers. ELCR is defined as:

$$\mu_{ELCR} = \mu_{LCR}\Phi_{shape}\Phi_{gain}\Phi_{alignment} \qquad \textbf{5-12}$$

μ_{ELCR} describes the maximum reduction factor of the lasing threshold with the use of the LC; μ_{LCR} is the absolute LCR; Φ_{pump}, Φ_{gain} and $\Phi_{alignment}$ are the threshold change due to the pump beam geometry, gain medium absorption and alignment respectively.

By assuming the alignment between the grating and the concentrator edge is perfect, $\Phi_{alignment}$ can approach 100%.Φ_{gain} equals to 79% as discussed in **Section 5.7**. Φ_{pump} is 60% and 70% for 1D and 2D DFB lasers from Figure 5.22. Hence, μ_{ELCR} was calculated to be 4.2 for 1D DFB laser and 5.3 for 2D DFB lasers.

5.10. Concentrator pumped polymer laser

The coumarin 334 LC was excited by a circular spot at 450 nm wavelength (1.5 mm in diameter) by OPO, resembling the pumping condition of the GaN LED. The LC was placed in front of the the 1D and 2D DFB MEH-PPV lasers to study its impact on the threshold intensity. Figure 5.23 shows details of the pumping setup.

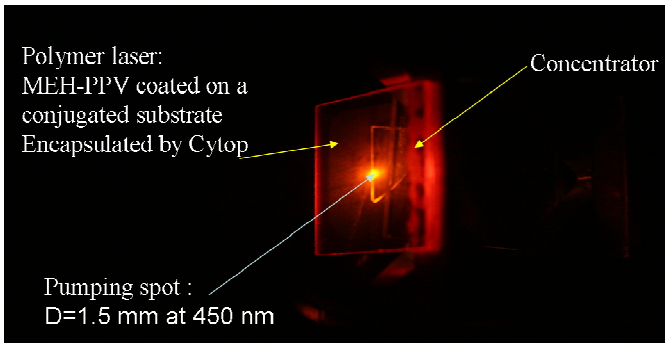

Figure 5.23. Pumping setup for LC pumped polymer laser

The edge of the concentrator was brought into contact with the surface of the polymer laser to prevent further broadening of the stripe emission from the edge of the LC, since the edge emission is very divergent. A layer of CYTOP was coated on the MEH-PPV layer to slow down the degradation and prevent potential scratching by the edge of the LC. The pump spot was aligned on the surface of the LC as close as possible to the edge of the LC to reduce potential waveguide losses.

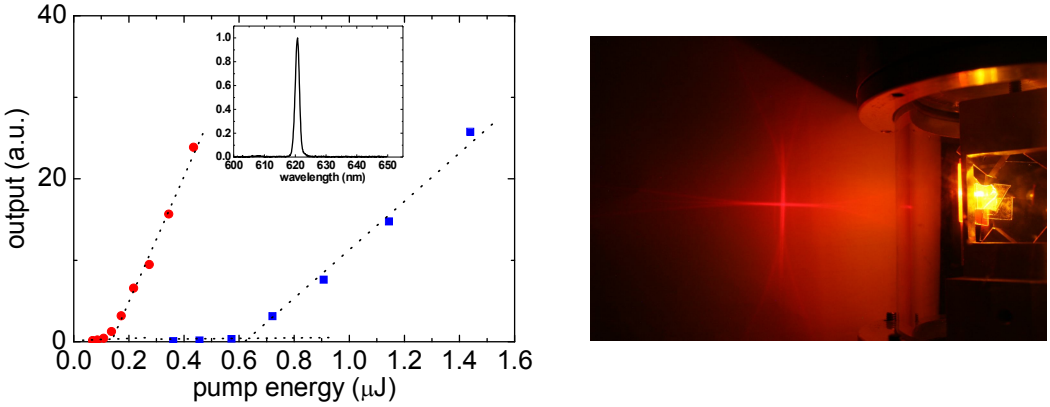

Figure 5.24. Lasing characteristics for 2D DFB laser: (left) threshold comparison between direct OPO pumping (square) and LC pumping (circle); (right) lasing picture.

Figure 5.24 shows the results for the 2D DFB laser. For direct pumping with a circular spot at 450 nm, the threshold energy was 610 nJ per /pulse (5.3 kW/cm^2). With the LC, the threshold intensity was reduced by 4.8 times to 1.1 kW/cm^2. The laser lased at 620 nm, close to the ASE peak. The picture, taken with a blue filter, shows an in-situ LC pumped MEH-PPV laser. The red-cross pattern of the emission confirms the polymer laser was pumped well above lasing threshold with the concentrator.

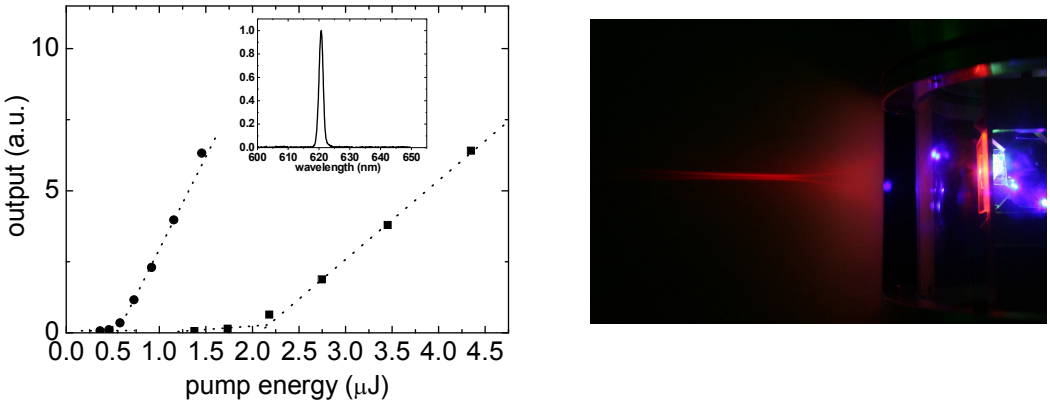

Figure 5.25. Lasing characteristics for 1D DFB laser: (left) threshold comparison between direct OPO pumping (square) and LC pumping (circle); (right) lasing picture.

For the 1D DFB laser in Figure 5.25, the LC reduced the threshold intensity from 19 kW/cm^2 to 4.4 kW/cm^2. i.e. by a factor 4.5. A double lobe lasing pattern can be observed in the picture, consistent with the fact that feedback was provided in only one dimension in the film [22]. The slightly lower threshold in the 2D DFB laser is due to the stronger feedback. For both 1D and 2D DFB lasers, the reductions in threshold pump intensity are in good agreement with the theoretical μ_{ELCR}.

5.11. Conclusion

In this chapter, suitable luminescent concentrators were developed for pumping organic semiconductor lasers with the aim to improve the performance of the LED pumped polymer laser. Two coumarin dye doped SU8 LCs were investigated and optimised to give LCR as high as 9.5 (coumarin 334) and 9.8 (coumarin 6). A simple theoretical model was developed to simulate the LCR for these two LCs. The theoretical model can successfully predict the change of the LCR at different coumarin dye concentrations, while the exact calculated LCR values were higher than the experimental results. The coumarin 334 LC was selected to pump the MEH-PPV laser, since there is better spectral overlap between the LC edge emission spectrum and the MEH-PPV absorption spectrum. With the coumarin 334 LC in between the polymer laser and the pump beam, the excitation densities required to reach thresholds in both 1D and 2D DFB polymer lasers were reduced by a factor of 4.5. The threshold reductions agreed well with the effective light concentration ratio which takes into account of the impact of the pump beam profile. MEH-PPV was chosen to be gain medium because of its absorption spectrum rather than its low threshold in polymer lasers. If better gain medium with matched absorption spectrum is used, the LC with high LCR and the capability of reducing lasing thresholds presents a promising technology for the

future developments in LED pumped polymer lasers.

5.12. Reference

[1] A. Garcia-Botella, A.A. Fernandez-Balbuena, D. Vazquez, E. Bernabeu, and A. Gonzalez-Cano, *Applied Optics*, 2009. **48**(4): p. 712.

[2] A. Garcia-Botella, A.A. Fernandez-Balbuena, D. Vazquez, and E. Bernabeu, *Solar Energy*, 2009. **83**(1): p. 113.

[3] Y.T. Chen, Y. Zhang, S. Hu, H. Tso-Hsiu, B.H. Lim, C.S. Lim, K.K. Chong, and B.K. Tan, *Communications in Theoretical Physics*, 2009. **52**(4): p. 750.

[4] I.M. Bassett, W.T. Welford, and R. Winston, *Progress in Optics*, 1989. **27**: p. 163.

[5] S.A. Evenson and A.H. Rawicz, *Applied Optics*, 1995. **34**(31): p. 7231.

[6] M.J. Currie, J.K. Mapel, T.D. Heidel, S. Goffri, and M.A. Baldo, *Science*, 2008. **321**(5886): p. 226.

[7] S.T. Bailey, G.E. Lokey, M.S. Hanes, J.D.M. Shearer, J.B. McLafferty, G.T. Beaumont, T.T. Baseler, J.M. Layhue, D.R. Broussard, Y.-Z. Zhang, and B.P. Wittmershaus, *Solar Energy Materials and Solar Cells*, 2007. **91**(1): p. 67.

[8] D. Yokoyama, M. Moriwake, and C. Adachi, *Journal of Applied Physics*, 2008. **103**(12).

[9] Y. Tian, Z.Q. Gan, Z.Q. Zhou, D.W. Lynch, J. Shinar, J.H. Kang, and Q.H. Park, *Applied Physics Letters*, 2007. **91**(14).

[10] J.H. Schmid, A. Delage, J. Lapointe, B. Lamontagne, S. Janz, P. Cheben, A. Densmore, D.X. Xu, and K.P. Yap. *Thin-film interference effect in scattering loss of high-index-contrast planar waveguides*. in *IEEE Lasers and Electro-Optics Society, 2008. LEOS 2008. 21st Annual Meeting of the*. 2008.

[11] A. del Campo and C. Greiner, *Journal of Micromechanics and Microengineering*, 2007. **17**(6): p. R81.

[12] P. Abgrall, V. Conedera, H. Camon, A.M. Gue, and N.T. Nguyen, *Electrophoresis*,

2007. **28**(24): p. 4539.

[13] F.M. Bain, A.E. Vasdekis, and G.A. Turnbull. *Holographic recording of sub-micron period gratings and photonic crystals in the photoresist SU8*. 2005. San Diego, CA, USA: SPIE.

[14] S.A. Evenson and A.H. Rawicz, *Applied Optics*, 1995. **34**(31): p. 7302.

[15] J. Roncali and F. Garnier, *Applied Optics*, 1984. **23**(16): p. 2809.

[16] J.S. Batchelder, A.H. Zewail, and T. Cole, *Applied Optics*, 1979. **18**(18): p. 3090.

[17] A.A. Earp, G.B. Smith, P.D. Swift, and J. Franklin, *Solar Energy*, 2004. **76**(6): p. 655.

[18] W.R.L. Thomas, J.M. Drake, and M.L. Lesiecki, *Applied Optics*, 1983. **22**(21): p. 3440.

[19] R.W. Olson, R.F. Loring, and M.D. Fayer, *Applied Optics*, 1981. **20**(17): p. 2934.

[20] B. Beche, N. Pelletier, E. Gaviot, and J. Zyss, *Optics Communications*, 2004. **230**(1-3): p. 91.

[21] H. Kogelnik and C.V. Shank, *Journal of Applied Physics*, 1972. **43**(5): p. 2327.

[22] G. Heliotis, R. Xia, D.D.C. Bradley, G.A. Turnbull, I.D.W. Samuel, P. Andrew, and W.L. Barnes, *Journal of Applied Physics*, 2004. **96**(12): p. 6959.

Chapter 6

Towards Mode-Locked Organic Lasers

6.1. Introduction

The demonstration of an LED pumped organic laser successfully removes the necessity for expensive excitation lasers and simplifies the whole system. However, to enhance the utility of organic semiconductor lasers in various fields, it would be desirable to have more control over the pulse duration and peak power. Since the demonstration of the first laser in the 1960s [1], great progress has been made in developing short pulse lasers. Q-switching, gain switching and mode locking are three widely applied methods of generating short pulses. Organic semiconductor lasers have commonly been operated in a gain-switched mode. These have generated sub-picosecond pulses [2], although this has required an expensive femtosecond laser as the pump source. Q-switching and mode locking can generate pulses shorter than the pump pulse duration. In comparison to Q-switching, mode locking has the advantage of giving output pulses with duration not limited by the cavity round trip time[3]. In the early 1980s, pulsed and c.w. mode locked organic dye lasers have been successfully demonstrated the generation of sub-picosecond pulses with tunability covering the whole visible spectrum by using different combinations of gain media and saturable absorber dyes [4-7]. However, to manage the fast photo-degradation, the dye solutions of

both gain media and saturable absorber must be rapidly flowed through the cavity, making these lasers less attractive in terms of portability, size and price. In contrast, organic semiconductor lasers have been demonstrated in solid state with relatively low lasing threshold in different kinds of resonators [8-11]. With emission spectra as broad as organic dyes, organic semiconductors are potentially good candidates for generating short pulses.

In this chapter, the impact of saturable absorbers on the performance of organic semiconductor lasers is investigated, serving as the first step towards passively mode locked organic semiconductor lasers. **Section 6.2** gives an introduction to saturable absorbers and passively mode locked lasers, followed by a study of the chosen saturable absorber in **Section 6.3**. This is divided into several sub-sections to discuss the saturation absorption of the chosen material, the theoretical modelling of the saturation behaviour, and the feasibility of combining it with a Bragg mirror to build an organic SESAM. In **Section 6.4**, the saturable absorber is included in a suitable laser resonator as a feasibility study of controlling the laser dynamics. The characterization of the selected organic semiconductor laser is described in **Section 6.5**. In order to identify the impact of the saturable absorber, a comparison is made between the performance of the laser with and without the saturable absorber both spectrally and temporally. In the final section, **Section 6.6**, a theoretical model is applied to simulate the laser dynamics from the cavity used in **Section 6.5** to give insight to the experimental results.

6.2. Principles of saturable absorbers & passive mode locking

Saturable absorbers are the critical elements in both passively mode-locked and passively Q-switched lasers for encouraging pulsed over CW operation. Saturable absorption is characterized by the decrease of the absorption with the increase of the incident intensity. This is not a unique property restricted to a specific category of materials. In fact, most materials show some degree of saturable absorption. In a simple picture, saturable absorption can be explained by a two-level energy model as shown in Figure 6.1[3].

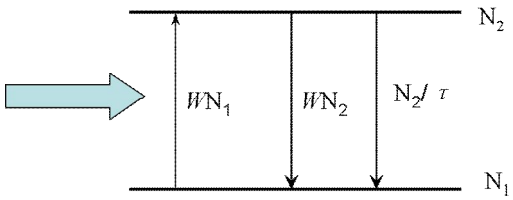

Figure 6.1. Two-level energy states for saturation absorption ([3])

In the figure, N_1 and N_2 are the population densities in the ground and the excited state respectively. In thermal equilibrium, $N_1 > N_2$ according to Boltzmann statistics. When illuminated with light of the correct frequency, the atoms in the ground state absorb the excitation at a rate W and are raised to the excited state. The atoms in the excited state relax back to the ground state by spontaneous emission at a rate determined by the excited state lifetime τ. Apart from spontaneous emission, stimulated emission also contributes to the depletion of the excited state population. The total change of N_2 can be written as:

$$\frac{dN_2}{dt} = W(N_1 - N_2) - \frac{N_2}{\tau}$$

$$W = \frac{\sigma I}{h\nu} \qquad \textbf{6-1}$$

The absorption rate W is proportional to the incident light intensity I and the absorption cross-section σ. In the steady-state, equation 6-1 gives that the

populations N_1, N_2 are related by:

$$N_2 = \frac{N_1}{1+\frac{I_{sat}}{I}}, \text{ where } I_{sat} = \frac{h\nu}{\sigma\tau} \qquad \textbf{6-2}$$

At a sufficiently high incident intensity, the stimulated emission and absorption rates become much larger than the spontaneous emission. The material becomes transparent for the incident beam and the absorption is saturated. The term saturation intensity I_{sat} refers to the intensity of the incident beam at which the transmission reduces to the cube root of its original value.

The energy states in a real organic saturable absorber usually constitute a four levels system as shown in Figure 6.2, with short lifetimes and thus fast decay rates in the 4th and the 2th states, similar to the four-level energy states of a laser gain medium discussed in **Chapter 2**. The fast decays lead to small population densities in these two states. Therefore, N_4 and N_2 are very small, compared to N_1 and N_3.

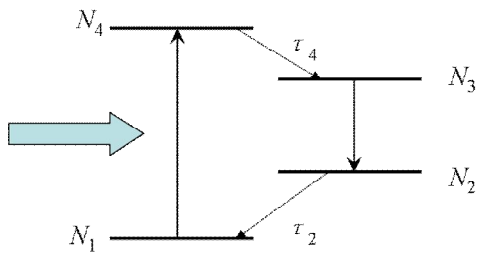

Figure 6.2. Four-level energy states ([3])

For the four-level energy system, the saturation absorption theory is similar to the simplified two-level system in Figure 6.1. The absorption transparency occurs when the populations in the ground state and upper states equalized. In this case, I_{sat} is the intensity at which the transmission drops to the square root of the original value.

Although absorption saturation exists in many materials, only a small number can potentially be used as saturable absorbers, because the saturation intensity I_{sat} is usually very high and close to the damage threshold of the materials. A good saturable absorber for a mode-locked laser or a Q-switched laser usually has the following properties. Firstly, its absorption should overlap with the lasing wavelength to modulate the laser beam effectively. Additionally, the saturation intensity should be low to avoid material damage and photodegradation. For mode locking, the upper state lifetime of the material should be shorter than the cavity round trip time so that it can fully recover before the arrival of the next circulating pulse. Several materials can be used as saturable absorbers, such as organic dyes [12] , quantum dots [13], carbon nanotubes [14], graphene [15]and semiconductor saturable absorber mirrors (SESAMs) [16].

As mentioned before, saturable absorbers can be used for passive mode locking in a laser resonator to generate ultra short pulses. In general, the term 'mode-locking' refers to the formation of a fixed phase relationship between the longitudinal modes of a laser resonator. These phase locked cavity modes interfere to form a circulating pulse of extremely short duration [17]. This circulating pulse is coupled out of the resonator each time it hits the output coupler, giving a repetition rate equal to the Free Spectral Range (FSR). In the simplest case, for a conventional Fabry-Perot cavity consisting two plane mirrors surrounding the gain medium, the free spectral range (FSR) between the cavity longitudinal modes is related to the cavity length L by

$$\Delta\nu = \frac{c}{2L} \qquad \textbf{6-3}$$

Among all the longitudinal modes supported by the resonator, only those whose frequencies overlap with the gain curve of the gain medium can contribute to the final laser output, as illustrated in Figure 6.3.

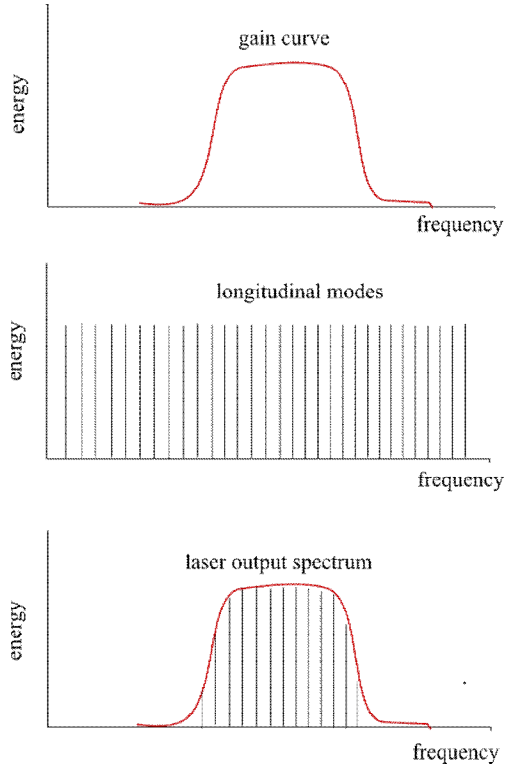

Figure 6.3. Fabry-Perot cavity modes for mode lock lasers

The duration of the output pulse is determined by many factors such as the configuration of the resonator, the gain medium, and dispersion. A Fourier transform relationship between the pulse duration and the spectral width of the gain limits the minimum pulse duration. A broad gain bandwidth is preferred for generating short pulses. Passive mode locking can produce pulses as short as a few femtoseconds in broadband lasers [18-19].

To achieve passive mode locking, the saturable absorber can be placed inside the resonator as an extra element or it can be embedded with the cavity mirror to modulate the cavity loss. Initially, the free running cavity modes oscillate independently in phase inside the resonator, leading to random fluctuations in intensity. When such a fluctuating laser field is incident on the saturable absorber, the intense spikes are preferentially transmitted, while the low intensity background will be absorbed. Consequently, the saturable absorber can

successfully discriminate the high energy spike from the noisy background [20].

Generally, two kinds of saturable absorbers are used for passive mode locking: fast saturable absorbers and slow saturable absorbers. The fast saturable absorber has a recovery time in the order of a few picoseconds. When a laser spike enters the fast saturable absorber, its leading edge can be steepened by absorbing the initial low energy fraction. Its trailing edge can also be absorbed, if the saturable absorber recovers before the spike travels through. As the spike circulates many round trips inside the resonator, the sharpening process repeats and the spike becomes steepened and steepened both in the leading and trailing edges. Eventually, the energy will be compressed into a very short pulse. For the slow saturable absorber, the recovery time is relatively long, in the region from tens to hundreds of picoseconds. Therefore, it cannot recover immediately after the peak of the spike passes through. Only the leading edge of the spike can be steepened by the slow saturable absorber. To achieve short pulses with these slow saturable absorbers, gain saturation is also required. When the laser spike enters the gain medium, the inversion is saturated by the energy in the leading edge, so that the trailing edge must propagate through the material without being amplified. After repeated round trips, the pulse becomes sharper in its leading edge due to the saturable absorber and steepened in the trailing edge by the gain medium. The combination of the slow saturable absorber and the gain medium can generate pulses shorter than the recovery time of the absorber. Hence, the pulses obtained from slow saturable absorber cavities can even be shorter than those from fast saturable absorber cavities.

6.3. Saturable absorber characterization

6.3.1. Material for saturable absorber

In the history of mode-locked solution dye lasers, saturable absorber dyes have been demonstrated to be capable of giving pulses as short as 19 fs [21]. Therefore, they were chosen as the saturable absorbers for the study on organic semiconductor lasers.

The chosen dye in this study is 1,1',3,3,3',3'-Hexamethylindodicarbocyanine Iodide Hexacyanine 2 (HIDCI) (Exciton). The molecular structure is shown in Figure 6.4. This dye has been previously used in flash lamp pumped passively mode-locked Rhodamine 6G lasers [22].

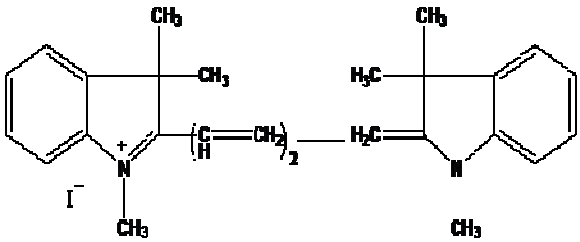

Figure 6.4. Molecular structure of HIDCI ($C_{27}H_{31}N_2I$, M.W. 510.46)

The impact of the saturable absorber dye will be studied in solid state for organic semiconductor lasers, rather than the conventional solution state, to maintain the compact feature of organic semiconductor laser systems. To slow down the oxidation and degradation, the dye molecules are separated by a passive polystyrene matrix. The absorption and photoluminescence spectra of the polystyrene doped HIDCI are ploted in Figure 6.5. The PL spectrum was obtained by exciting the sample with the OPO at 600 nm. A long pass filter was used before the CCD detector to block the OPO excitation beam. The Fluromax, described in **Chapter 3** for normal PL measurement, is not sensitive enough for detecting PL

above 700 nm.

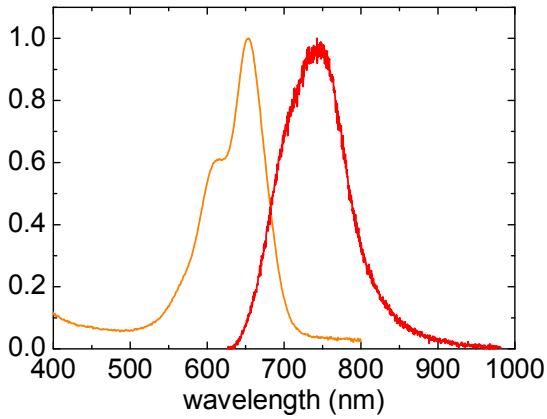

Figure 6.5. (Orange) Absorption and (red) PL spectra of HIDCI doped polystyrene

In Figure 6.5, HIDCI has a broad absorption spectrum spanning from 550 nm to 700 nm with two vibronic peaks at 600 nm and 630 nm. The absorption band matches well with the MEH-PPV PL spectrum shown in **Chapter 4**, making it suitable for MEH-PPV lasers.

6.3.2. Experimental

Before the saturable absorber can be used, its properties such as the saturation intensity and upper state lifetime should be characterized. A Streak camera with response time of 2 ps was used to measure the excited state lifetime. The saturable absorber film was held in vacuum and exited by a 100 fs laser pulse at 400 nm.

The saturation intensity was studied with the experimental setup described in Figure 6.6.

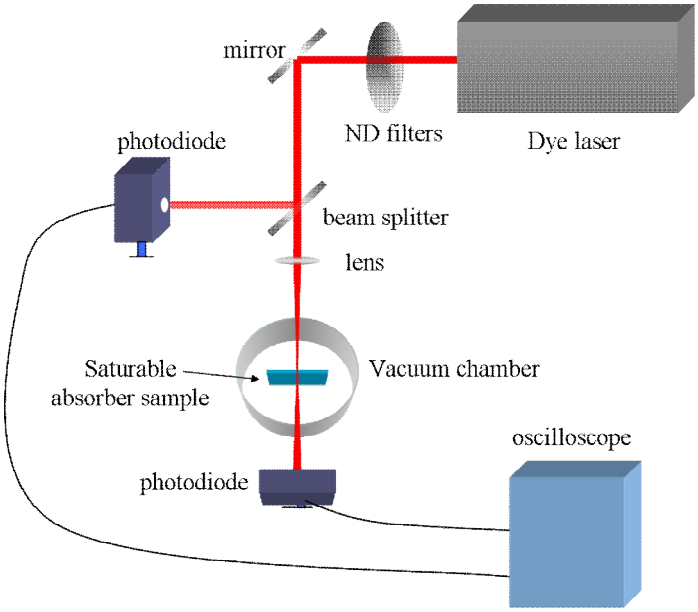

Figure 6.6. Experimental setup for measuring saturation intensity

The saturable absorber was placed inside a vacuum chamber at 10^{-4} mbar to prevent oxidation and photodegradation during the experiment. The sample was excited by a nitrogen laser pumped dye laser whose output wavelength can be tuned in the visible spectral range by changing the dye solution. The output pulse from the dye laser was 500 ps in duration with repetition rate of 6 Hz. A series of neutral density (ND) filters were used at the output aperture of the dye laser to change the excitation intensity. The combination of the ND filters can change the excitation energy by a factor of 10000. The maximum pulse energies were around a few μJ and slightly wavelength dependent. The transmission of the sample was measured at different excitation energies to form an absorption curve, from which the saturation intensity can be deduced. To reduce the influence of the energy fluctuation of the dye laser, an extra beam path was added to monitor in-situ the excitation energy for each transmission measurement. 5% of the excitation was reflected to the monitor photodiode by a beam splitter. The remaining excitation

was focused onto the saturable absorber sample and the transmission was measured by another photodiode. Both photodiodes were connected to an oscilloscope for energy measurements. The two photodiodes used for the monitor and transmission measurement were identical.

6.3.3. HIDCI saturable absorption

6.3.4.1. Experimental results

1 mg/ml HIDCI was blended with 40 mg/ml polystyrene in chloroform to form a 2.5% w.t. blend with a film thickness of 8 μm from spin coating at 2000 r.p.m.. The sample was excited at 610 nm with a spot of 109 μm by 118 μm. Figure 6.7 shows the dependence of the absorption in percentage on the excitation intensity from 4 nJ to 4 μJ.

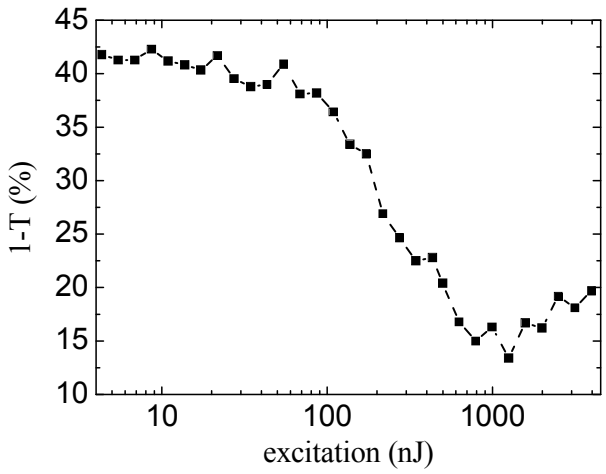

Figure 6.7. Absorption vs excitation for 2.5%w.t. blend

When the excitation energy increased from 4 nJ to 100 nJ, the absorption stayed at the 40% level with a small decrease. A large drop of the absorption from 40% to 15% occurred as the excitation increased from 100 nJ to 700 nJ, indicating the

absorption was saturated to the level of 15%. In theory, the saturable absorber should become transparent at high excitation and the absorption should drop down to zero. The non-zero 'absorption' observed in the graph could be attributed to several loss mechanisms, such as reflection losses from both surfaces of the sample and scattering loss from the vacuum chamber and the sample (e.g.: propagating losses in polystyrene matrix and the surface roughness). As the excitation further increased to 4 μJ, a small reverse increase was observed in the absorption, which also deviates from the theory mentioned in **Section 6.2**. The simplified theory only includes the spontaneous and stimulated decays for upper state depletion. In reality, other intermolecular interactions, such as excited state absorption and multi-photo absorption, could become significant when the excited state population increases. Specifically, for cyanine dyes, the formation of J-aggregates at high concentrations introduces an additional narrow absorption band usually observed at approximately 600 nm -700 nm [23-24]. This extra absorption overlaps well with the HIDCI monomer absorption spectrum and thus could contribute to the absorption characteristics.

The saturation intensity measured from Figure 6.7 should be the excitation intensity at which the transmission drop to the square root of its initial value. From the figure, this occurred at 250 nJ and thereby the saturation intensity I_{sat} corresponds to 3.8 MW/cm^2. To achieve this saturation intensity, it is highly possible that the organic semiconductor lasers require pumping at a relatively high level and the internal laser fields need to be focused into a very small spot. However, high pumping energies could lead to a fast photodegradation of the gain medium. Consequently, it is worth trying to reduce the saturation intensity.

According to equation 6-2, I_{sat} is inversion proportional to the product of the absorption cross section and the upper state lifetime. To reduce I_{sat}, either its

absorption cross section or the upper state lifetime should be increased. This could be achieved by varying the HIDCI doping concentration in the polystyrene matrix to change the packing condition of the dye molecules.

Figure 6.8 gives the absorption curves for two further HIDCI doping concentrations of 5% w.t. (2 mg/ml) and 1% w.t. (0.4 mg/ml).

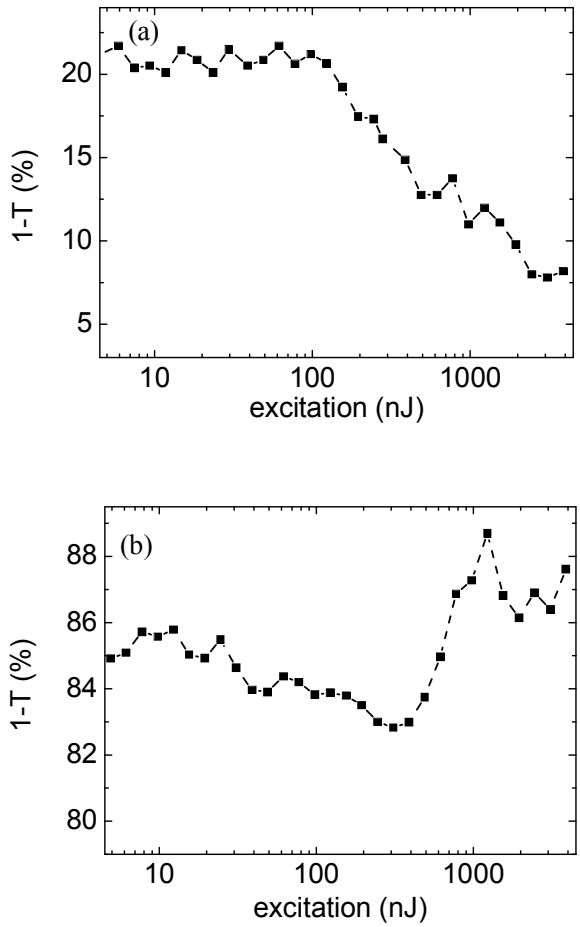

Figure 6.8. Absorption vs excitation: (a) 1% w.t.; (b) 5% w.t. HIDCI blend

For the 1% w.t. blend, the absorption decreased from 20% to 8% as the excitation intensity increased. The reduction of the absorption (12%) is smaller than that of the 2.5% w.t. blend shown in Figure 6.7. The saturation intensity I_{sat} was measured to be 1.2 μJ, corresponding to 2.9 MW/cm^2 with a 290 μm by 282 μm excitation beam. On the other hand, the 5% w.t. blend exhibited a very severe reverse increase of the

absorption at high excitation intensity, making the initial reduction in the absorption (~ 2% from 10nJ to 500 nJ) barely observed. As a result, I_{sat} cannot be directly deduced from the graph and it is not suitable as saturable absorber.

Figure 6.7 and Figure 6.8 show that a decrease in the dye concentration can lower the saturation intensity I_{sat}. Slightly lower concentrations of 0.25% w.t. and 0.125% w.t. were tested to look for a further reduction in the saturation intensity. However, these two blends showed non-saturated absorptions of less than 10%, falling into the background noise level discussed in Figure 6.7 and making the measurements difficult and inaccurate. To measure the saturation intensities of these samples requires experimental setups with higher accuracy, which unfortunately was not tried due to a lack of time.

Besides the saturation intensity, the upper state lifetime of the saturable absorber needs to be characterized. It is essential for a passively mode-locked laser that the cavity round trip time should be longer than the saturable absorber lifetime so that the saturable absorber can completely recover before the next cycle starts. A Hamamatsu camera was used to measure the lifetimes of the three HIDCI doped polystyrene blends. The PL decay dynamics of the three blends are illustrated in Figure 6.9 and summarized in Table 6.I.

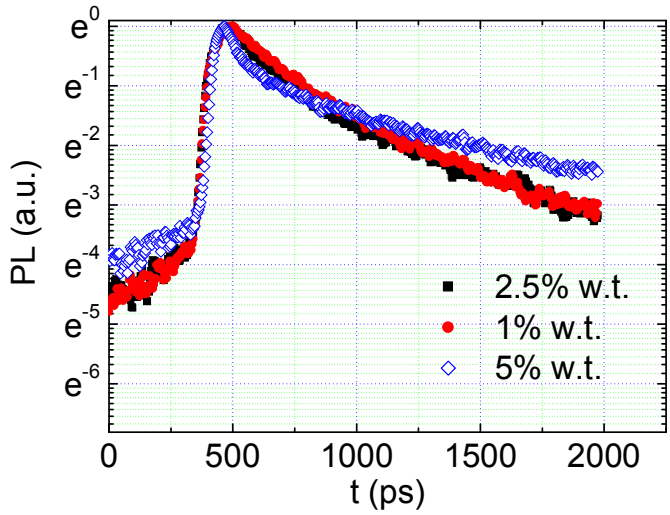

Figure 6.9. PL decays of the three HIDCI doped polystyrene blends

Concentration	Lifetime τ (ps)
1% w.t.	283
2.5% w.t.	225
5% w.t.	125

Table 6.I. Lifetimes extracted from Figure 6.9

Figure 6.9 implies that the PL decay changed from mono-exponential to multi-exponential characteristics as the dye concentration increased. The exact reason is not clear. It could be due to the strong intermolecular interaction between the dye molecules at high concentration which adds additional non-radiative decay paths between the excited state and ground state. The obvious multi-exponential PL decay of the 5% w.t. blend could explain the strong reverse increase in the absorption at high excitation intensities observed in Figure 6.8. In Table 6.I, the PL lifetimes of the three blends are in the range of hundreds of picoseconds, which indicates that the cavity length should be at least millimetres long.

6.3.4.2. Numerical simulation of saturation intensity

As discussed in **Section 6.3.1**, saturable absorption dyes can be described through a theoretical model by assuming a four energy system in Figure 6.2. Slightly different to equation 6-1, the change in the ground state population N_1 is described by:

$$\frac{dN_1(I)}{dt} = -\frac{N_1(I)I\sigma}{h\nu} + \frac{N_3(I)}{\tau} \qquad \textbf{6-4}$$

If higher energy states are not taken into account, the total population N_t can be written as:

$$N_t = N_1 + N_3 \qquad \textbf{6-5}$$

By substituting equation 6-5 into equation 6-4 to remove N_3 and using I_{sat} defined in equation 6-2, the population density N_1 in steady state can be derived from equation 6-4, by taking dN_1/dt=0:

$$N_1(I) = \frac{N_t}{1 + \frac{I}{I_{sat}}} \qquad \textbf{6-6}$$

As the excitation beam with intensity I pass through an absorbing medium with length L in the z direction, the change in the excitation intensity can be represented as:

$$\frac{dI}{dz} = -I\sigma N_1(I) \qquad \textbf{6-7}$$

The ground state population N_1 is excitation intensity I dependent. The transmission of the excitation can be calculated by taking the integral of equation 6-7:

$$\int_{I_{in}}^{I_{out}} \frac{1}{I\sigma N_1(I)} dI = -\int_0^L dz \qquad \textbf{6-8}$$

The expression of N_1 from equation 6-6 can be substituted into equation 6-8 to solve the integral to give:

$$\sigma N_t L = \frac{I_{in}}{I_{sat}} - \frac{I_{out}}{I_{sat}} - \ln(\frac{I_{out}}{I_{in}}) \qquad \textbf{6-9}$$

In equation 6-9, I_{in} and the I_{out} are normalized to I_{sat}. The relationship between the transmission, $\sigma N_t L$, and absorbance (optical density O.D.) can be described as:

$$\frac{I_{out}}{I_{in}} = \exp(-\sigma N_t L) = 10^{-O.D.} \qquad \textbf{6-10}$$

Therefore, using equations 6-9 and 6-10, a contour plot of $\sigma N_t L$, representing the dependence of the absorbance on the excitation intensity, can be plotted with $\log(\frac{I_{in}}{I_{sat}})$ and optical density (O.D.), $\log(\frac{I_{in}}{I_{out}})$, as variables. This is shown in Figure 6.10. The contour lines indicate that the absorbance decreases as the excitation intensity increases, showing the characteristics of absorption saturation.

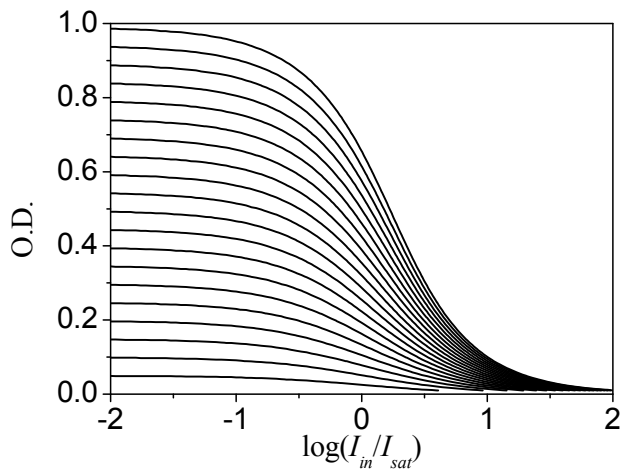

Figure 6.10. The dependence of absorbance on excitation intensity

The saturation intensity I_{sat} can be used as the fitting parameter to fit the experimental results of the 2.5% w.t. and 1% w.t. HIDCI blends obtained in **Section 6.3.4.1** into the universal plot of Figure 6.10. The results are plotted in Figure 6.11.

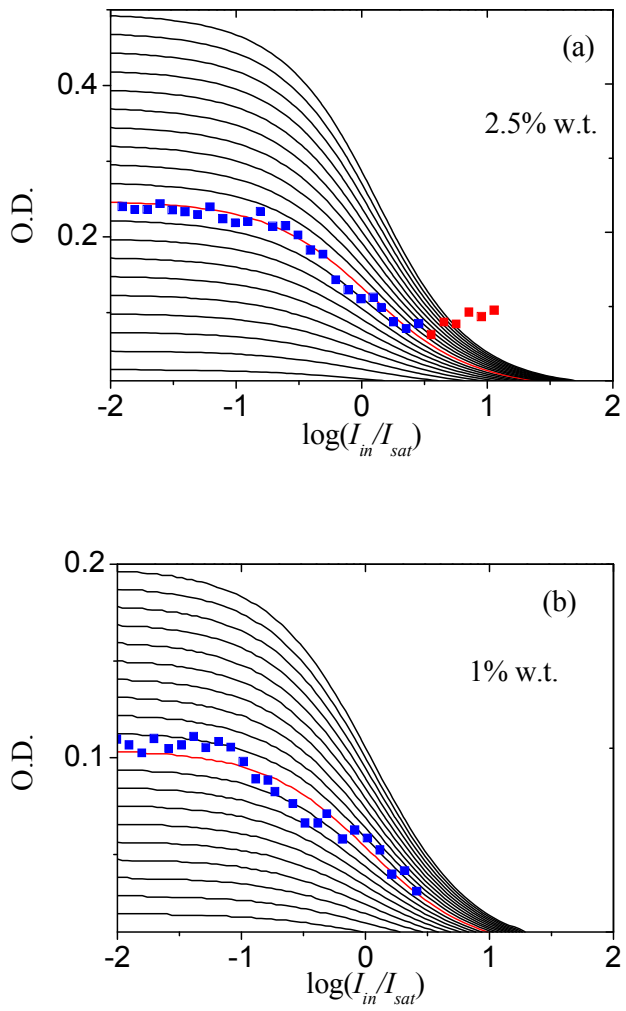

Figure 6.11. Theoretical fits for (a) 2.5% w.t. and (b) 1% w.t.

In Figure 6.11, when suitable I_{sat} was chosen, the experimental results of both blends at low excitation intensities (blue squares) agrees well with the theory. The two unsaturated optical densities for the 2.5% w.t. and 1% w.t. blends are 0.25 and 0.11 respectively. For the 2.5% w.t. blend, the experimental data at high excitation intensity (red squares) deviates from the contour lines. These data points

correspond to the increasing tail in Figure 6.7 and Figure 6.8, which cannot be explained by the simple model. The fitting values of I_{sat} and the directly measured I_{sat} values are compared in Table 6.II.

Concentration	I_{sat} (measured)	I_{sat} (theoretical)
1% w.t.	2.9 MW/cm^2	4.5 MW/cm^2
2.5% w.t.	3.2 MW/cm^2	6.3 MW/cm^2

Table 6.II. Comparison of measured and theoretical I_{sat} values

The theoretical confirms that the increase of the dye concentration leads to an increase in the saturation intensity, as observed from experiments. By knowing the saturation intensity and the upper state lifetime, according to equation 6-2, the ground state absorption cross section can be deduced (in Table 6.III).

Concentration (w.t.)	absorption cross section (10^{-16} cm^2)
1%	2.5 ± 0.1
2.5%	2.6 ± 0.3

Table 6.III. Absorption cross section for HIDCI doped polystyrene

The values of σ are in the order of 10^{-16} cm^2, comparable to the absorption cross sections of other organic dyes such as Rhodamine 6G and DOCI.

6.3.4. HIDCI SESAM

Semiconductor Saturable Absorber Mirrors (SESAMs) are key components in modern ultrafast laser systems. They are widely used in diode pumped solid state lasers to give short pulse output with high power and repetition rate. The large absorption cross section (in the range of 10^{-14} cm^2) of SESAM results in very low saturation flux of tens of μJ/cm^2 [25]. However, most SESAMs work in the infrared region between 800 nm and 1 μm and are thus not suitable for organic

semiconductor lasers whose emission are mainly in the visible spectral range. Recently, a GaN based SESAM has been demonstrated to operate near 410 nm with the potential for mode locking blue emitting lasers [16]. Nevertheless, the complicated and expensive fabrication of SESAMs involves the growth of semiconductor quantum dots or quantum wells on top of a highly reflective semiconductor Bragg substrate. A hybrid saturable absorber mirror with a thin layer of organic dye deposited on an inorganic Bragg substrate would simplify the fabrication process and thereby reduce the cost of the ultrafast laser system. Additionally, tunability across the visible spectral range could easily be accessed by using a range of organic dyes.

Showing characteristics of absorption saturation, the two HIDCI doped polystyrene thin films of 2.5% w.t. and 1% w.t. are suitable for such hybrid SESAMs operating in the region between 550 nm and 650 nm. To construct a SESAM, solutions of HIDCI doped polystyrene were spin coated onto a Bragg mirror substrate purchased from LaserOptik (Part No. A050519). These substrates were designed to exhibit high reflectivity (>99.9%) in the wavelength region of 590 nm - 690 nm (Figure 6.12).

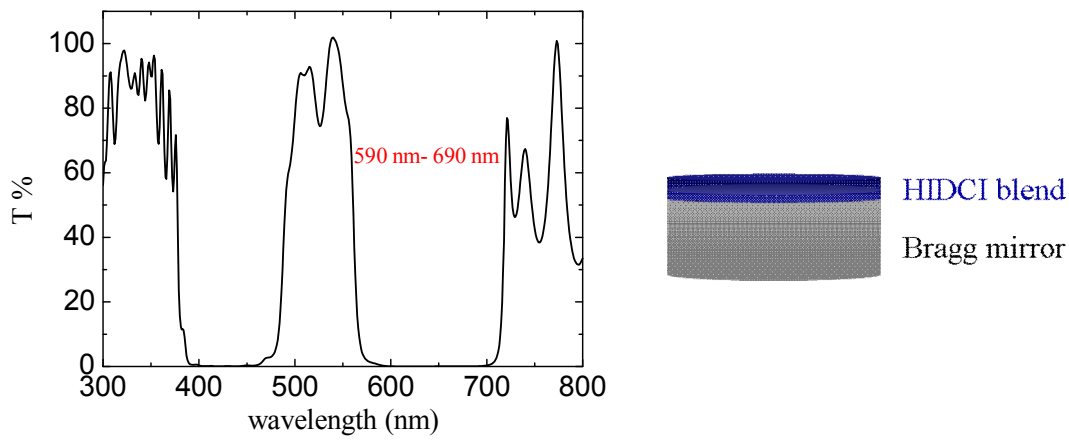

Figure 6.12. (left) The transmission spectrum of the Bragg mirror; (right) HIDCI SESAM

The experimental setup shown in Figure 6.6 was used to characterize the sample. The reflection of the 610 nm excitation light was collected by the photodiode to reveal the dependence of the reflectivity of the SESAM on the excitation intensity, as indicated in Figure 6.13.

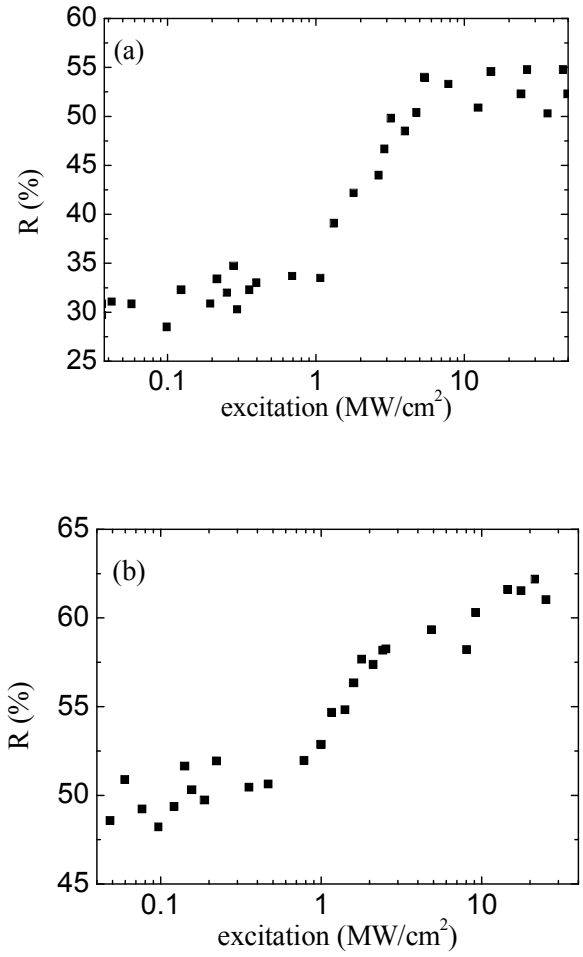

Figure 6.13. The dependence of reflectivity on excitation intensity:

(a) 2.5% w.t.; (b) 1% w.t.

Both 2.5% w.t. and 1% w.t. samples showed an increase in reflectivity as the excitation intensity increased. Such behaviour arises from the absorption saturation in the HIDCI layer at high intensity observed previously. The 2.5% w.t. sample gave a 20% difference in reflection, increasing from 30% to 50%. It is larger than the 10% increase for the 1% w.t. sample. The change in the reflectivity

corresponded well with the change in the absorption of the two blends shown in Figure 6.7 and Figure 6.8. The saturation intensities for the 2.5% w.t. and 1% w.t. samples were 4 MW/cm^2 and 2 MW/cm^2 respectively, close to the saturation intensities listed in Table 6.II. The demonstration of the intensity dependent reflectivity of the two HIDCI-Bragg mirrors proves that hybrid SESAMs could be promising candidates for passively mode-locked visible lasers.

6.4. Organic semiconductor laser cavity

To match the absorption spectrum of the HIDCI saturable absorbers, MEH-PPV was chosen as the laser gain medium. Its PL spectrum covers most of the orange-red region from 550 nm to 680 nm. In films, the gain of MEH-PPV spans from 620 nm to 640 nm, overlapping well with the absorption spectrum of HIDCI. As a preliminary investigation, the impact of the saturable absorber will be explored in a solution based laser cavity shown in Figure 6.14. Although solution lasers are much less attractive than solid state lasers, it is a convenient starting point to gain insight into the interaction between the gain medium and the saturable absorber, which can then be easily adapted to solid state organic semiconductor lasers.

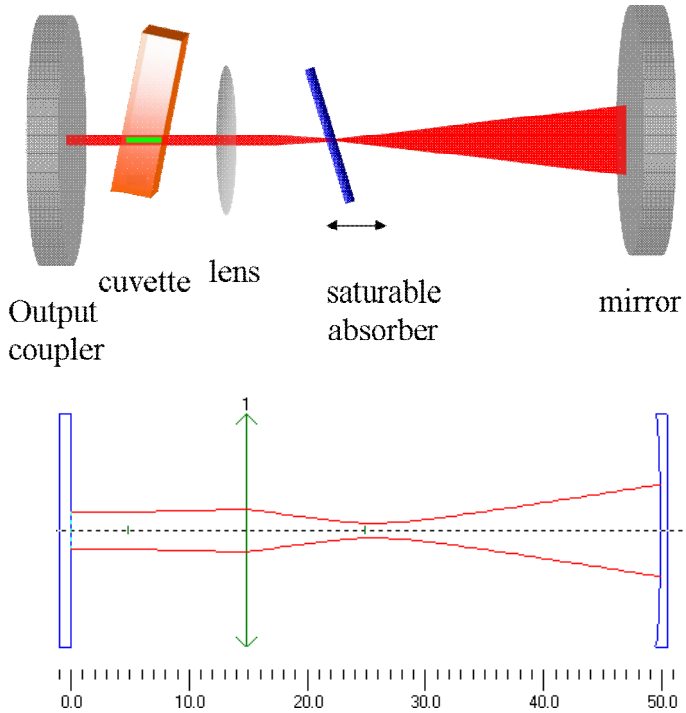

Figure 6.14. Solution MEH-PPV laser cavity:

(Top) Cavity layout; (Bottom) Simulated cavity mode (from 'Psst!')

In Figure 6.14, the laser cavity is formed by two dielectric mirrors (LaserOptik) and a short focal length lens (Comar). The cavity length is 50 mm so that the cavity round trip time is estimated to be 330 ps, longer than the upper state lifetime of the HIDCI saturable absorbers (Table 6.I). The cuvette containing the MEH-PPV solution is placed in between the output coupler and the lens at a small angle to prevent reflections from the cuvette walls forming a second small cavity. The solution was stirred by a magnetic stirrer during the experiment to slow down the potential photodegradation. The right cavity mirror is a concave dielectric mirror with radius of curvature of 25 mm and reflectivity greater than 99%. The left output coupler is a plane mirror with reflectivity of 95% between 590 nm and 690 nm. The AR coated lens, 10 mm focal length, is placed 14 mm away from the output coupler to focus the internal laser field to a 20 μm diameter spot. The radius of the cavity mode in the cuvette is calculated to be 105 μm. The solution laser is transversely pumped by a stripe (represented by the green bar) with diameter of 170 μm to match

the internal laser mode. The saturable absorber was mounted on a translation stage and titled to prevent on axis surface reflections.

The impact of the saturable absorber on both the spectral and temporal properties of the laser pulses was studied. Figure 6.15 shows the experimental layout for device characterization.

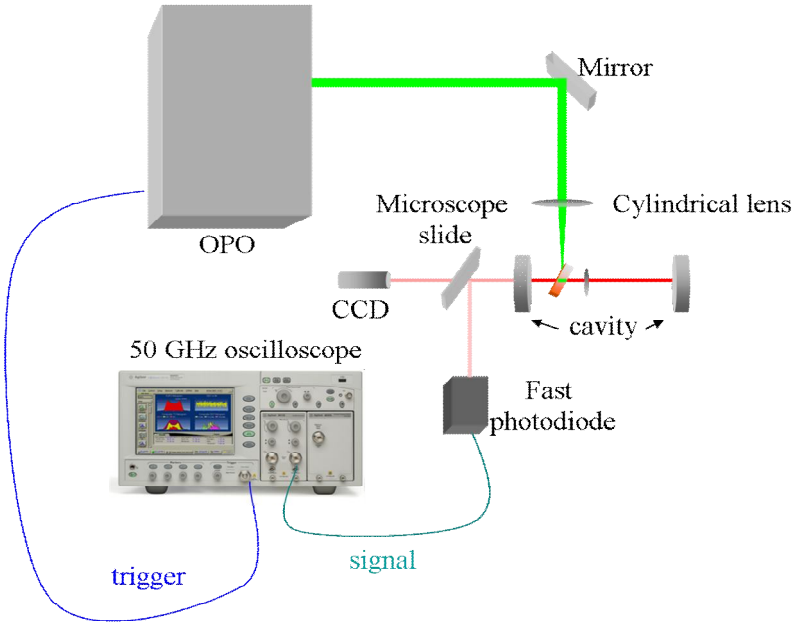

Figure 6.15. Experimental setup for device characterization

To match the absorption peak of the MEH-PPV, the solution laser was transversely pumped at 500 nm by OPO at 20 Hz. The setup allows simultaneous measurements of the emission spectrum and the pulse temporal profile by splitting the output beam with a microscope slide. Most of the output beam was collected by the CCD coupled spectrograph for spectral measurement. A 4% portion of the beam was reflected from the microscope slide and focused onto a high speed photodiode (Standa Ltd. Model: 11HSP-V2) connected to a 50 GHz oscilloscope (Agilent Technologies, 83484A) for temporal measurements. The combination of the photodiode and the oscilloscope was capable of measuring pulses as short as 210 ps, limited by the resolution of the high speed photodiode.

The OPO output pulse used for pumping the MEH-PPV lasers was first stretched from 4 ns to 8 ns through an additional delay path, as illustrated in Figure 6.16, to increase the pump duration.

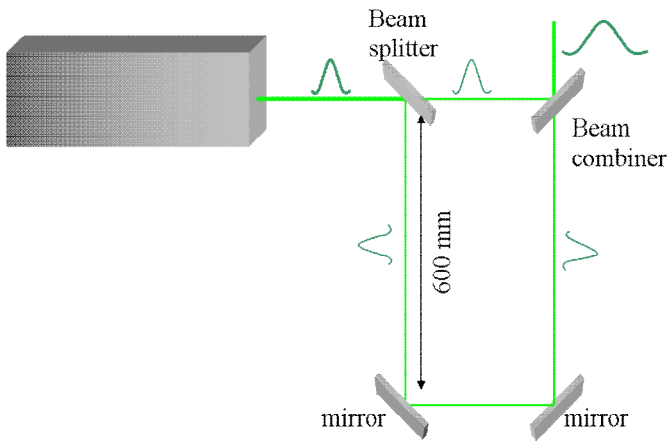

Figure 6.16. Experimental setup for stretching the OPO pulse

The output pulse from the OPO was split into two by a 50%:50% beam splitter. One half was guided through a delay line of 1200 mm by two mirrors and recombined with the other half by a beam combiner. The 1200 mm delay line shifted the pulse by 4 ns in time, in comparison to the direct pass pulse. The final combined pulse had a FWHM around 8 ns. Figure 6.17 presents the profile of the final pulse.

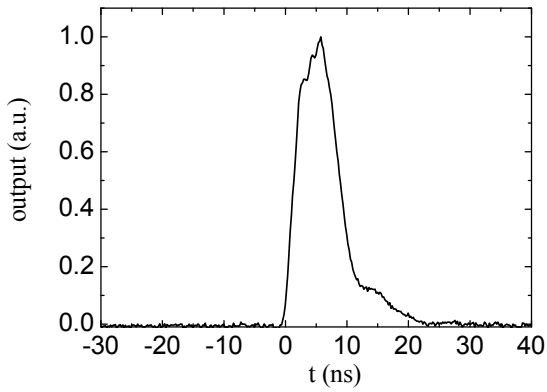

Figure 6.17. Stretched OPO pulse

The stretched pulse width was 7.5 ns, close to the expected 8 ns. The small shoulder on the tail could be due to the inaccurate timing of the two pulses.

A 2 mg/ml MEH-PPV solution in chlorobenzene, stirred in a quartz cuvette of 5 mm width (Hellma UK Ltd. model: 111.057), was used as the laser gain medium. The spectral and temporal measurements were performed on the laser both with and without the saturable absorber in order to explore the impact of the saturable absorber on the organic laser performance.

6.5. Laser characterization

6.5.1. Cavity without saturable absorber

Figure 6.18 presents the lasing spectra in the absence of the saturable absorber at different pump energies and the corresponding input vs output curve.

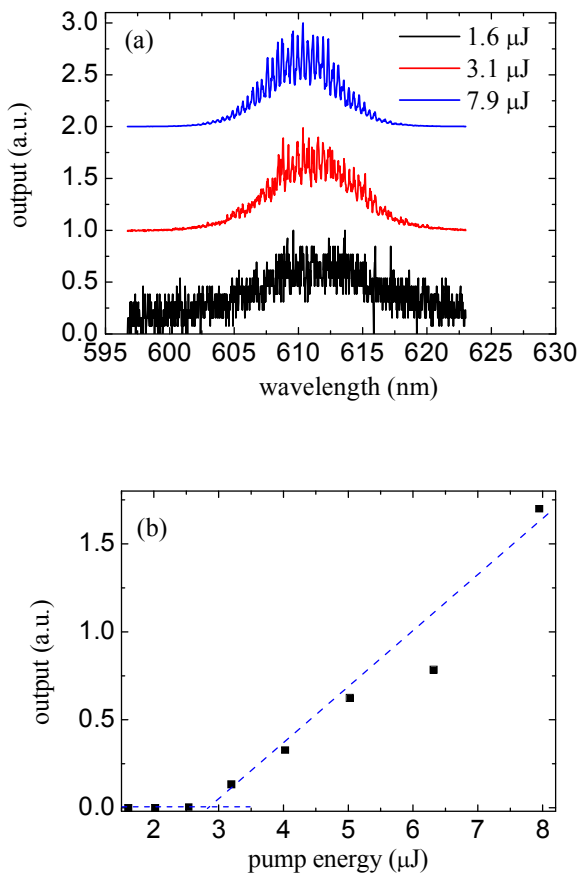

Figure 6.18. (a) Emission spectra at three pump energies; (b) Input vs output plot

Three emission spectra at different pump energies of 1.6 μJ, 3.1 μJ and 7.9 μJ are shown in Figure 6.18 (a). When the laser was below threshold (1.6 μJ), the broad emission spectrum was similar to the spontaneous emission with a peak at 615 nm, corresponding to the 0-1 vibronic peak. As the pump energy increased to 3.1 μJ, sharp peaks were superimposed in the spontaneous emission spectrum. These peaks represented different longitudinal laser modes supported by the resonator and the gain medium. Limited by the resolution of the CCD spectrograph, a FSR of 0.4 nm was measured from the spectrum, wider than the theoretical value of 3.7 pm calculated for a 50 mm long cavity. When the pump energy was further increased to 7.9 μJ, the sharp peaks increased much faster than the spontaneous emission background. The lasing threshold indicated by the input vs output graph was 2.8 μJ, equivalent to 87.5 kW/cm^2. The FWHM of the lasing spectra above threshold is 5.2 nm.

The temporal profile of the output pulse at 5 μJ is plotted in Figure 6.19. The Gaussian fit suggests a FWHM of 1.9 ns. The fluctuation in the OPO pump pulse width leads to a fluctuation of 30% in the measured output pulse width from the MEH-PPV laser.

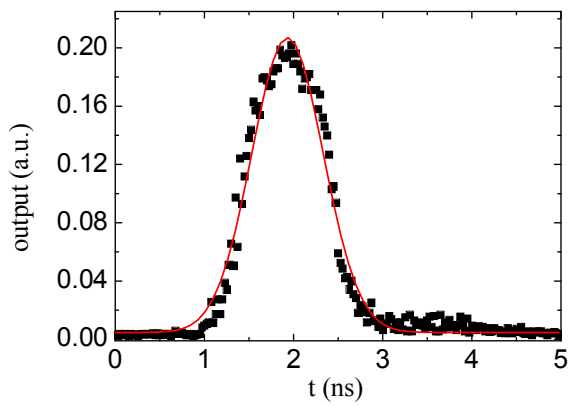

Figure 6.19. Temporal profile of the output pulse excited at 5 μJ: (black square) Experimental data; (red curve) Gaussian fit

6.5.2. Cavity with saturable absorber

The 1% w.t. HIDCI doped polystyrene film was chosen as the saturable absorber due to its lower saturation intensity of 4.5 MW/cm^2 than the 2.5% w.t. blend. Figure 6.20 illustrates the impact of the saturable absorber on the lasing threshold and spectra.

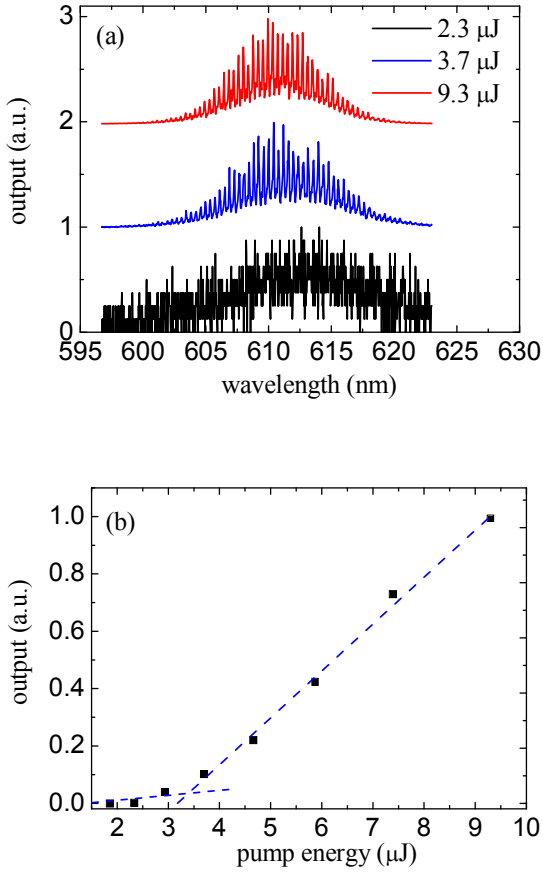

Figure 6.20. Cavity with saturable absorber:

(a) Emission spectra at different pump energies; (b) Input vs output plot

The spectra at different pump energies are similar to the spectra shown in Figure 6.18 without the saturable absorber. The lasing threshold in Figure 6.18 (b) was slightly increased by 17% to 3.3 μJ due to the additional losses brought by the saturable absorber.

To determine whether the saturable absorber can be saturated, the internal intensity of the lasing field at the saturable absorber was estimated by using the output energy measured from the 95% output coupler and the 40 μm spot size obtained from the cavity simulation in Figure 6.14. Table 6.IV summarizes the internal intensities deduced at four different pump energies by assuming a 2 ns pulse width, which is the same as the pulse without the saturable absorber. The dependence of the internal intensity on the pump energy is plotted in Figure 6.21 for a better illustration.

pump (μJ)	Output (nJ)	Internal energy (nJ)	Internal intensity (MW/cm^2)
5.8	3.5	70	2.8
7.4	7.9	152	6.4
11.7	23.4	384	18
23.4	52.1	1042	42

Table 6.IV. Calculated internal intensity at the saturable absorber

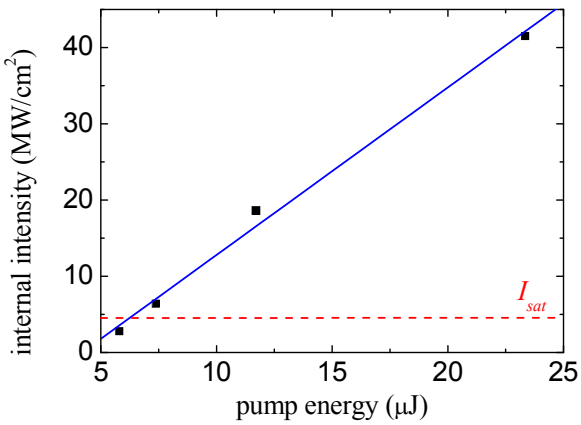

Figure 6.21. Pump energy vs internal intensity from Table 6.IV

In Table 6.IV, when the pump energy increased from 5.8 μJ to 23.4 μJ, the output energy increased from 3.5 nJ to 52.1 nJ, corresponding to a increase of the internal energy from 70 nJ to 1.04 μJ. The intensity at the focus in the cavity therefore increased from 2.8 MW/cm^2 to 42 MW/cm^2, which is plotted in Figure 6.21. As

indicated by the blue linear fit, the internal intensity increased linearly with the pump energy. When the pump energy was higher than 6.2 μJ, the internal intensity at the saturable absorber exceeded the theoretical saturation intensity of 4.5 MW/cm^2 (the dotted red line).

To characterize the temporal properties of the output pulse, the laser was pumped at 7.4 μJ to achieve free-running internal intensity of 6.4 MW/cm^2 at the saturable absorber. The saturable absorber was moved slowly on a translation stage through the focus region to vary the intensity. Figure 6.22 gives the output pulses measured by the high speed photodiode.

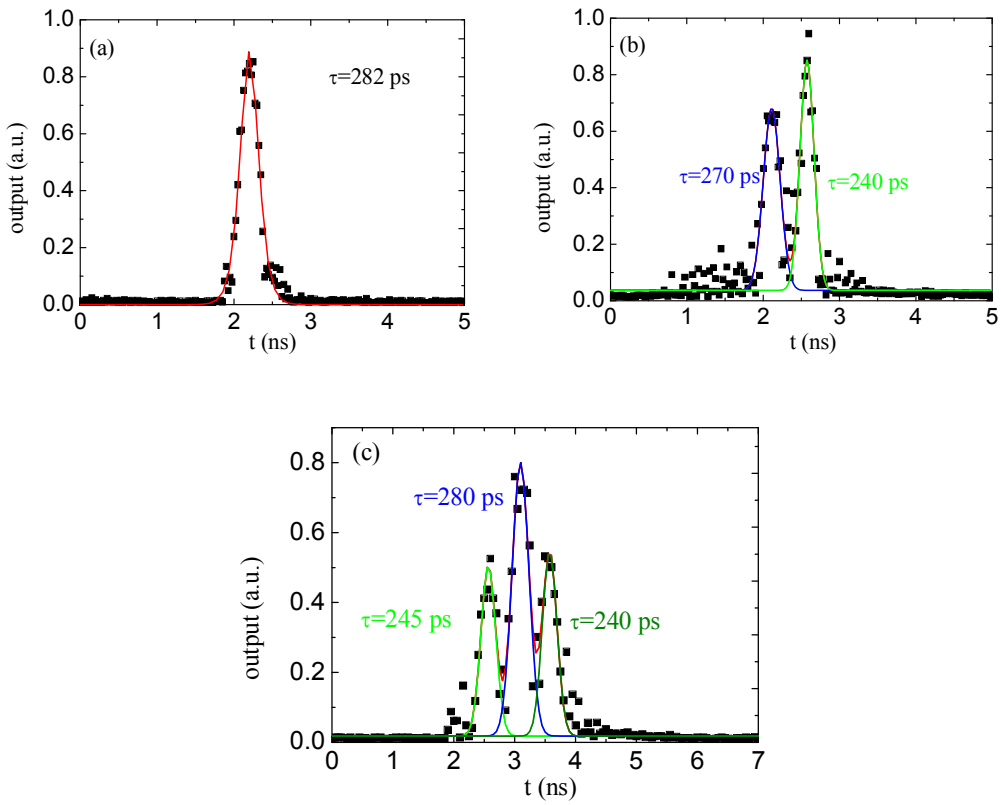

Figure 6.22. Three temporal output profiles pumped at 7.4 μJ: (solid colour curves) Gaussian Fits; (black square) Experimental data. FWHMs are indicated in corresponding colour texts

When the saturable absorber was scanned through the focus, three different pulse profiles can be detected shown in Figure 6.22. Gaussian fits, indicated by the curves, were applied to the experimental data to deduce the FWHM and pulse separations. In graph (a), when a single output pulse was recorded, the fitting curve indicated that the pulse FWHM was 282 ps. For the double pulse output, each pulse was around 250 ps and separated by 470 ps. The triple pulse, in graph (c), has a similar pulse FWHM to the double pulse case, with slightly wider pulse separation of 500 ps. In these three different cases, the pulse durations were shorter than the initial pulse without the saturable absorber in Figure 6.19 by an order of magnitude.

The saturable absorber can successfully give trains of output pulses much shorter than the pump pulse. When the pump energy increased from 7.4 μJ to 11.7 μJ, the internal intensity at the saturable absorber from Table 6.IV should increase to 18 MW/cm^2, 4 times above the saturation intensity. However, as shown in Figure 6.23, only a single pulse with duration about 1 ns was detected. This is similar to the pulse profile in Figure 6.19 without the saturable absorber. The disappearance of the pulse shortening effect at high pump energies could be due to the bleaching of the solid state saturable absorber at such high incident intensities. But a definite conclusion cannot be generated at this stage.

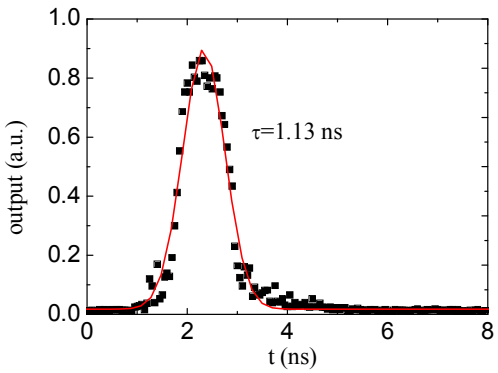

Figure 6.23. Output pulse pumped at 23.4 μJ:

(black square) Experimental data; (red curve) Gaussian fit

Additionally, the impact of output coupling efficiencies, which is related to the Q factor of the laser resonator and hence the pulse build up time, was also investigated. Besides the 5% output coupling mirror used above, another two output couplers with transmissions of 15% and 35% were tested. For each case, the laser was pumped at twice above the threshold, the same as the pumping situation for the 5% output coupler. The three output pulse profiles shown in Figure 6.22 from the 5% coupler were also observed for the 15% and 35% output couplers. Figure 6.24 gives a detailed comparison of pulse width and pulse separation for the three output couplers. It shows the increase of the output coupling efficiency from 5% to 35% leads to an increase of the output pulse width from 250 ps to 500 ps together with the pulse separation from 500 ps to 1.1 ns.

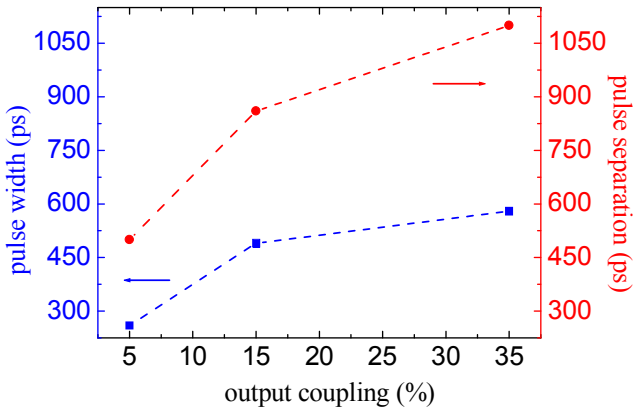

Figure 6.24. Pulse widths (blue square) and separations (red spot) with different output coupler

The measured pulse separations in Figure 6.22 and Figure 6.23 are longer than the cavity round trip time of 330 ps. It is therefore clear that the observed pulse trains are not due to mode-locking but instead are probably due to a passive Q-switching of the laser cavity. The evolution of a stable short pulse train of a passively mode-locked laser can only be achieved after several round trips of the pulse circulating

inside the resonator. For instance, a Rhodamine 6G laser requires at least 45 round trips to form the final 10 ps pulse from a noisy fluctuation background[26]. The excited state lifetime of the 2 mg/ml MEH-PPV solution is 500 ps, which is comparable to the cavity round trip time and at least ten times shorter than the lifetime of Rhodamine 6G. Therefore, only one round trip can be supported during the PL lifetime of MEH-PPV. The 8 ns pump pulse can compensate the short PL lifetime to support 22 round trips. Nevertheless, it could be still shorter than the required pulse build up time to achieve proper mode locking. To better understand the dynamics, in the next section a rate-equation model is used that could describe the passive Q-switching of the laser.

6.6. Simulation of output pulse with saturable absorber

The presence of the saturable absorber film in the laser cavity changed the output pulse from a single pulse of 2 ns width into a series of short pulses. A theoretical simulation based on a previous study of the transient behaviour of a dye laser cavity [27] was performed to model the temporal dynamics of the short pulses observed experimentally. The following rate equations can be used to describe the interaction between the photon densities inside the cavity and the populations in the gain medium and the saturable absorber.

$$\begin{aligned} \frac{dn}{dt} &= P(t) - c\sigma_e nq - \frac{n}{\tau} \\ \frac{dq}{dt} &= \frac{l}{L} c\sigma_e n(q+1) - \frac{q}{t_c} - c\sigma_s (N_{st} - n_s) q \frac{l_s}{L} \\ \frac{dn_s}{dt} &= c\sigma_s (N_{st} - n_s) q \frac{A}{A_s} - \frac{n_s}{t_s} \end{aligned} \qquad \textbf{6-11}$$

where n is the population inversion density in MEH-PPV, q is the photon density, n_s is population density in the upper state of the HIDCI doped polystyrene, τ is the PL lifetime of MEH-PPV, t_c is the cavity lifetime, t_s is the upper state lifetime of

HIDCI, L is cavity length of 50 mm, l and l_s are the lengths of the gain medium (5 mm) and the HIDCI thin film (8 μm), A and A_s are the areas of the cavity transverse modes in the gain medium and the HIDCI film, N_{st} is the number density of HIDCI molecules, σ_e is the stimulated cross-section of MEH-PPV, σ_s is the absorption cross-section of HIDCI, $P(t)$ is the pumping rate. The parameters used for the simulation are given in Table 6.V.

σ_s (10^{-16} cm^2)	σ_e (10^{-16} cm^2)[2]	t_c (ns)	τ (ns)	t_s (ns)	N_{st} (10^{-4} M/L)	A (μm^2)
2.5	4	0.6	0.5	0.3	5.6	210×500

Table 6.V. Parameters used for equation 6-11

In Table 6.V, σ_s was obtained from the simulation on the 1% w.t. saturable absorber in Table 6.III, cavity lifetime t_c was calculated by taking into account the 5% output coupling loss and the 4% reflection from the walls of the cuvette and the 20% non-saturating loss from the HIDCI thin film, t_s is from Table 6.I, τ was measured by streak camera, N_{st} was deduced from 1% w.t. HIDCI doped polystyrene blend, and A is based on the cavity simulation shown in Figure 6.14. The excitation pulse $P(t)$ can be assumed to have a Gaussian profile with a FWHM of 10 ns to simulate the OPO excitation used in the experiments:

$$P(t) = P_0 \exp[-4\ln 2(\frac{t-15}{T})^2] \qquad \textbf{6-12}$$

where T is the pulse width of 10 ns, and P_0 is taken to be 2.3 times above the lasing threshold, as used in experiments.

Figure 6.25 illustrates the simulated results from equation 6-11 for a range of different focussing condition in the saturable absorber.

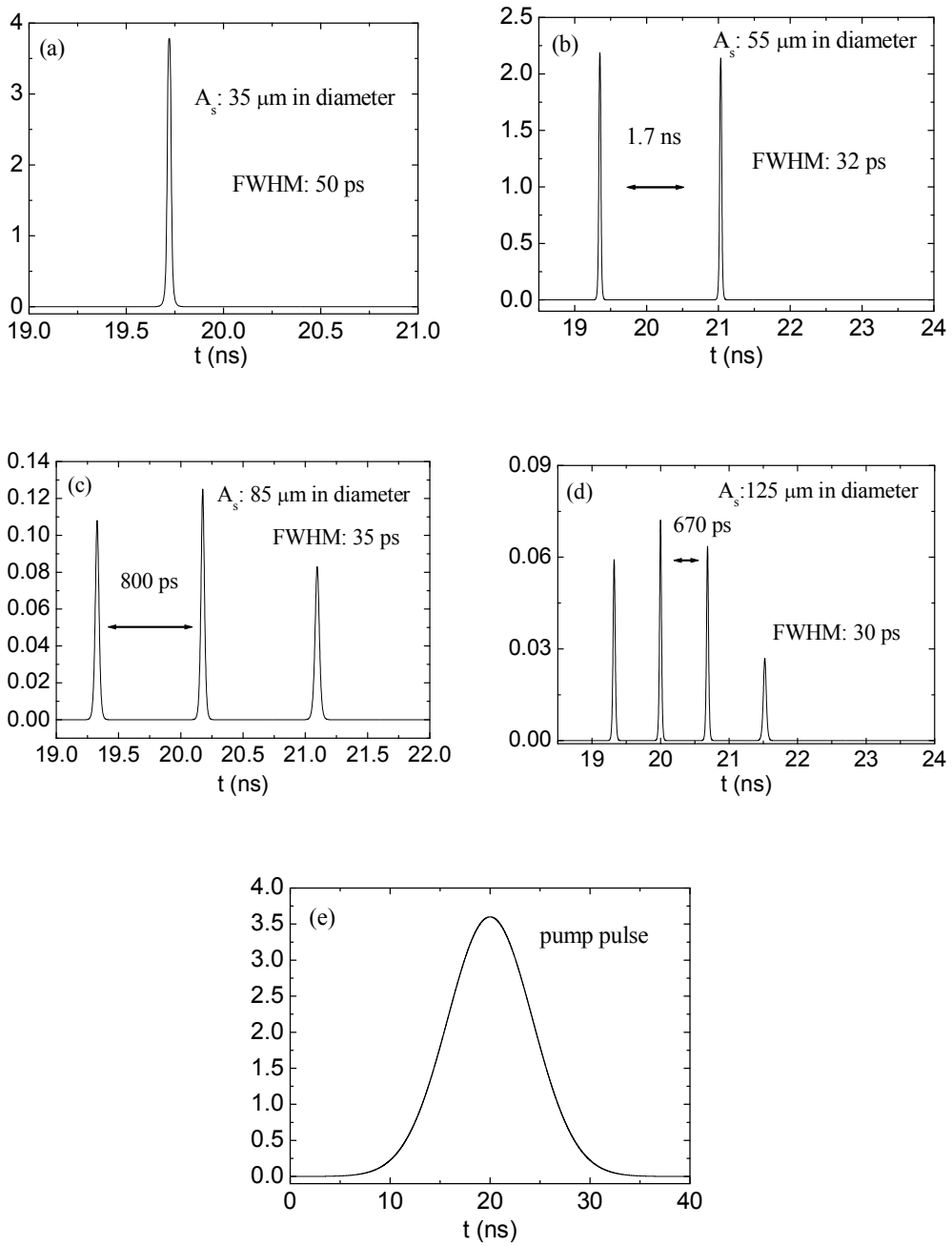

Figure 6.25. (a)-(d) Simulated output pulses for different A_s; (e) Pump pulse

The simulation predicts four different output pulse profiles from the cavity, similar to the different pulses measured experimentally in Figure 6.22. In Figure

6.25, as the laser field in the saturable absorber increased from 35 μm to 125 μm, the output changed from a single pulse of 50 ps duration to a string of four pulses of 30 ps duration, accompanied by a decrease in the output energy. In comparison to the results in Figure 6.22, the measured pulses are much wider than the simulated pulses, which is consistent with the time resolution (210 ps) of the fast photodiode. The measured pulse separations for the double pulse and the triple pulse output were about 500 ps. However, the simulated pulse separation reduced from 1.7 ns to 670 ns, when the number of the output pulses increased.

The comparisons between the experimental results and the rate-equation model suggest that the simulation agrees well with the experimental results qualitatively, although the quantitative repetition times do not exactly match. Additionally, the simulation implies the laser beam size on the saturable absorber is the reason for the different pulse trains obtained in the experiment which involved translating the saturable absorber around the focus inside the cavity. All these imply that very short pulses can be generated in polymer lasers using a Q-switching mechanism. In order to match the pulse widths and the pulse separations with experimental results, different cavity lifetime t_c, saturable absorber recovery time t_s, and intermediate values of A_s were put into the rate-equation model. However, no obvious matching has been found in the generated pulses so far.

6.7. Conclusion

In this chapter, a solid state saturable absorber has been included in an organic semiconductor laser cavity to investigate its influence on the laser output dynamics. The saturable absorber thin film was made from a HIDCI doped polystyrene blend. The impact of the dye concentration on the saturation intensity was examined in the range of 1% w.t. and 5% w.t. both experimentally and

theoretically. The experimental results corresponded well with the simulation. The increase of the dye concentration leaded to an increase in the saturation intensity with a shortening in the PL lifetime. The lowest saturation intensity achieved with the 1% w.t. blend was around 4 MW/cm^2. An organic SESAM made of a thin film of HIDCI coated on a Bragg mirror substrate was demonstrated to operate between 590 nm and 690 nm. A change in the reflection of 20% was observed, which could potentially be used as a low cost SESAM in passively mode-locked red lasers.

A solution organic semiconductor laser based on MEH-PPV was chosen to test the effect of the saturable absorber. The solution cuvette was placed in a 50 mm long Fabry-Perot cavity and transversely pumped by a stripe of 170 μm wide to match the internal cavity mode. To saturate the HIDCI film, a short focal length lens was used to concentrate the cavity mode into a small spot on the film. The existence of the saturable absorber increased the lasing threshold from 2.8 μJ to 3.3 μJ due to the additional refraction losses. Temporally, the saturable absorber changed the output pulse from a single 2 ns pulse to a string of pulses of 250 ps. Rate equations were explored to simulate the pulse dynamics in the cavity with the HIDCI saturable absorber. Qualitative agreement was observed between the simulation and experimental results. It is suggested that the laser beam size on the saturable absorber film could explain the different pulse dynamics obtained experimentally.

The demonstration of the impact of the saturable absorber thin film on the solution based MEH-PPV laser makes it promising for establishing passive mode-locking in organic semiconductor lasers, if optimization can be managed on absorption saturation intensity, pump pulse duration, and dispersions in the laser cavity. With simple fabrication, broad tunability and low cost, passively

mode-locked solid state organic semiconductor lasers could be the future high power light sources.

6.8. Reference

[1] Haiman.T.H., *Nature* 1960. **187**: p. 493.

[2] M. Goossens, A. Ruseckas, G.A. Turnbull, and I.D.W. Samuel, *Applied Physics Letters*, 2004. **85**(1): p. 31.

[3] M.S. Demokan, *mode-locking in solid-state and semiconductor lasers*. 1982, England: John Wiley & Sons Ltd.

[4] K. Smith, N. Langford, W. Sibbett, and J.R. Taylor, *Optics Letters*, 1985. **10**(11): p. 559.

[5] H. Vanherzeele, R. Torti, and J.C. Diels, *Journal of the Optical Society of America a-Optics Image Science and Vision*, 1984. **1**(12): p. 1256.

[6] W. Sibbett and J.R. Taylor, *Optics Communications*, 1982. **44**(2): p. 121.

[7] J.C. Mialocq and P. Goujon, *Applied Physics Letters*, 1978. **33**(9): p. 819.

[8] G. Heliotis, R. Xia, D.D.C. Bradley, G.A. Turnbull, I.D.W. Samuel, P. Andrew, and W.L. Barnes, *Applied Physics Letters*, 2003. **83**(11): p. 2118.

[9] N. Tessler, G.J. Denton, and R.H. Friend, *Nature*, 1996. **382**(6593): p. 695.

[10] S.V. Frolov, M. Shkunov, Z.V. Vardeny, and K. Yoshino, *Physical Review B*, 1997. **56**(8): p. R4363.

[11] I.D.W. Samuel and G.A. Turnbull, *Chemical Reviews*, 2007. **107**(4): p. 1272.

[12] P.M.W. French, M.D. Dawson, and J.R. Taylor, *Optics Communications*, 1986. **56**(6): p. 430.

[13] C. Scurtescu, Z.Y. Zhang, J. Alcock, R. Fedosejevs, M. Blumin, I. Saveliev, S. Yang, H. Ruda, and Y.Y. Tsui, *Applied Physics B-Lasers and Optics*, 2007. **87**(4): p.

671.

[14] W.B. Cho, A. Schmidt, J.H. Yim, S.Y. Choi, S. Lee, F. Rotermund, U. Griebner, G. Steinmeyer, V. Petrov, X. Mateos, M.C. Pujol, J.J. Carvajal, M. Aguilo, and F. Diaz, *Optics Express*, 2009. **17**(13): p. 11007.

[15] Q.L. Bao, H. Zhang, Y. Wang, Z.H. Ni, Y.L. Yan, Z.X. Shen, K.P. Loh, and D.Y. Tang, *Advanced Functional Materials*, 2009. **19**(19): p. 3077.

[16] N. Xiang, F. Lin, H.P. Li, H.F. Liu, W. Liu, W. Ji, and S.J. Chua, *Thin Solid Films*, 2007. **515**(10): p. 4484.

[17] O. Svelto and D.C. Hanna, *Principles of lasers*, ed. 4th. 1998: Springer.

[18] P.M.W. French, *Reports on Progress in Physics*, 1995. **58**(2): p. 169.

[19] P.G. Kryukov, *Quantum Electronics*, 2001. **31**(2): p. 95.

[20] E.P. Ippen, *Applied Physics B-Lasers and Optics*, 1994. **58**(3): p. 159.

[21] A. Finch, G. Chen, W. Sleat, and W. Sibbett, *Journal of Modern Optics*, 1988. **35**(3): p. 345.

[22] M. Maeda and Y. Miyazoe, *Japanese Journal of Applied Physics*, 1974. **13**(1): p. 193.

[23] S. Kirstein and S. Daehne, *International Journal of Photoenergy*, 2006: p. 20363.

[24] V.I. Avdeeva and B.I. Shapiro, *Doklady physical Chemistry*, 2003. **389**(1-3): p. 77.

[25] M. Haiml, R. Grange, and U. Keller, *Applied Physics B-Lasers and Optics*, 2004. **79**(3): p. 331.

[26] E.G. Arthurs, D.J. Bradley, and A.G. Roddie, *Applied Physics Letters*, 1973. **23**(2): p. 88.

[27] L. Zhu, *Optics Communications*, 1991. **84**(3-4): p. 155.

Chapter 7

Explosive Vapours Sensing with Organic Lasers

7.1. Introduction

Although the direct electrical excitation of organic lasers remains a big challenge at present [1], the reduction of laser threshold in the past few years significantly has reduced the size and cost of optical pump sources [2-3]. The demonstration of an LED pumped organic laser [4] and the potential improvement by incorporating a Luminescence Concentrator [5] make organic semiconductor lasers attractive in practical applications as compact, broadly tunable, low cost and disposable laser sources. Moreover, the possibility of increasing the peak power of organic lasers by mode locking makes them potential high power sub-picosecond sources. In the past few years, organic semiconductor lasers and amplifiers have been proven to be competent in spectroscopy [6], data communication [7], optical switching [8-9] and chemical sensing [10-11]. This chapter will focus on the capability of organic lasers as sensitive chemosensors.

Sensors for explosive vapours are important in terms of environmental applications, national security and human health protection. Rose et al [11] have shown that an organic microring laser made from a PPV derivative can be used to detect 2,4-dinitrotoluene (DNT) vapour. Recently, fluorene-based dendrimer lasers have

been successfully used as nitro-aromatic vapour sensors [12]. However, both the gain media of these lasers are custom-synthesized and therefore come with a high price and low availability in the market. In this chapter, the widely available prototypical polymer polyfluorene combined with the convenient distributed feedback (DFB) resonator will be tested as chemosensors for nitro-aromatics based explosive analytes. Polyfluorene has been demonstrated to be an attractive laser medium with high gain, low loss and high PLQY. Combined with distributed feedback resonators, polyfluorene lasers exhibit low lasing thresholds and broad tunability in the blue spectral range [13-15]. To use polyfluorene DFB lasers in chemosensing, not only the laser characteristics (e.g. threshold) but also the output dynamics is explored in this chapter.

A background theory of using organic semiconductors to detect explosive vapour is introduced in **Section 7.2**, followed by a description of the experimental design in **Section 7.3** which allows in-situ monitoring the change in emission intensity during exposure to the explosive vapours. In **Section 7.4**, a comparison of laser characteristics, including the laser threshold and slope efficiency, has been made between the pre-exposure laser and the exposed laser. Also, the sensing efficiency is introduced to describe the sensitivity of the laser. **Section 7.5** investigates the dynamics in the laser output during exposure and recovery process. To improve the understanding of the interaction between the analyte and the polymer, a model is developed in **Section 7.6** to simulate the diffusion of the analytes into the polymer layer.

7.2. Background theory

Organic semiconductors are good candidates for explosive vapour detection because of their capabilities as electron donors to the nitroarmoatics based explosive vapour molecules [16-19]. The mechanism for explosive detection is based on fluorescence quenching of the emission from organic semiconductors[20]. A simple diagram is depicted in Figure 7.1.

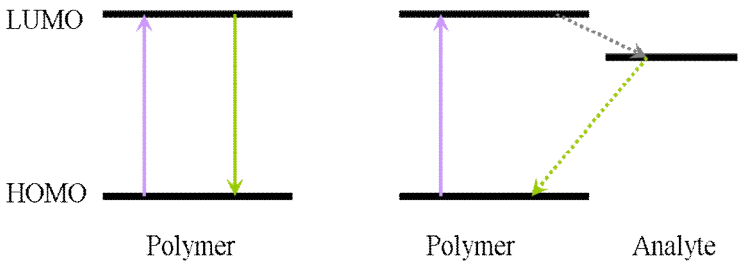

Figure 7.1. Explosive sensing mechanism

(Left) energy states in organic semiconductor; (Right) Organic semiconductor-analyte

The presence of electron-withdrawing nitro groups on the aromatic rings in the analyte molecules lowers the energy of the empty π orbital. Therefore, they can insert energy states in between the HOMO and LUMO states of organic semiconductors. These additional energy states function as electron acceptors to organic semiconductors. Fluorescent quenching occurs through the donor-acceptor electron transfer mechanism. As described in the left of Figure 7.1, in organic semiconductors, electrons in the HOMO level can be excited to the LUMO level by absorbing a photon to form excitons. In absence of the analyte states, the excitons decay to the ground state radiatively and give fluorescence emission. However, the present of the analyte states, as shown in the right of Figure 7.1, provides an additional non-radiative pathway (represented by the dotted line) through which excitons can be dissociated with electrons transferring from the LUMO state to the quencher state. In other words, organic semiconductors act as electron donors and the analytes act as electron acceptors. Electrons in the analyte state can transfer

back to the HOMO state via another non-radiative decay. Hence, the analyte molecules can quench the fluorescence from organic semiconductors.

In comparison to other fluorescent chemosensors, organic semiconductors usually have high detection sensitivity up to a few parts per billion or even parts per trillion due to their unique delocalized π excited states. The delocalized excited states allow excitons to diffuse along the molecular backbone. Hence, the probability of an exciton to meet a bounded analyte quencher is significantly increased, compared to a bounded electron. In the past decades, apart from spontaneous fluorescence, stimulated emission in organic thin films and lasers have been demonstrated to be effective and even more sensitive in chemosensing[21-22].

7.3. Experimental setup

The nitroaromatics based analyte examined in this chapter is 1,4-dinitrobenzene (DNB). It is strongly electronegative and has low equilibrium vapour pressure of 30 ppb at 25°C. The molecular structure is shown in Figure 7.2.

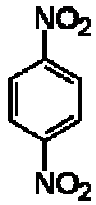

Figure 7.2. Molecular structure of 1,4-dinitrobenzene

As for the organic semiconductor laser, a 260 nm thick poly9,9-dioctylfluorene (PFO) film was spin coated from a 25 mg/ml solution in chloroform onto a one-dimensional corrugated silica substrate to make a surface emitting 1D DFB laser. The grating period used was chosen to be 268 nm to support a lasing wavelength at 450 nm, close to the ASE peak of PFO. The laser was pumped by a nitrogen laser at 337 nm with 500 ps pulse at 10 Hz repetition rate.

A comparison of the sensing efficiency has been made between PFO lasers and fluorescence thin films. The excitation source to generate fluorescence from PFO thin films was a PicoQuant laser diode with emission at 390 nm running at 80 MHz repetition rate to give a quasi-CW excitation. To detect the explosive analyte, the PFO laser or thin film was placed in a specially designed vacuum chamber which allows the continuous flow of the analyte vapour. Simultaneously, the emission spectra can be recorded by a fibre-coupled CCD spectrograph to reveal the emission dynamics during detection. A detailed sketch of the experimental setup is given in Figure 7.3.

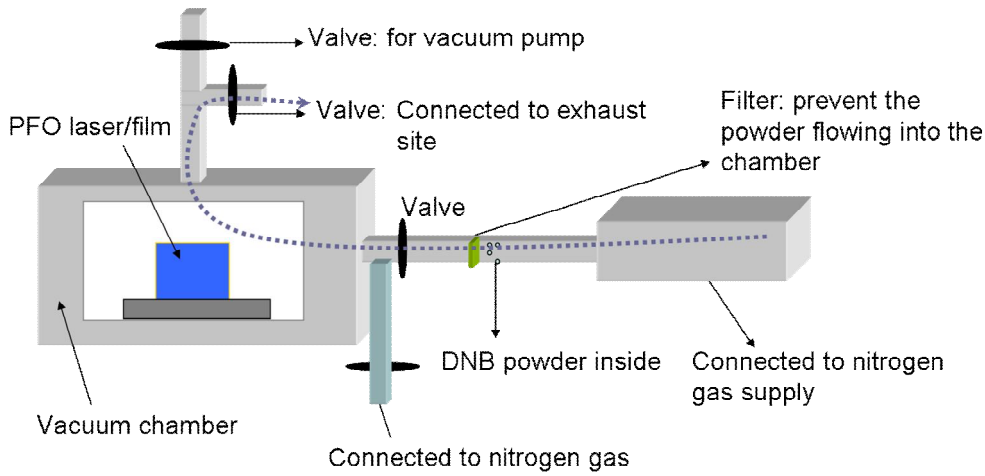

Figure 7.3. Vacuum chamber design for explosive vapour sensing

To perform an exposure, the PFO laser or thin film was placed inside the chamber which was connected to a vacuum pump. The DNB vapour supply and exhaust were controlled by separate valves. Initially, the chamber was pumped down to 10^{-4} mbar to remove atmospheric oxygen. DNB powder was placed in a glass tube connected to a nitrogen gas supply whose pressure can be adjusted by a gas valve. The flow of the nitrogen gas can bring the DNB vapour into the chamber. A filter of grade 3 porosity (pore size: 16 μm-40 μm) was placed in the middle of the glass tube to prevent the DNB powder flowing into the vacuum chamber. In the exposure process, the port connected to the vacuum pump was closed with the other

two ports open to circulate the DNB vapours through the chamber, represented by the dotted lines in Figure 7.3 (with arrows showing the flow direction). The typical exposure time was 5 minutes. A fibre-coupled CCD spectrograph was used to record the output spectra of the laser in steps of between 3 seconds and 45 seconds.

To remove the DNB vapour, the ports connected to the DNB vapour and the exhaust were closed. Three different recovery environments were investigated: using vacuum, flowing clean nitrogen gas across the sample, and immersion in clean air. When the recovery was realized in vacuum, the port connected to the vacuum pump was turned on to extract DNB molecules from the chamber. In the second case, an extra port, represented by the cyan bar in Figure 7.3, was turned on to allow clean nitrogen gas to flow into the chamber with a similar flow rate as used in the exposure process. For recovery in air, the whole chamber was removed and the film was left in air unattended.

The pressure of the DNB vapours used during exposure can be determined from fluorescence quenching of the PFO thin films, according to the following equation [17]:

$$F_Q \sim V_P[\exp(-\Delta G)^2]K_b \qquad \textbf{7-1}$$

F_Q is the fluorescence quenching per unit time, V_P is the vapour pressure of the DNB analytes, ΔG is the exergonicity energy and K_b is the binding strength between the analyte molecules and the polymer. For the polymer films of identical thickness and exposed to the same analyte for the same amount of time, F_Q is proportional to the analyte vapour pressure V_P. Therefore, to determine the DNB vapour pressure used in the flowing exposure, the fluorescence quenching of the thin film exposed under experimental condition stated above was compared with

that exposed in equilibrium vapour pressure for the same exposure duration of 5 minutes. The results showed that the fluorescence quenching under flowing DNB vapours is 3.3 times lower than that under equilibrium conditions. Consequently, it can be deduced that the vapour pressure of the flowing DNB is 9.8 ppb, when the equilibrium vapour pressure is taken to be 30 ppb at 25 ^{0}C [17].

7.4. Lasing threshold and slope efficiency change

From Figure 7.1, as fluorescent quenchers, the DNB vapours are expected to have an impact on the laser performance. Figure 7.4 compares the laser thresholds between a pre-exposure laser, a five-minute exposed laser and a recovered laser achieved by evacuating the chamber.

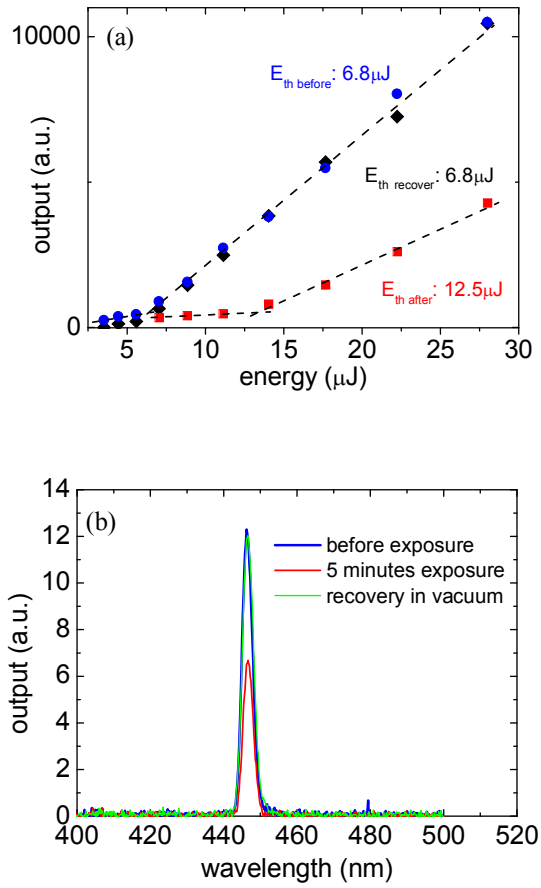

Figure 7.4. Comparison of laser thresholds before and after 5 minute exposure:

(a) Input vs Output plot; (b) Lasing spectra.

Figure 7.4 (a) gives the input vs output of the PFO laser before exposure (blue circles), after five-minute exposure (red squares) and recovery in vacuum (black squares). The corresponding lasing spectra of these three lasers were plotted in Figure 7.4 (b) at a constant pumping energy of 28 μJ/pulse. Before exposure, the laser threshold was 6.8 μJ/pulse. A five-minute exposure to the circulating DNB vapours increased the threshold by a factor of 1.8 to 12.5 μJ/pulse. The bound DNB quenchers on the PFO backbond reduced the gain and hence increased the lasing threshold. Correspondingly, the output spectrum of the exposed laser in Figure 7.4 (b) exhibited a decrease in the lasing peak, in comparison to that of the pre-exposure laser. In addition to the change in the laser threshold, DNB molecules also have an impact on the slope efficiency. The input vs output plots indicate the slope efficiency was reduced by a factor of 3 after exposure to DNB vapours, which means that the presence of the DNB molecules not only serves as quenchers for excitons, but could also change the output coupling losses of the DFB laser resonator. Both the changes in the lasing threshold and the slope efficiency could be used as robust multipoint measurements for sensitive detections.

The changes in the laser threshold and slope efficiency are reversible, once the DNB molecules are removed from the PFO laser. In Figure 7.4, when the DNB molecules were extracted from the chamber by a vacuum pump, the laser threshold resumed to its original value of 6.8 μJ/pulse with its output spectrum recovering completely.

The change in the output emission can be described by a “sensing efficiency”, defined as the change in the intensity of the emission after exposure divided by the original emission intensity. The sensing efficiency of the PFO laser depends

strongly on the excitation energy. Figure 7.5 presents the sensing efficiencies obtained from Figure 7.4 at different pump energies.

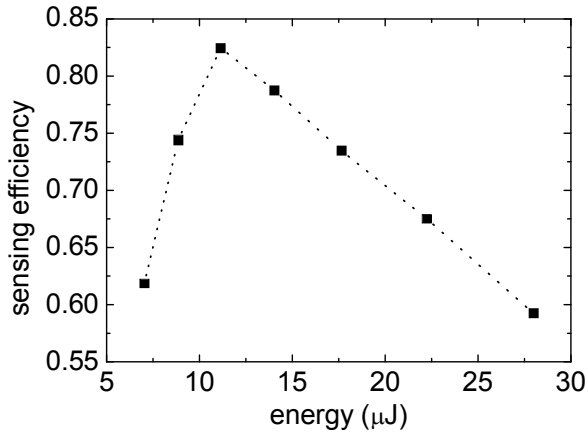

Figure 7.5. Sensing efficiencies at different pump energies

The sensing efficiency increased with the pump energy from 62% to a maximum value of 82% which occurred when the pump energy was close to the threshold of the exposed-laser at 12 μJ/pulse, followed by a drop as the pump energy continuously increased to 26 μJ/pulse. The pump dependent sensing efficiency suggests that the PFO laser is most sensitive when it is pumped at the threshold of the exposed laser.

A comparison has been made on the sensing efficiency between PFO lasers and planar films of identical film thickness and exposed to the same concentration of DNB vapours. The dependence of the sensing efficiency of planar thin films on pump energy is shown in Figure 7.6. Unlike PFO lasers, the sensing efficiency of the planar film fluctuated at 68% as the pump energy changed. Compared to the maximum sensing efficiency of the PFO laser, the fluorescent sensing efficiency is 1.2 times lower.

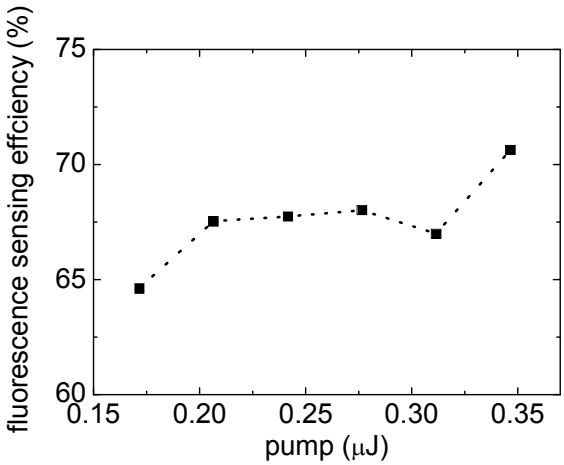

Figure 7.6. Fluorescent sensing efficiency of PFO planar film

The influence of the pump energy on the sensing efficiency of PFO lasers can be explained by means of a four-level energy laser system [11]. In the steady state, when the laser is pumped (I_{pump}) below threshold, the fluorescence output is spontaneous emission and proportional to the radiative decay rate:

$$I_{film} = BI_{pump} \frac{\frac{1}{\tau_{sp}}}{\frac{1}{\tau}} = BI_{pump} \frac{\tau}{\tau_{sp}} \qquad \textbf{7-2}$$

B is a constant related to spontaneous emission, τ_{sp} is the radiative lifetime and τ is measured upper state lifetime including non-radiative decay. When the DNB quencher states are introduced into the polymer states, the upper state lifetime τ is reduced to τ' through the non-radiative decay paths with electron transferring from polymer to quencher states. With the quenching factor q used to describe this effect, the spontaneous fluorescence intensity from an exposed film is

$$I'_{film} = BI_{pump} \frac{\frac{1}{\tau_{sp}}}{\frac{1}{\tau'}} = BI_{pump} \frac{\tau'}{\tau_{sp}},$$

with $\frac{\tau}{\tau'} = q$ **7-3**

When the pump energy is lower than the threshold of the pre-exposed laser (I_{th}), $I_{pump} < I_{th} < I'_{th}$, the pre-exposed and exposed lasers should give spontaneous emission governed by equation 7-2 and 7-3 respectively. The sensing efficiency can be written as:

$$\eta = \frac{BI_{pump}(\frac{\tau}{\tau_{sp}} - \frac{\tau'}{\tau_{sp}})}{BI_{pump}\frac{\tau}{\tau_{sp}}} = 1 - \frac{1}{q} \quad \textbf{7-4}$$

Equation 7-4 indicates the sensing efficiency of spontaneous emission is only determined by the quenching factor and independent of the pump energy. It corresponds well with the results demonstrated in Figure 7.6 for fluorescent thin films.

When the pump energy is in between the threshold of the pre-exposed and exposed laser, $I_{th} < I_{pump} < I'_{th}$, stimulated emission occurs in the pre-exposed laser, while the exposed laser still only shows spontaneous emission.

The small round trip gain $\gamma(\lambda)$ can be represented by the following equations:

$$\gamma(\lambda) = N_{th}\sigma(\lambda)$$

$$N_{th} = R_{th}\tau \quad \textbf{7-5}$$

where N_{th} is the threshold population inversion; $\sigma(\lambda)$ is stimulated emission cross section at the lasing wavelength; R_{th} is the pumping rate at threshold. By substituting the second equation into the first one in equation 7-5, the threshold round trip gain is:

$$\gamma(\lambda) = R_{th}\tau\sigma(\lambda) \quad \textbf{7-6}$$

At threshold, the round trip gain should be equal to the cavity loss β .

$$R_{th}\tau\sigma(\lambda) = \frac{\beta}{d} \quad \textbf{7-7}$$

Where d is the cavity round trip length. Therefore, the threshold pump energy is inversely proportional to the upper state lifetime:

$$R_{th} = \frac{\beta}{d\tau\sigma(\lambda)} \quad \textbf{7-8}$$

The quencher states tend to shorten the upper state lifetime through additional non-radiative decay. Based on equation 7-8, the required threshold pumping rate for the exposed laser should be increased, even if the impact of the analyte quenchers on the output coupling efficiency is assumed negligible. Similar to equation 7-3, the laser threshold of an exposed laser can be described with q:

$$R_{th}^{'} = qR_{th} \quad \textbf{7-9}$$

When the laser is above threshold, the output intensity should be proportional to the pump intensity, assuming the laser emission is much stronger than the spontaneous emission:

$$I_{laser} = A(I_{pump} - I_{th}) \quad \textbf{7-10}$$

A is a constant related to the cavity output coupling. When $I_{th} < I_{pump} < I_{th}^{'}$, the sensing efficiency can be described as:

$$\eta = \frac{I_{laser} - I_{laser}^{'}}{I_{laser}} = 1 - \frac{BI_{pump}\frac{\tau^{'}}{\tau_{sp}}}{A(I_{pump} - I_{th})} \quad \textbf{7-11}$$

Hence, the sensing efficiency depends on the pump energy. As the pump energy increases, the sensing efficiency increases accordingly, since $\frac{\partial \eta}{\partial (I_{pump})} > 0$ in the region $I_{th} < I_{pump} < I_{th}^{'}$. This agrees with the efficiencies in Figure 7.5 between 6 μJ and 11 μJ.

When the pump energy increases further to the region of $I_{pump} > I_{th}^{'}$, both pre-exposed and exposed laser are pumped above threshold. So, the sensing efficiency becomes:

$$\eta = \frac{I_{laser} - I_{laser}^{'}}{I_{laser}} = \frac{I_{th}^{'} - I_{th}}{I_{pump} - I_{th}} = \frac{(q-1)I_{th}}{I_{pump} - I_{th}} \qquad \textbf{7-12}$$

From equation 7-12, the increase of the pump energy leads to a reduction in the sensing efficiency. Combined with the result in equation 7-11, the maximum sensing efficiency is achieved, when the pump energy equals to the threshold of the exposed laser. Ideally, the maximum sensing efficiency η can approach 100%, when $I_{pump} = qI_{th}$ is substituted into equation 7-12. However, the maximum sensing efficiency measured in Figure 7.5 is 85%. The 15% difference could arise from the shallow penetration depth of the DNB analytes, which will be discussed later.

7.5. Exposure Dynamics

The change in the laser characteristics in **Section 7.4** successfully demonstrated the PFO lasers are suitable chemosensors for nitro-aromatics based explosive vapours. However, the information of how fast the analyte molecules can quench the PFO laser remains unclear. Such quenching details haven't been published in any organic semiconductor laser based chemosensors. This information is

extremely important in terms of applications. For instance, security check points in the airports usually require a fast and sensitive response to the explosive analytes.

One advantage of the chamber design in Figure 7.3 is to allow for directly monitoring the dynamics of the laser emission during exposure and recovery process by recording the output spectra. Figure 7.7 (a) presents the changes in laser output in two cycles of exposure to DNB vapours and recovery in vacuum. The details of the second exposure are shown separately in Figure 7.7 (b). The laser was pumped at three times the threshold of the pre-exposed laser, showing a sensing efficiency of 68%.

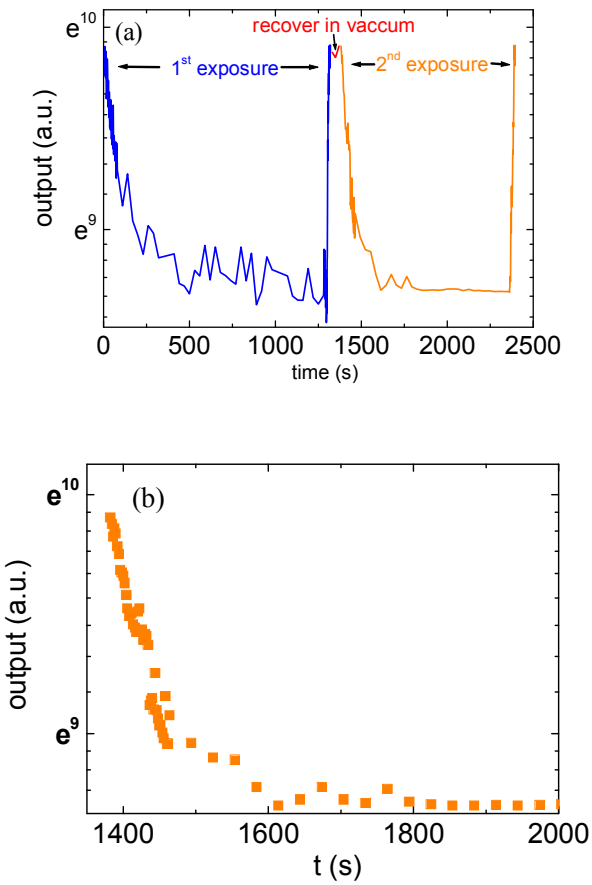

Figure 7.7. (a) Two exposure and recovery cycles of the PFO laser; (b) Details of the second exposure

In graph (a), for each exposure-recovery cycle, the laser emission can recover back to its original state, as demonstrated in Figure 7.4. The similar trend in the two dynamics cycles proves the exposure-recovery process is repeatable. As for the details of the exposure process, in graph (b), the output emission decreased rapidly by 36% (1/e) within 65 seconds with an initial 13% drop in the first 10 seconds. Prolonged exposure to DNB molecules beyond 300 seconds causes very little further change in the emission. A possible explanation for the flattening of the curve following a fast decay could be that most of the excitons near the surface of the PFO film were quenched as soon as the DNB molecules reached the surface of the film. Further quenching dynamics depends on the diffusion of DNB molecules deep into the PFO films and it is likely to be slower than the surface exciton quenching. The diffusion speed of the explosive vapour molecules into the polymer film is determined by several parameters such as the explosive vapour pressure, the size of the vapour molecules and the packing of the polymer chains [17]. For example, higher vapour pressure could bring more analyte molecules per unit space. So the probability of the excitons meeting the quenchers is higher and the quenching process is sped up accordingly. In addition, it is easier for small vapour molecules to penetrate into polymers with large space between chains. It was observed that with the exposure duration extended from 5 minutes to two hours, the PFO laser can still lase. Therefore, it is likely that excitons deep in the PFO film could still give radiative decay with a modest concentration of quenchers, due to the limited exciton diffusion length of 5 nm for polyfluorene [23-24]. More details of the diffusion of DNB into PFO will be discussed in **Section 7.6**.

How the DNB molecules are removed has a strong impact on the recovery dynamics. In all the three recovery approaches, the lasers were pumped at three times above the threshold of the pre-exposed laser. In Figure 7.7, when the DNB

molecules were removed from the chamber under a vacuum of 10^{-4} mbar, the PFO laser can recover fully within 20 seconds. Flowing clean nitrogen gas with similar pressure as used in the exposure process prolonged the recovery time, as plotted in Figure 7.8.

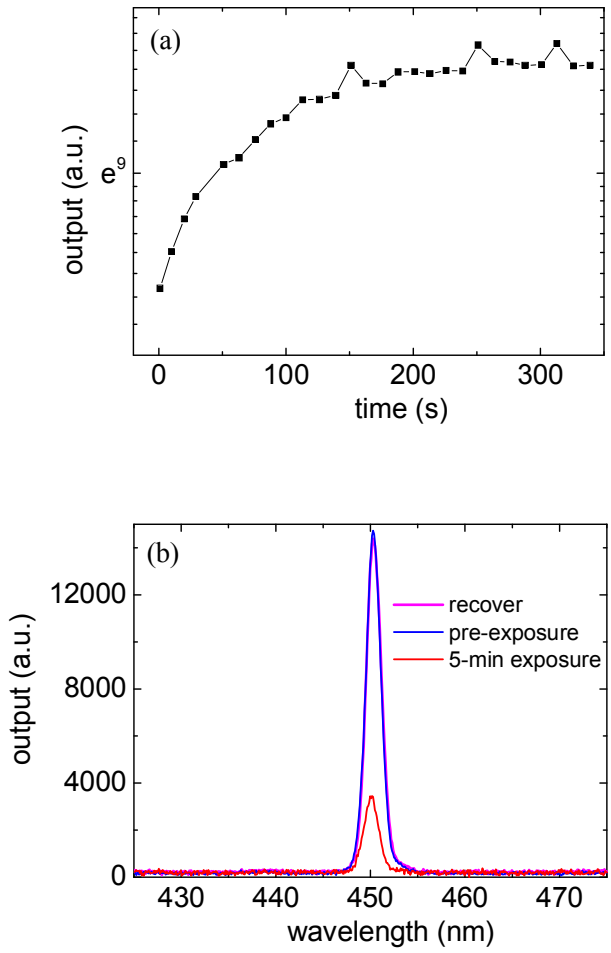

Figure 7.8. (a) Nitrogen gas recovery;

(b) Spectra of pre-exposure, recovery and 5-min exposure lasers

From the three emission spectra in Figure 7.8 (b), the PFO laser recovered completely with no degradation observed, which is similar to the case in vacuum recovery. The dynamics from graph (a) indicates that the laser recovered to within 1/e (36%) of the original value in 32 s and full recovery can be realized in 200 s. Both time scales are comparable to the exposure process shown in Figure 7.7.

The capability for the PFO laser to recover in air was also tested. This recovery approach could significantly reduce the cost and complexity of the system by getting rid of the vacuum pump or nitrogen gas supply. Prior to examining the recovery dynamics, the degradation of the PFO laser was measured to find out how fast the emission decays in ambient atmosphere, because PFO lasers, as other organic semiconductor lasers, are sensitive to oxygen and water. However, the measurement is different from the lifetime measurement of the ADS 233 YE laser in **Chapter** 4. The PFO laser was not encapsulated because the PFO layer needs to be exposed to DNB molecules. To measure the degradation, the PFO laser was not continuously pumped. Instead, it was only pumped when the output spectrum was taken. Otherwise, it was left in air. In this case, the degradation could be much slower than the continuously pumped situation and the measured lifetime could be much longer. This pumping scheme is reasonable in practice, since the laser only requires excitation when checking the recovery. As indicated Figure 7.9, the output of the PFO laser only decreased by 4% within the first 1000 minutes. The slightly flattening of the curve beyond 400 minutes could be due to the fewer measurement points in comparison to the first 200 minutes.

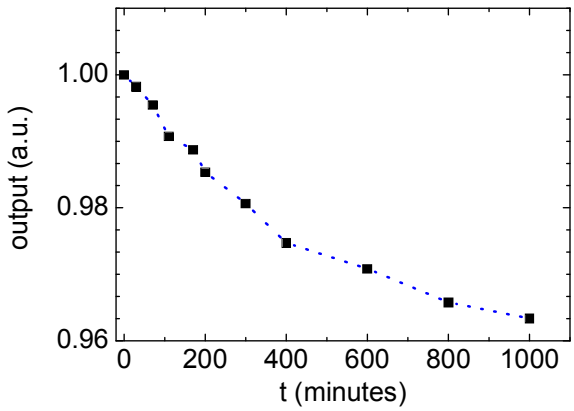

Figure 7.9. Degradation of PFO laser in air

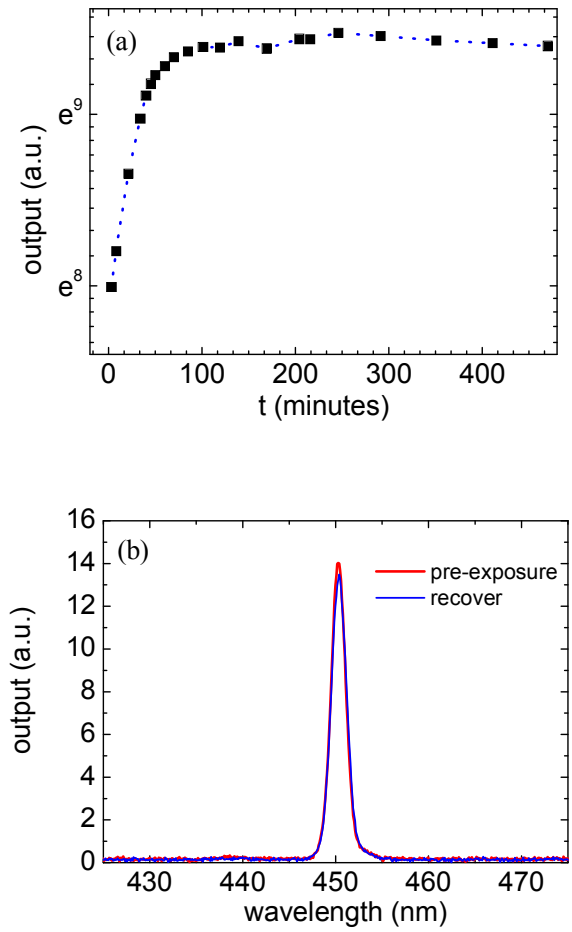

Figure 7.10. (a) Recovery dynamics in air; (b) Pre-exposure and recover output spectra

Figure 7.10 shows the recovery dynamics of the PFO laser in air. It took 34 minutes to recover to 1/e (36%) of the original performance, 23 times longer than the nitrogen recovery. Beyond 230 minutes, the output shows a reduction which could be the result of oxidation and photodegradation of the laser expected from Figure 7.9. The recovery spectrum in Figure 7.10 was taken after 210 minutes where the peak of the recovery dynamics curve lied in graph (a). The spectrum suggests that the laser can achieve 97% recovery. The 3% loss is comparable to the degradation results shown in Figure 7.9. Table 7.I summarizes the recovery dynamics for all these three situations discussed above:

	Recover by 1/e	Full recovery
Vacuum	6 seconds	20 seconds (100%)
Nitrogen	88 seconds	200 seconds (100%)
Air	34 minutes	210 minutes (97%)

Table 7.I. Summary of the recovery approaches

It is clear that the more aggressive the removal of the analyte molecules, the shorter the recovery takes. All these three approaches can achieve close to 100% recovery in a relative short period, indicating that one PFO laser is capable of many detection cycles. The fast response and recovery makes PFO lasers promising chemical sensors in practical applications.

7.6. The diffusion of DNB molecules in the PFO layer

The diffusion of DNB molecules into the PFO layer is important to the sensing efficiencies and output dynamics shown in the previous sections. The deeper the analytes can diffuse into the polymer layer, the higher will be the sensing efficiency, since more excitons deep inside the polymer can be quenched.

A simple model was developed to determine how far the DNB can penetrate into the PFO film during the five-minute exposure. In this model, it is assumed that the DNB molecules have uniform concentrations up to a particular penetration depth from the PFO film surface. The PFO film is divided into two regions by the penetration depth of the DNB molecules as shown in Figure 7.11.

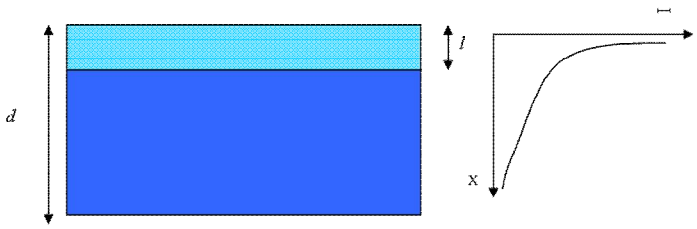

Figure 7.11. Sketch of the square diffusion model

In the figure, the PFO film thickness is *d*. The penetration depth of the DNB molecules is represented by *l*. Within the distance *l*, the concentration of the DNB molecules is constant and independent of the distance away from the surface. The excitons lying in the region from the surface to depth *l* have a possibility of being quenched by the explosive analytes via non-radiative decay mechanisms described in **Section 7.2**. The quenching can be evaluated by a quenching factor *Q*, defined as the fraction of the emission being quenched compared to the pre-exposure emission. Excitons outside this region in the deep blue rectangle are not affected, giving emission limited by the normal PLQY of the polymer (55% for PFO). The *I* vs *x* curve on the right indicates the variation of exciton density in the film due to the absorption of pump photons according to the Beer-Lambert Law. The explosive analytes can affect only emission but not absorption.

The volume-integrated fluorescence from the pre-exposed and the exposed film can be described by equation 7-13 and equation 7-14 respectively:

$$I_{before} = AP[1-\exp(-\alpha d)] \qquad \textbf{7-13}$$

$$I_{after} = AP(1-Q)[1-\exp(-\alpha l)] + AP[\exp(-\alpha l) - \exp(-\alpha d)] \qquad \textbf{7-14}$$

I_{before} is the pre-exposure emission intensity and I_{after} is the emission intensity after five-minute exposure. *A* is a constant relating the pump beam intensity *P* and the fluorescence output intensity *I*. α is the absorption coefficient at the pump

wavelength. Equations 7-13 and equation 7-14 can be used to calculate the fluorescence sensing efficiency η:

$$\eta = 1 - \frac{I_{after}}{I_{before}} = Q\frac{1-\exp(-\alpha l)}{1-\exp(-\alpha d)} \qquad \textbf{7-15}$$

In equation 7-15, the two unknown parameters, penetration depth l and quenching factor Q, can be deduced by knowing the sensing efficiencies η from measurements on a range of PFO films of different thickness.

Experiments were setup as described in **Section 7.3** to measure the sensing efficiencies η for a series of PFO thin films on flat silica substrates with thickness ranging from 30 nm to 300 nm. The corresponding results were plotted as black squares in Figure 7.12. The two simulation curves, represented by the two dashed lines, were generated based on equation 7-15 with l and Q being the fitting parameters. In the simulation, the assumed penetration depth l was used to calculate the theoretical sensing efficiency when the sample film thickness d is larger than l, otherwise l was equal to d in the calculation for thinner films which are completed occupied by analyte molecules.

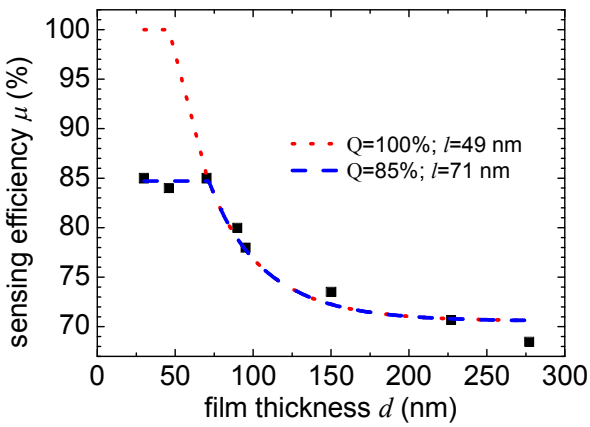

Figure 7.12. Fitting of the sensing efficiency for different film thickness: (blue) Q=85%; (red): Q=100%

The experimental data shows that the sensing efficiency increased as the PFO film thickness was reduced. Generally, thin films give a larger sensing efficiency than thick films, since a larger fraction of the polymer can interact with quenchers of identical densities in thinner films than in thicker films and thus more excitons can be quenched. When Q = 100% and the optimized penetration depth was 48 nm, the red curve fits well for films thicker than 70 nm and diverged for thinner films. 100% quenching requires the sensing efficiency to reach 100% for films thinner than 48 nm, because all the excitons lying within the penetration depth are quenched and there should be no output emission. However, this is different from what is observed from measurement. In the experiment, films thinner than 49 nm still give output emission after exposure, indicating the sensing efficiency must be lower than 100%. When partial quenching was assumed (Q<100%), an optimum fit (blue curve) for all film thicknesses can be generated with Q = 85% and a DNB penetration depth of 71 nm. 85% quenching suggests that the PFO films can still give 15% of their original emission in the presence of the DNB quenchers, agreeing well with the experimental results. One possible origin for partial quenching could be that excitons created outside the exciton diffusion range to a DNB quencher cannot interact with the quencher and thereby cannot be quenched.

7.7. Confinement factor

As shown in **Section 7.4**, the presence of DNB quenchers brought a change in both laser thresholds and slope efficiencies of PFO DFB lasers. In this section, the DNB diffusion profiles obtained in **Section 7.6** will be applied to predict the impact of these quenchers on the laser properties, since how the DNB molecules distribute through the gain layer can modify the exciton distribution and hence changes the lasing threshold.

In laser physics, a confinement factor is usually used to describe the fraction of the gain overlapping with the cavity modes. With other cavity losses (e.g. scattering, reabsorption and output coupling loss) unchanged, the higher the confinement factor is, the better overlap of the specific cavity mode with the gain

medium and the lower the lasing threshold will be. The confinement factor is inversely proportional to the laser threshold R_{th}.

Mathematically, for a waveguide laser such as a DFB laser, the confinement factor Γ is defined as the overlap between the optical transverse mode of the waveguide and the population inversion distribution by the following equation, when a planar substrate is assumed [25]:

$$\frac{1}{R_{th}} \sim \Gamma = \frac{\int_{x=0}^{d} E^2(z)\exp(-2\alpha_p z)dz}{\int_{\infty} E^2(z)dx} \qquad \textbf{7-16}$$

A schematic waveguide structure corresponding to equation 7-16 is plotted in Figure 7.13. $E(z)$ is represented by the red dotted curve and is the amplitude profile of the waveguided transverse mode which can be obtained by solving the Helmholtz equations of a planar waveguide. The distribution of the population inversion is related to the change of the pump beam intensity throughout the PFO waveguide layer of d (purple dashed curve). The presence of the DNB quenchers is plotted as the grey region inside the PFO layer. The bottom graph illustrates the refractive indices for different regions in the above graph separated by the dotted vertical boundaries.

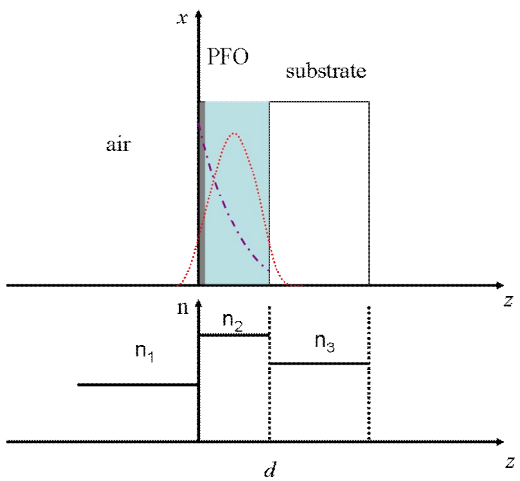

Figure 7.13. Cavity mode (top) and refractive indices (bottom) used in equation 7-16

The change of the lasing threshold can therefore be calculated from:

$$\eta = \frac{I_{th}^{'} - I_{th}}{I_{th}} = \frac{\Gamma_{pre}}{\Gamma_x} - 1 \qquad \textbf{7-17}$$

I'_{th}, I_{th} are the threshold of the exposed and pre-exposed lasers. Γ_x and Γ_{pre} are the confinement factors after exposure and before exposure.

The presence of the DNB molecules changes the distribution of the excitons by introducing quenchers and thus has an impact on the laser threshold, shown by the modified confinement factor which includes the quenching efficiency Q (z):

$$\Gamma = \frac{\int_0^d E^2(z)[1-Q(z)]\exp(-2\alpha_p z)dz}{\int_\infty E^2(z)dz} \qquad \textbf{7-18}$$

From the theoretical simulation in **Section 7.6**, Q (z) is a constant of 85% for the quenched region (grey region in Figure 7.13). The integral in the denominator of equation 7-18 can be divided into two parts by the diffusion frontier of the quencher:

$$\Gamma_{square} = \frac{\int_0^l E^2(z)\exp(-2\alpha_p z)dz + (1-0.85)\int_l^d E^2(z)\exp(-2\alpha_p z)dz}{\int_\infty E^2(z)dz} \qquad \textbf{7-19}$$

The diffusion length l is 71 nm from the best fit in Figure 7.12. The confinement factor before exposure was calculated to be 76%. After five-minute exposure, it decreased to 36% due to the quenchers which reduced the effective overlap between the cavity modes and excitons. Based on equation 7-17, the fractional threshold change η was calculated to be 2.1. Experimentally, in Figure 7.4, the laser threshold increased by a factor of 1.8 after exposure to the DNB vapour, close to the prediction value of 2.1. The good agreement between the theoretical

prediction and experimental results indicates the square diffusion profile from the simple model could be more or less correct. Recently, neutron scattering measurements of nitro-aromatic diffusion in dendrimer films also suggests a similar square diffuser profile [27]. The square diffusion profile is similar to what is observed in a case II diffusion [26], which is usually characterized by a sharply defined boundary separating the swollen, rubbery outer layer (behind the diffusion front) and the glassy interior (ahead of the diffusion front). In the outer layer, the diffuser concentration is almost uniform and the front advances into the glassy polymer linearly at constant speed.

7.8. Conclusion

In this chapter, the suitability of using organic semiconductor lasers as chemosensers for detecting nitro-aromatics based explosive vapours is discussed. Polyfluorene (PFO) based 1D DFB laser has been demonstrated to be an excellent sensor for low vapour pressure detection of DNB analyte at 9.8 ppb. The convenient DFB laser geometry gives larger response to the DNB molecules than the fluorescence thin films of the same film thickness. Acting as additional quencher centres, the presence of the DNB analytes reversibly deteriorate the performance of the PFO laser, which is represented by an increase of the laser threshold and a decrease of the slope efficiency. Compared to the relatively small change in the laser threshold, the reduction in the slope efficiency by a factor of 3 gives a robust and sensitive approach for detecting explosive analytes. Using a flowing chamber design, the laser dynamics in the exposure and the recovery were measured to reveal the sensitivity of the PFO lasers. When exposed to the DNB molecules, the laser output was quenchedby 1/e of in 65 s, showing a relatively fast response. Three different approaches for removing the DNB molecules were explored to recover the PFO laser performance. It took 6 seconds

to recover to the 1/e of the original value in vacuum, 32 seconds under the nitrogen gas flow, and 34 minutes in air.

A theoretical model was developed to simulate the penetration of the DNB molecules into the PFO layer in order to get an insight to the interaction between these two materials. The simple square diffusion profile, similar to Case II diffusion, is capable of providing a good fit to the experimental results, by assuming a 85% quenching of the original emission and 71 nm penetration depth of the DNB molecules into the PFO layer in a five-minute exposure. This model is also supported by successfully predicting the fractional change in the PFO laser threshold. Overall, in this chapter, the PFO DFB laser was demonstrated to be suitable candidate for low pressure explosive vapour detection with fast response and large efficiency.

7.9. References

[1] N.C. Giebink and S.R. Forrest, *Physical Review B*, 2009. **79**(7).

[2] A.E. Vasdekis, G. Tsiminis, J.C. Ribierre, L. O'Faolain, T.F. Krauss, G.A. Turnbull, and I.D.W. Samuel, *Optics Express*, 2006. **14**(20): p. 9211.

[3] M. Haiml, R. Grange, and U. Keller, *Applied Physics B-Lasers and Optics*, 2004. **79**(3): p. 331.

[4] Y. Yang, G.A. Turnbull, and I.D.W. Samuela, *Applied Physics Letters*, 2008. **92**(16).

[5] Y. Yang, I.D.W. Samuel, and G.A. Turnbull, *Advanced Materials*, 2009. **21**(31): p. 3205.

[6] Y. Oki, S. Miyamoto, M. Maeda, and N.J. Vasa, *Optics Letters*, 2002. **27**(14): p. 1220.

[7] H. Ma, A.K.Y. Jen, and L.R. Dalton, *Advanced Materials*, 2002. **14**(19): p. 1339.

[8] S. Perissinotto, G. Lanzani, M. Zavelani-Rossi, M. Salerno, and G. Gigli, *Applied Physics Letters*, 2007. **91**(19).

[9] D. Amarasinghe, A. Ruseckas, A.E. Vasdekis, G.A. Turnbull, and I.D.W. Samuel, *Applied Physics Letters*, 2008. **92**(8).

[10] S.W. Thomas, G.D. Joly, and T.M. Swager, *Chemical Reviews*, 2007. **107**(4): p. 1339.

[11] A. Rose, Z.G. Zhu, C.F. Madigan, T.M. Swager, and V. Bulovic, *Nature*, 2005. **434**(7035): p. 876.

[12] S. Richardson, H.S. Barcena, G.A. Turnbull, P.L. Burn, and I.D.W. Samuel, *Applied Physics Letters*, 2009. **95**(6).

[13] G. Heliotis, R.D. Xia, G.A. Turnbull, P. Andrew, W.L. Barnes, I.D.W. Samuel, and D.D.C. Bradley, *Advanced Functional Materials*, 2004. **14**(1): p. 91.

[14] R.D. Xia, G. Heliotis, Y.B. Hou, and D.D.C. Bradley, *Organic Electronics*, 2003. **4**(2-3): p. 165.

[15] G. Heliotis, R. Xia, D.D.C. Bradley, G.A. Turnbull, I.D.W. Samuel, P. Andrew, and W.L. Barnes, *Applied Physics Letters*, 2003. **83**(11): p. 2118.

[16] Q. Zhou and T.M. Swager, *Journal of the American Chemical Society*, 1995. **117**(50): p. 12593.

[17] J.S. Yang and T.M. Swager, *Journal of the American Chemical Society*, 1998. **120**(46): p. 11864.

[18] L. Basabe-Desmonts, D.N. Reinhoudt, and M. Crego-Calama, *Chemical Society Reviews*, 2007. **36**(6): p. 993.

[19] J.S. Yang and T.M. Swager, *Journal of the American Chemical Society*, 1998. **120**(21): p. 5321.

[20] S.J. Toal and W.C. Trogler, *Journal of Materials Chemistry*, 2006. **16**(28): p. 2871.

[21] T.M. Swager and J.H. Wosnick, *Mrs Bulletin*, 2002. **27**(6): p. 446.

[22] S.W. Thomas, J.P. Amara, R.E. Bjork, and T.M. Swager, *Chemical*

Communications, 2005(36): p. 4572.

[23] M.A. Stevens, C. Silva, D.M. Russell, and R.H. Friend, *Physical Review B*, 2001. **63**(16).

[24] M. Ariu, M. Sims, M.D. Rahn, J. Hill, A.M. Fox, D.G. Lidzey, M. Oda, J. Cabanillas-Gonzalez, and D.D.C. Bradley, *Physical Review B*, 2003. **67**(19).

[25] G.F. Barlow, A. Shore, G.A. Turnbull, and I.D.W. Samuel, *Journal of the Optical Society of America B-Optical Physics*, 2004. **21**(12): p. 2142.

[26] M. Sanopoulou, D.F. Stamatialis, and J.H. Petropoulos, *Macromolecules*, 2002. **35**(3): p. 1012.

[27] H. Cavaye, A.R.G. Smith, M. James, A. Nelson, P.L. Burn, I.R. Gentle, S.C. Lo, and P. Meredith, *Langmuir*, 2009. **25**(21): p. 12800.

Chapter 8

Conclusion

Since the first demonstration in 1992 [1], organic semiconductor lasers have proven themselves as compact laser sources with simple fabrication, low cost, and broad tunability covering the whole visible spectrum. Over the past decade, driven by the ultimate aim of electrically pumped organic laser diodes, a lot of progress has been made in both new materials and resonator design to reduce the lasing threshold [2-7]. While electrically excited organic lasers remain an ongoing research goal, the downsizing of excitation lasers has removed smoothly from a regenerative amplifier[8] to InGaN diode lasers[9]. In complementary work, hybrid optoelectronic devices which exploit the benefits of both organic and inorganic semiconductors have become a growing interest of research. For instance, organic semiconductor thin films have been combined with blue nitride LEDs for highly efficient wavelength conversion in the context of full colour displays [10-11]. Elsewhere, silicon substrates were introduced into organic lasers to open the possibility of integrating organic lasers with other components for cost effective optical communication systems [12]. Driven by the lighting industry, the DC power from inorganic LEDs (especially the emergent blue GaN LEDs) has improved significantly, making them potentially attractive candidates for hybridizing with organic semiconductor lasers as the optical pump source.

The first experimental chapter of this thesis, **Chapter 4**, discussed the first demonstration of this hybrid structure: the LED pumped organic semiconductor laser [13]. The challenge lay in the relatively low output power and high divergence of LEDs. The most powerful commercial blue (450 nm) LEDs, chosen from LUMILEDS, were investigated. The incoherent output beams from these LEDs lead to a very low focusing efficiency with the use of conventional imaging technique. Hence, a relatively small light emitting chip (1.5 mm by 1.5 mm) was chosen to directly pump the organic laser, with the encapsulating layer around the chip removed. A further increase in power intensity was realized by pulsing the LED with a laser diode driver capable of providing up to 160 A current in a pulse as short as 15 ns. The strong current pulse raised the power intensity of the blue LED to 255 W/cm^2. A surface emitting DFB laser based on a yellow emitting copolymer, consisting of F8 and BT units, was developed to give a lasing threshold as low as 208 W/cm^2. When pumped by the pulsed blue GaN LED, both a sharp peak in the emission spectrum and a kink in the input vs output graph confirmed that the polymer laser was successfully pumped above the threshold. This is the first LED pumped organic laser, demonstrating itself as an alternative approach to the direct electrically excited organic laser. The future of LED pumped organic laser lies in the complete integration of the LED with organic lasers, which could contain a GaN LED controlled by CMOS circuits with the organic DFB laser directly fabricated on top via imprint technique (e.g.: nano-imprint lithography). Such lasers are the goal of the EPSRC funded HYPIX project and would be the future for compact, low cost and current controllable organic laser sources.

While LED pumped lasing was successfully demonstrated, the limited power density of the LED meant the laser could not be pumped far above threshold. A higher pump level from the LED is required to enhance the performance of the

polymer lasers. In **Chapter 5**, a non-imaging focusing technique, the luminescent concentrator, was used for the first time to increase the LED power density. The concentrator was a slab waveguide made of a dye doped (coumarin 6 or coumarin 334) SU8 matrix on a silica substrate. The concentrator changed the circular excitation spot with diameter of 1.5 mm (resembling that of the LED chip) to a narrow strip (31 μm by 1.5 mm), thus improving the power density. Several optimization steps, including the waveguide thickness, material PLQY, dye concentration and substrate size, were performed to maximize the light concentration ratio (LCR), defined as the ratio of the edge emission intensity to the excitation power intensity. Maximum LCRs of 9.5 and 9.8 were achieved for coumarin 334 and coumarin 6 doped SU8 concentrators, close to the predictions from a simple theoretical model. The insertion of the coumarin 334 doped SU8 luminescent concentrator between the excitation laser and a surface emitting MEH-PPV DFB laser (both 1D and 2D) reduced the threshold intensity by a factor of 4.5. The threshold reduction agreed well with the expected value. Owing to the high lasing threshold from the MEH-PPV gain medium, LEDs have not yet been tested as the excitation source. However, the large reduction in threshold intensity shows the capability of the luminescent concentrator as a useful element for improving LED pumped organic lasers, if a better lower threshold gain medium, such as Red F [14], were to be used.

One of the advantages of organic semiconductors is their broad emission spectra, which is very useful in spectroscopic applications. The broad emission spectra also promise short pulse operation, if the cavity longitudinal modes can be locked in phase. Passive and active mode-locked lasers were successfully demonstrated in organic dye lasers thirty years ago. As materials with similar broad emission spectra and superior performance as gain media in the solid state, organic semiconductors are potentially good candidates for mode-locked lasers. The first step towards

developing a passively mode-locked polymer laser was described in **Chapter 6**. A solid state saturable absorber made of dye doped polystyrene was characterized. The HIDCI saturable absorber exhibited absorption saturation at an excitation intensity of a few MW/cm^2, with an absorption change of around 20%. A hybrid organic/inorganic SESAM was then demonstrated with the saturable absorber layer coated on a commercial inorganic DBR mirror. This showed a change in the reflectivity of between 10% and 25% at the saturation intensity. As a first test of the saturable absorber, a polymer laser based on a conventional Fabry-Perot resonator with MEH-PPV solution as gain medium was built. The inclusion of the saturable absorber in the cavity resulted in the formation of a pulse train with pulse widths of several hundreds of picoseconds. This was different from the dynamics without the saturable absorber, but was attributed to Q-switching rather than mode-locking. A theoretical model suggested the size of the internal optical field on the saturable absorber was responsible for the number of pulses and their separation in the pulse train. Although mode-locking hasn't yet been observed by the end of this thesis, this first attempt points out the future direction towards a mode-locked polymer laser: a longer pump pulse, a saturable absorber with shorter recovery time and a gain medium with long PL lifetime will be helpful in achieving this goal.

The final experimental chapter (**Chapter 7**) focused on the application of these organic semiconductor lasers in chemosensing. A blue surface emitting DFB laser based on a prototypical polymer, polyfluorene, was used to detect a nitro-aromatic explosive compound 1,4-Dinitrobenzene (DNB) at a low vapour pressure of 10 ppb. The polymer laser showed an increase in threshold and decrease in the output slope efficiency after exposure to the vapour, indicating that the DNB molecules act as fluorescence quenchers. In comparison to fluorescence from PFO thin films, PFO lasers were found to give a higher sensing efficiency, and so are more effective chemosensors. The experimental setup allowed in-situ monitoring, for the first time,

of the dynamics of the laser emission during exposure and recovery cycles. The output emission was observed to drop to 1/e of its initial value in 80 seconds, a fast response to the vapour molecules. The quenching process was reversible, shown by the recovery of the laser emission in three different recovery approaches: under vacuum, in flowing nitrogen and in air. The recovery time varied from 6 seconds (in vacuum), to 35 seconds (in flowing nitrogen) and 34 minutes (in air). The diffusion of the DNB molecules into the PFO layer was investigated through a simple theoretical model by assuming a square diffusion profile. A penetration depth of 71 nm and a quenching efficiency of 85% were deduced from the simple model. The model also successfully predicted the change in the laser threshold through a calculation of the confinement factor. The high sensing efficiency (80%) and fast response of PFO lasers to the low pressure DNB vapour make them attractive chemo detectors. In this chapter, polyfluorene is used as laser gain medium, because it is commercial available. The sensing efficiency could be further enhanced by better material design [15-17]. Additionally, with the rapid development both in the inorganic and organic materials, if LED excitation could be combined, organic semiconductor lasers would become the chemosensors with high efficiency, compact size and very low cost.

Overall, the rapid developments in organic semiconductor lasers, both on materials and resonators, have significantly reduced the complexity of the system, gradually bringing organic semiconductor lasers from laboratories to the real world. With the appealing properties of simple fabrication and broad tunability, organic semiconductor lasers are promising, cost effective, and compact solid-state lasers with great potentials in a wide range of practical applications such as chemosensing, bio-sensing, fluorescent spectroscopy and so on.

Reference

[1] D. Moses, *Applied Physics Letters*, 1992. **60**(26): p. 3215-3216.

[2] G. Heliotis, R.D. Xia, G.A. Turnbull, P. Andrew, W.L. Barnes, I.D.W. Samuel, and D.D.C. Bradley, *Advanced Functional Materials*, 2004. **14**(1): p. 91-97.

[3] T. Rabe, M. Hoping, D. Schneider, E. Becker, H.H. Johannes, W. Kowalsky, T. Weimann, J. Wang, P. Hinze, B.S. Nehls, U. Scherf, T. Farrell, and T. Riedl, *Advanced Functional Materials*, 2005. **15**(7): p. 1188-1192.

[4] C. Karnutsch, C. Gyrtner, V. Haug, U. Lemmer, T. Farrell, B.S. Nehls, U. Scherf, J. Wang, T. Weimann, G. Heliotis, C. Pflumm, J.C. deMello, and D.D.C. Bradley, *Applied Physics Letters*, 2006. **89**(20): p. 201108.

[5] B.K. Yap, R.D. Xia, M. Campoy-Quiles, P.N. Stavrinou, and D.D.C. Bradley, *Nature Materials*, 2008. **7**(5): p. 376-380.

[6] A.E. Vasdekis, G.A. Turnbull, I.D.W. Samuel, P. Andrew, and W.L. Barnes, *Applied Physics Letters*, 2005. **86**(16): p. 161102.

[7] C. Karnutsch, C. Pflumm, G. Heliotis, J.C. Demello, D.D.C. Bradley, J. Wang, T. Weimann, V. Haug, C. Gartner, and U. Lemmer, *Applied Physics Letters*, 2007. **90**(13): p. 131104.

[8] N. Tessler, G.J. Denton, and R.H. Friend, *Nature*, 1996. **382**(6593): p. 695-697.

[9] A.E. Vasdekis, G. Tsiminis, J.C. Ribierre, L. O'Faolain, T.F. Krauss, G.A. Turnbull, and I.D.W. Samuel, *Optics Express*, 2006. **14**(20): p. 9211-9216.

[10] G. Heliotis, E. Gu, C. Griffin, C.W. Jeon, P.N. Stavrinou, M. D Dawson, and D.D.C. Bradley, *Journal of Optics a-Pure and Applied Optics*, 2006. **8**(7): p. S445-S449.

[11] G. Heliotis, G. Itskos, R. Murray, M.D. Dawson, I.M. Watson, and D.D.C. Bradley, *Advanced Materials*, 2006. **18**(3): p. 334.

[12] A.E. Vasdekis, S.A. Moore, A. Ruseckas, T.F. Krauss, I.D.W. Samuel, and G.A. Turnbull, *Applied Physics Letters*, 2007. **91**(5): p. 051124.

[13] Y. Yang, G.A. Turnbull, and I.D.W. Samuel, *Applied Physics Letters*, 2008. **92**(16):

p. 163306-3.

[14] G. Heliotis, R. Xia, D.D.C. Bradley, G.A. Turnbull, I.D.W. Samuel, P. Andrew, and W.L. Barnes, *Journal of Applied Physics*, 2004. **96**(12): p. 6959-6965.

[15] S. Richardson, H.S. Barcena, G.A. Turnbull, P.L. Burn, and I.D.W. Samuel, *Applied Physics Letters*, 2009. **95**(6): p. 063305.

[16] J.S. Yang and T.M. Swager, *Journal of the American Chemical Society*, 1998. **120**(46): p. 11864-11873.

[17] S.W. Thomas, G.D. Joly, and T.M. Swager, *Chemical Reviews*, 2007. **107**(4): p. 1339-1386.